LPNHE
PARIS

THESE DE DOCTORAT
DE L'UNIVERSITÉ PIERRE ET MARIE CURIE

présentée par

Camille Couturier

Pour obtenir le grade de

DOCTEUR DE L'UNIVERSITÉ PIERRE ET MARIE CURIE

Spécialité :

Physique de la Particule à la Matière Condensée (ED 389)

Invariance de Lorentz et Gravité Quantique: contraintes avec des sources extragalactiques variables observées par H.E.S.S. et *Fermi*-LAT

Soutenue le 21 octobre 2014

Après avis de :

MM	Alain	BLANCHARD	Rapporteur
	Paschal	COYLE	Rapporteur

Devant le jury composé de :

MM	Giovanni	AMELINO-CAMELIA	Examinateur
	Paschal	COYLE	Rapporteur
	Frédéric	DAIGNE	Examinateur
Mme	Agnieszka	JACHOLKOWSKA	Directrice de thèse
M.	David	SMITH	Examinateur

cnrs IN2P3 Les deux infinis

UPMC SORBONNE UNIVERSITÉS

université PARIS DIDEROT PARIS 7

LPNHE
PARIS

PhD THESIS
OF THE UNIVERSITÉ PIERRE ET MARIE CURIE

presented by

Camille Couturier

Submitted in fulfillment of the requirements for the degree of

DOCTEUR DE L'UNIVERSITÉ PIERRE ET MARIE CURIE

Speciality :

Physics from Particles to Condensed Matter (ED 389)

Lorentz Invariance Violation and Quantum Gravity: constraints from astrophysical observations of extragalactic transient events.

Defended on October 21st 2014

Following the reports from:

Mr	Alain	BLANCHARD	Referee
	Paschal	COYLE	Referee

In front of the committee:

Mr	Giovanni	AMELINO-CAMELIA	Examiner
	Paschal	COYLE	Referee
	Frédéric	DAIGNE	Examiner
Mrs	Agnieszka	JACHOLKOWSKA	Supervisor
Mr	David	SMITH	Examiner

cnrs IN2P3 Les deux infinis

UPMC SORBONNE UNIVERSITÉS

université PARIS DIDEROT PARIS 7

Contents

List of figures

List of tables

Introduction

Some Quantum Gravity (QG) theories allow for a violation of Lorentz invariance (LIV), manifesting as a dependence on the velocity of light in vacuum on its energy. If such a dependence exists, then photons of different energies emitted together by a distant source will arrive at the Earth at different times. High energy (above 1 GeV) or very high energy (above 100 GeV) transient emissions from distant astrophysical sources such as Gamma-ray Bursts (GRBs) and Active Galaxy Nuclei (AGNs) can be used to search for and constrain LIV. A short review of such tests is given in chapter 1; the two types of sources used, blazars and GRBs, are described in chapter 2.

The data of two leading Gamma-ray telescopes have been used: H.E.S.S., described in chapter 3 – for which a study of the quality of the calibrated data has been performed and is presented in chapter 4 – and *Fermi*-LAT, presented succinctly in chapter 5. This work presents the studies obtained with these two telescopes in terms of constraints on the dispersion parameter in vacuum, and on the energy scale at which QG effects causing LIV may arise. The method used is described in detail in chapter 6, along with a study of the impact of the variation of the main parameters in the method; a modification of the method in the case of non-negligible background is also provided. Chapter 7 describes the study of an AGN flare with such a relatively low signal-to-noise ratio using H.E.S.S. data. Chapter 8 presents the results of the analysis of 4 bright GRBs observed by the *Fermi*-LAT.

Chapter 1

Testing Lorentz Invariance violation and Quantum Gravity with photons from astrophysical sources

Contents

The Lorentz Invariance is a building brick of the Special theory of Relativity. However it may not hold at extremely high energies. Testing a possible Lorentz violation (LIV) is not only motivated by its validity at extreme energies: LIV was also suggested in various Quantum Gravity (QG) models, as a tool to detect QG effects at Planck scale.

This brief review is inspired by the reviews of Amelino-Camelia [1], Liberati *et al.* [2] and Mattingly [3] and focuses on the experimental tests possible at very high energies.

1.1 Special relativity and Lorentz invariance

This part benefits from the reading of [2], [4] and [5].

Lorentz invariance means invariance under Lorentz transformations (rotations and boosts) in a local tangent space at a given space-time point.

More generally, Special Relativity (SR) relies on the transformations of the Poincarré group, which leaves the local space-time metric invariant. The Poincarré group includes the following symmetries: Lorentz-Poincarré transformations (3 boosts), space-time translations (4 operators), space rotations (3 operators), and 3 operations which correspond to discrete symmetries – the parity P, the time-reversal T and the charge conjugation C.

In SR, the existence of a maximum attainable speed appears as a consequence of the following principles:

— homogeneity of space,

— homogeneity of time,

— isotropy of space,

and

— relativity principle,

— causality principle.

This maximum attainable speed is not *a priori* the speed of light. It can be associated to the speed of light c with other arguments, from field theory.

As it is built on very general and desired properties of space-time, Lorentz invariance constitutes a strong constraint to build a physical theory.

1.2 Lorentz violating theories

1.2.1 Extensions of the Special relativity

It is possible that Lorentz symmetry breaks in a certain energy range, just as other symmetries break at low energies (*cf. e.g.* Higgs mechanism).

The violation of Lorentz invariance is often associated with a variation of the speed of light in vacuum. Thus, a manifestation of a break of the Lorentz invariance could be a change of the maximum attainable speed. In particular, the maximum attainable speed is not a constant anymore, and could vary with time or with the photon energy.

For instance, the dispersion relation for a photon, $E^2 = p^2c^2$ with E the energy of the photon and p its momentum, might be an approximation at low energies of a more general expression. Among others, the extended special relativity [6] and the doubly special relativity [7] propose to add a second term to this expression, introducing a particular length l_0 as a second invariant quantity:

$$E^2 = p^2c^2 - f(E, p; l_0)$$

The term depends on the model/theory considered: for instance, for the doubly special relativity, $f(E, p; l_0) = l_0 c p^2 E/\hbar$ with $\hbar$ the reduced Planck constant.

What we call the "speed" of a particle corresponds to its *group* velocity [1], defined as $v_g = \partial E/\partial p$.

1. While the *phase* velocity $v_\phi = E/p$ can have a value greater than c, the group velocity v_g is to be lower than c, in the framework of Special relativity.

1.2.2 Quantum Gravity theories

The search for a quantum theory of gravitation emerges from the apparent contradiction between the Standard Model and the General theory of Relativity, in some specific situations: *e.g.* description of the Big Bang and consistent description of the black holes.

Several theoretical models, grouped within the term of Quantum Gravity (QG) models, try to describe and predict the unknown nature of space-time at Planck length:

$$l_{\text{Planck}} = \sqrt{\frac{\hbar G}{c^3}} \simeq 1.6 \times 10^{-35}\,\text{m}$$

where G is the gravitational constant. They include:

— Loop quantum gravity,

— Non-commutative geometry,

— String-inspired models (D branes),

— Wrapped brane worlds,

— Emergent gravity.

It is believed that QG effects appear only at this length, or equivalently, at energy scales near the Planck energy

$$\text{E}_{\text{Planck}} = \frac{\hbar}{c \times l_{\text{Planck}}} = \sqrt{\frac{\hbar c^5}{G}} \simeq 1.22 \times 10^{19}\,\text{GeV}.$$

In particular, extrapolating from the sub-TeV experimental data, one can expect the unification of the non-gravitational coupling constants (electroweak and strong forces) to be roughly at E_{Planck} (within a few orders of magnitude). The fact *a priori* uncorrelated scales seem to meet there encourages to look for a wider unification scheme, which could include gravity.

The search for probes of QG theories is called "Quantum Gravity phenomenology". Such tests include:

— the search for QG imprint on initial cosmological perturbations, violation of discrete symmetries;

— the search for violation of space-time symmetries including Lorentz Invariance violation.

1.3 Manifestation of Lorentz Invariance violation

A breaking of the Lorentz Invariance can manifest as:

— a maximum attainable velocity of a particle $\neq$ c;

— a modification of energy thresholds of reactions (for instance $\gamma\gamma$ EBL interactions), which could lead to *e.g.* a hardening of the spectrum in very high energy (VHE) sources;

— the allowance of particle interactions/decays kinetically forbidden by Lorentz Invariance;

— or the suppression of known particle interactions or decays;

— modified dispersion relations: Vacuum birefringence (introducing the sign of the helicity of the photon) and Vacuum dispersion (*e.g.* the modified dispersion in 1.2.1).

We will focus on the latter manifestation and look for an energy-dependence of the speed of light in vacuum.

1.3.1 Frameworks - Effective Field Theories

The Lorentz violating theories (1.2) can be grouped under a general framework of effective theory. The quantum gravity effects are likely to be suppressed by a power of $\frac{1}{\mathrm{E_{QG}}}$, *e.g.* by a factor $\frac{10^3}{10^{19}} = 10^{-16}$ for a particle with energy 1 TeV and assuming $\mathrm{E_{QG}} \sim \mathrm{E_{Planck}} \sim 10^{19}$ GeV. The following phenomenological parameterizations can be viewed as low-energy effective field theories, holding at energies $E << \mathrm{E_{Planck}}$ and providing an effective framework to search for LIV at reachable energies.

Standard Model Extension

The (minimal) Standard Model Extension, (m)SME, developed by Kostelecky *et al.* [8, 9, 10] is an extension of the Standard model which includes Lorentz violation operators. It also includes both CPT -preserving and -violating terms. It was built after it was shown that certain string theories could spontaneously break CPT invariance [2].

We define the degree of dispersion due to LIV effects τ_n for two photons as the ratio of their delay in arrival Δt over the difference of their energies (resp. of their squared energies) $\Delta(E^n)$. In the SME framework, the LIV effects are described by a series expansion with respect to powers of the photon energy. The leading term reads as:

$$\tau_n \simeq \frac{1}{H_0} \left(\sum_{jm} {}_0Y_{jm}(\hat{\boldsymbol{n}}) c^{(n+4)}_{(I)jm} \right) \times \kappa_n, \tag{1.1}$$

where $\hat{\boldsymbol{n}}$ is the direction of the source, ${}_0Y_{jm}(\hat{\boldsymbol{n}})$ are spin-weighted spherical harmonics, $c^{(n+4)}_{(I)jm}$ are coefficients describing the strength of LIV, and the distance κ_n is defined in next paragraph.

Series expansion framework

Amelino-Camelia, Ellis *et al.* [12] parametrized the possible LIV time delays also using a series expansion of powers of the photon energy over $\mathrm{E_{QG}}$. For close (*e.g.* galactic) objects, the degree of dispersion can be written as simply as:

$$\tau_n = \frac{\Delta t}{\Delta(E^n)} \simeq s_{\pm} \frac{L}{\mathrm{E^n_{QG}} c} \tag{1.2}$$

where L is the distance of the source. $n = 1$ (resp. $n = 2$) accounts for linear (quadratic) LIV effects. The value of the coefficient $s_{\pm}$ is $s_{\pm} = -1$ (resp. $+1$) in superluminal (subluminal) case, *i.e.* if the photons are faster with larger (smaller) energies.

For distant (*e.g.* extragalactic) sources, this expression has to be modified to account for the universe's cosmological expansion. Specifically, the degree of dispersion is then connected to $\mathrm{E_{QG}}$, to the modified distance of the source κ_n, and to the Hubble constant $\mathrm{H_0}$:

$$\tau_n = \frac{\Delta t}{\Delta(E^n)} \simeq s_{\pm} \frac{(1+n)}{2\mathrm{E^n_{QG}} \mathrm{H_0}} \kappa_n \tag{1.3}$$

2. **CPT and Lorentz violations**: It has been shown that CPT violation entails Lorentz violation. The opposite is not true: the violation of Lorentz Invariance does not require the violation of CPT invariance [11].

with the correct expression [13] of the distance κ_n:

$$\kappa_n = \int_0^z \frac{(1+z')^n \, dz'}{\sqrt{\Omega_m (1+z')^3 + \Omega_\Lambda}} \tag{1.4}$$

A direct consequence of equation 1.3 is that any measurement (or limit) on the dispersion parameter τ_n with photons detected in a well-located (*i.e.* with known redshift) gamma-ray source can lead to a measurement (or limit) on the energy scale $\mathrm{E_{QG}}$. The sensitivity of such a measure with a given source depends on the distance of the source, its variability and the energy range of the emitted photons: for these three parameters, the higher, the most noticeable the effects.

This framework is much simpler than the SME framework, and provides a direct and model-independent test of Lorentz Invariance. We chose this one to obtain the main results of this work, where the dependence of the arrival time of the photons from the distant sources on energy is investigated.

1.3.2 Order of magnitude – previous results

Expected limits for example sources

In case the measured degree of dispersion τ_n is compatible with $0\,\mathrm{s/GeV}^n$, then using equation 1.3, we can get lower limits on $\mathrm{E_{QG,n}}$:

$$\mathrm{E_{QG,n}} \gtrsim \left(\frac{(1+n) k_n(z) \cdot \tau_n}{2\mathrm{H_0}} \right)^{\frac{1}{n}} = \left(\frac{(1+n) k_n(z) \cdot \Delta(E^n)}{2\mathrm{H_0} \cdot \Delta t} \right)^{\frac{1}{n}} \tag{1.5}$$

Table 1.1 gives expected limits on the Quantum Gravity energy scale (for linear and quadratic cases) for various configurations:

— redshifts z of 10^{-6} (corresponding to $\sim 4\,\mathrm{kpc}$ [3]), 10^{-3} ($\sim 4\,\mathrm{Mpc}$), 10^{-1} ($\sim 0.4\,\mathrm{Gpc}$), 1 and 10;

— maximum energies of 1 keV, 1GeV, 1 TeV;

— variability of 1 ms, 1 s, 10^3 s.

The following characteristics are preferred to put tight constraints on $\mathrm{E_{QG}}$:

— cosmological distances ($z \gtrsim 1$);

— very high energies ($\Delta E \sim E_{\mathrm{max}}$ of the order of TeV);

— fast variability ($\Delta t <$ s).

As examples, these events would set nicely constraining bounds on $\mathrm{E_{QG}}$:

— A flare of a blazar seen by a ground telescope such as H.E.S.S. ($\mathrm{E_{max}} \sim 1\,\mathrm{TeV}$) at a redshift of 0.1 to 0.5 with a variability of a few minutes is expected to give lower limits on $\mathrm{E_{QG,1}}$ of the order of 10^{17} - $10^{19}\,\mathrm{GeV}$ (linear case) and 10^{10} - $10^{11}\,\mathrm{GeV}$ (quadratic case).

— A Gamma-ray burst (GRB) detected by a space telescope such as *Fermi*-LAT ($\mathrm{E_{max}} \sim 1\,\mathrm{GeV}$) at a redshift of 1 to 10 with a measured delay Δt of a few ms could possibly give a lower bound on $\mathrm{E_{QG,1}}$ up to $\sim 10^{20}\,\mathrm{GeV}$ (linear case) and $10^{10}\,\mathrm{GeV}$ (quadratic case).

3. using the Hubble law

— A millisecond pulsar, located at a few kpc from Earth, emitting at energies up to GeV, showing a phase alignment of two separate energy bands within 1 μs, would lead to lower limits on $E_{QG,1}$ of the order of 10^{17} GeV.

	Limits on τ_1 in s/GeV (linear case)				
	10^6	10^3	1	10^{-3}	10^{-6}
e.g. (Δt, E_{max}) =	(10^3 s, 1 keV)	(1 s, 1 keV) (10^3 s, 1 GeV)	(1 ms, 1 keV) (1 s, 1 GeV) (10^3 s, 1 TeV)	(1 μs, 1 keV) (1 ms, 1 GeV) (1 s, 1 TeV)	(1 μs, 1 GeV) (1 ms, 1 TeV)
	Lower limits on $E_{QG,1}$ in GeV (linear case)				
$z = 10^{-6}$	4×10^{5}	4×10^{8}	4×10^{11}	4×10^{14}	4×10^{17}
$z = 10^{-3}$	4×10^{8}	4×10^{11}	4×10^{14}	4×10^{17}	4×10^{20}
$z = 0.1$	4×10^{10}	4×10^{13}	4×10^{16}	4×10^{19}	4×10^{22}
$z = 1$	5×10^{11}	5×10^{14}	5×10^{17}	5×10^{20}	5×10^{23}
$z = 10$	4×10^{12}	4×10^{15}	4×10^{18}	4×10^{21}	4×10^{24}

(a) Limits for a linear dispersion of light (n = 1)

	Limits on τ_2 in s/GeV^2 (quadratic case)						
	10^9	10^6	10^3	1	10^{-3}	10^{-6}	10^{-9}
e.g. (Δt, E_{max}) =	(10^3 s, 1 keV)	(1 s, 1 keV)	(1 ms, 1 keV) (10^3 s, 1 GeV)	(1 μs, 1 keV) (1 s, 1 GeV)	(1 ms, 1 GeV) (10^3 s, 1 TeV)	(1 μs, 1 GeV) (1 m, 1 TeV)	(1 ms, 1 TeV)
	Lower limits on $E_{QG,2}$ in GeV (quadratic case)						
$z = 10^{-6}$	2×10^{1}	7×10^{2}	2×10^{4}	7×10^{5}	2×10^{7}	7×10^{8}	2×10^{10}
$z = 10^{-3}$	7×10^{2}	2×10^{4}	7×10^{5}	2×10^{7}	7×10^{8}	2×10^{10}	7×10^{11}
$z = 0.1$	7×10^{3}	2×10^{5}	7×10^{6}	2×10^{8}	7×10^{9}	2×10^{11}	7×10^{12}
$z = 1$	3×10^{4}	1×10^{6}	3×10^{7}	1×10^{9}	3×10^{10}	1×10^{12}	3×10^{13}
$z = 10$	2×10^{5}	5×10^{6}	2×10^{8}	5×10^{9}	2×10^{11}	5×10^{12}	2×10^{14}

(b) Limits for a quadratic dispersion of light (n = 2)

Table 1.1: Expected lower limits on the Quantum Gravity energy scale $E_{QG,n}$ (in GeV) for various configurations.

Comparison of previous results

Table 1.2 gives the limits on the Quantum Gravity energy scale E_{QG} (Series expansion framework) from measurements of the linear (n = 1) and the quadratic (n = 2) dispersion parameters in the data of transient events (GRBs, AGN flares) or pulsars seen by gamma telescopes. Limits given are as of 2011, before the beginning of this work. Best limits had been obtained with PKS 2155-304 by the H.E.S.S. Collaboration with a likelihood method analysis, and with GRB 090510 by the *Fermi* Collaboration using a maximum sharpness method ("DisCan").

In the following, we will provide new results obtained with two types of particular sources: PG 1553+113 and four "golden" GRBs detected and analyzed within the H.E.S.S. and *Fermi* collaborations respectively.

Source(s)	**Experiment**	**Method**	**Results (95% CL limits)**
Mrk 421	Whipple	likelihood	$E_{QG,1} > 4\times10^{16}$ GeV
Mrk 501	MAGIC	ECF	$E_{QG,1} > 2\times10^{17}$ GeV $E_{QG,2} > 3\times10^{10}$ GeV
		likelihood	$E_{QG,1} > 3\times10^{17}$ GeV $E_{QG,2} > 5.7\times10^{10}$ GeV
PKS 2155-304	H.E.S.S.	MCCF	$E_{QG,1} > 7.2\times10^{17}$ GeV $E_{QG,2} > 1.4\times10^{9}$ GeV
		wavelets	$E_{QG,1} > 5.2\times10^{17}$ GeV
		likelihood	$E_{QG,1} > 2.1\times10^{18}$ GeV $E_{QG,2} > 6.4\times10^{10}$ GeV
GRB 021206	*RHESSI*	fit + mean arrival time in a spike	$E_{QG,1} > 1.8\times10^{17}$ GeV
GRB 080916C	*Fermi* GBM + LAT	associating a 13 GeV photon with the trigger time	$E_{QG,1} > 1.3\times10^{18}$ GeV $E_{QG,2} > 9\times10^{9}$ GeV
GRB 090510	*Fermi* GBM + LAT	associating a 31 GeV photon with the start of any observed emission, DisCan	$E_{QG,1} > 1.5\times10^{19}$ GeV $E_{QG,2} > 3.0\times10^{10}$ GeV
9 GRBs	BATSE + OSSE	wavelets	$E_{QG,1} > 7\times10^{15}$ GeV $E_{QG,2} > 2.9\times10^{6}$ GeV
15 GRBs	*HETE-2*	wavelets	$E_{QG,1} > 4\times10^{15}$ GeV
17 GRBs	*INTEGRAL*	likelihood	$E_{QG,1} > 3.2\times10^{11}$ GeV
35 GRBs	BATSE + *HETE-2* + *Swift*	wavelets	$E_{QG,1} > 1.4\times10^{16}$ GeV
Crab Pulsar	VERITAS	fit + comparison of the positions of the peaks at low and high energies	$E_{QG,1} > 3\times10^{17}$ GeV $E_{QG,2} > 7\times10^{9}$ GeV

Table 1.2: Bounds on the Quantum energy scale E_{QG} from measurements of the linear (n = 1) and the quadratic (n = 2) dispersion parameters in the data of transient events (GRBs, AGN flares) or pulsars seen by gamma telescopes. Limits as of 2011, before the beginning of this work. The limits are at a 95% confidence level. Adapted from [14].

Chapter 2

Extragalactic gamma-ray sources

Contents

Blazars and Gamma-ray bursts are among the most violent astrophysical objects observed. Their main features – SED, variability – are described here.

2.1 Blazars

2.1.1 Active Galactic Nuclei and Blazars

Quasi-stellar radio objects ("quasars") are known to be of extragalactic origins for more than 50 years: it was first realized in 1963 from the spectrometry of 3C 273 that this specific source has a redshift of 0.16 [15]. This, combined with an optical magnitude of 13, meant that the luminosity of this source was enormous, pointing toward powerful emission mechanisms. This object was later described as an *Active galactic nucleus* (AGN), a kind of quasar.

Different subclasses of these objects have since been observed and studied in detail. They can be split between radio-loud and radio-quiet objects, the latter not exhibiting jets. Among the radio-loud AGNs, the most variable are the *Flat spectrum radio quasars* (FSRQs) and the BL Lac [1] objects. They are refered to as "blazars". Both also exhibit a significant polarization ($\sim 10\%$). A difference between these two objects is a wider and stronger emission line present in the FSRQs. Besides, BL Lac objects are variable to a lesser degree than FSRQs.

1. called after BL Lacertae

2.1.2 Variability

Characteristic time scales of a blazar range from a few minutes to years. The period of high variability (intra-night) are called "Flares": a famous example of such period is the 2006 flares of PKS 2155-304 [16]. Causality principle along with short variability time scales lead to very small characteristic sizes of the emission regions, in some cases smaller than the Solar system. The very high luminosity, combined with small emission region, lead toward a black hole-powered mechanism.

2.1.3 Unification scheme

The unification scheme of AGN [17, 18] proposes a coherent explanation of the different classes of AGNs: these differences would arise from distinct angles of observation of the same kind of object. Figure 2.1 depicts a typical AGN in this scheme: the engine of the emission is a massive black hole, with an accretion disk. In these objects, the gravitational potential energy is released through the accretion process. In some AGNs, part of this energy is indirectly released through two opposite collimated jets of ejected matter.

In particular, within this scheme, blazars are thought to be a subclass of AGN where a jet is observed in the line of sight. The apparent superluminal motion that they exhibit [19, 20, 21] can be explained by a relativistic motion seen in a favorable viewing angle [22].

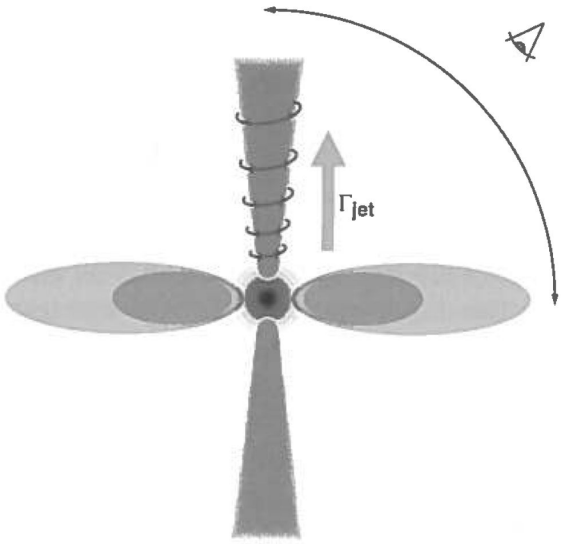

Figure 2.1: Cartoon of the structure of AGN, from [23]. A blazar is thought to be observed in the line of sight of one of the two jets.

2.1.4 Production of gamma-ray photons in Blazars

Leptonic models

Two peaks are observed in spectral energy distribution (SED) of an AGN. The majority of AGN emission models explain them with leptonic processes, and do not involve hadronic interactions. In these models, the low energy component of the spectrum is attributed to the synchrotron emission of relativistic leptons. The second bump in the SED is explained by inverse Compton scattering (relativistic lepton transferring energy to soft photons):

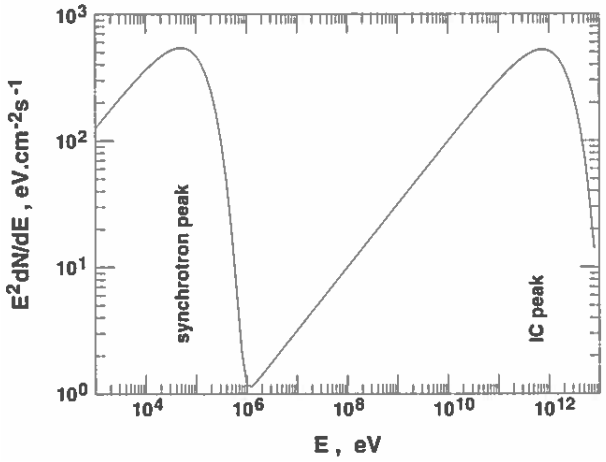

Figure 2.2: Spectrum generated by the SSC model: the two peaks correspond to synchrotron (lower energies) and inverse Compton (higher energies) emission. From [23].

— in the synchrotron self-Compton model (SSC), the same population of particles is responsible for the Synchrotron emission (first bump) and the inverse Compton emission (second bump). The electrons are accelerated in the jet frame. In this model, the two peaks are strongly correlated. A spectrum generated with the SSC model is shown in Figure 2.2.

— in the external radiation Compton (ERC), the population of soft photons is outer to the source: they can be emitted by the accretion disk, and interact with the central regions of the AGN, close to the jet emitter.

Hadronic models

Some models involving hadronic interaction, more complicated than leptonic-only models, have been proposed. They lack of observations probing hadronic-specific interactions. As they are necessary product of hadronic interactions, neutrinos appear as great messengers for probing the mechanisms in such objects. Besides, as their cross section is far lower than photon's with the encountered media, they can escape the inner emission region and travel without being absorbed. Among others, the ANTARES [24] and IceCube [25] Collaborations are working toward detecting such cosmological neutrinos. The neutrino astronomy is expected to revolutionize our current understanding of these sources.

Time-dependant models

Most models try to explain the emission mechanism from the SED. However, during a flare, an evolution of the SED can be observed. A few try to take into account this spectral evolution, *e.g.* using a model derived from two-flow [26].

2.1.5 Distances

At very high energies (VHE), the gamma photons interact with the Extragalactic Background Light, in the infrared spectrum: thus, the spectra of these sources is distorted. More decisive, most distant AGNs cannot be observed at TeV energies. Thus, Cherenkov telescopes

observations are limited to AGN located up to a redhift of $z \sim 0.6$. The first blazar detected at TeV energies is Mrk 421 by Whipple in 1992 [27].

In the following chapters, the term "AGN" will mostly refer to the subclass of blazars.

2.2 Gamma-ray bursts (GRB)

Gamma-ray bursts are transient events observed in the gamma range, from keV to tens of GeV. They are followed by a declining emission ("afterglow") [2], lasting longer and emitting in a broader and lower energy range, from radio to X-rays.

The Burst and Transient Source Explorer (BATSE) instrument onboard the Compton Gamma Ray Observatory, launched in 1991, showed that the population of GRBs was isotropic, hinting toward a non-galactic origin. The measurement of the redshift of GRB 970508 from its afterglow in 1997 by Metzger *et al.* [28] made clear its extragalactic origin: they placed a lower limit on its redshift at $z > 0.835$. Reichart [29] determined its redshift to be $z = 1.09$. The GRB with the highest measured redshift detected so far is GRB 090423 [30], with $z = 8.2$. These enormous distances ($\sim$ 6Gly), the following analyses of supernovae and host galaxies, and their high luminosity altogether led toward an "exploding massive star" scenario for the long GRBs.

2.2.1 Variability and duration

The bursts' time profiles are rather complex. Norris *et al.* [31] proposed to unify the description of the GRB lightcurves observed by BATSE, parameterizing them as the continuous junction of two asymmetric exponential functions. these function, known as "Norris" or FRED [3] functions allow to describe the very different rise/decay profiles and sharpness encountered. They do not, however, reflect the physics of the emission.

A distinction is made depending the duration of the bursts [4]:

— GRBs with a duration of about a second or less are dubbed as "short" GRBs,

— GRBs with a duration of the order of minutes and more are designated as "long" GRBs.

2.2.2 Spectral energy distributions

Studying BATSE [33] observations of GRBs, Band *et al.* [34] showed that their spectral energy distributions (SED) could be empirically described by two smoothly connected power-law functions, with the junction located around 100 keV to 1 MeV (now called a "Band" function). Zhang *et al.* [32] showed that the emission of the GRB observed by *Fermi* GBM and LAT up to May 2010 could show up to two more components, as sketched in Figure 2.3: a non-thermal component (I – Band function) covering the whole GBM/LAT range, and peaking around 200 keV, an *a priori* thermal component at lower energies (II – quasi-blackbody) and an additional non-thermal component (III) becoming important at higher energies, possibly with a break around 1 TeV (thus not accessible by *Fermi*).

2. The afterglow duration can still be considered as rapid, as its flux decays as a power-law function of time.
3. FRED = Fast Rise Exponential Decay
4. The duration of the burst is usually measured as T90, *i.e.* the time interval where 90 % of the energy of the burst is released.

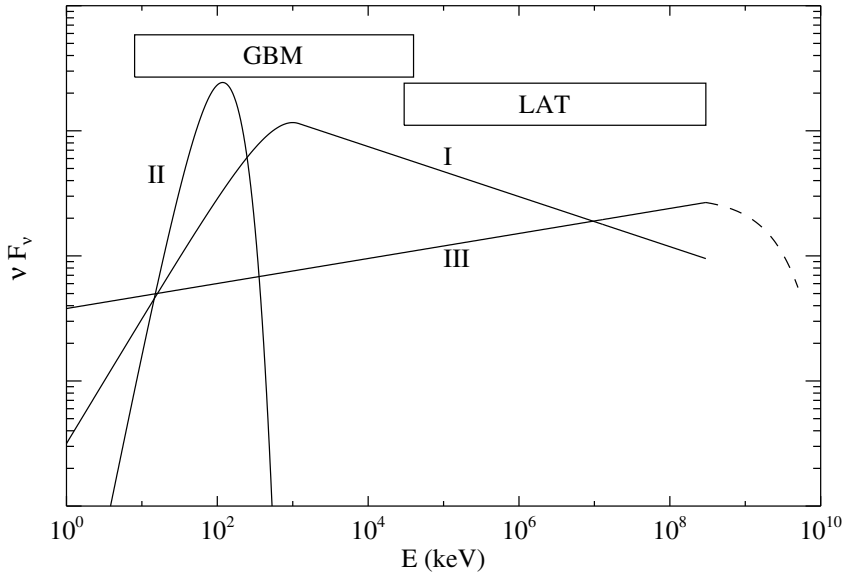

Figure 2.3: Description of the spectral energy distribution of GRBs observed by *Fermi* GBM and LAT up to May 2010, proposed by Zhang *et al.* [32]: a non-thermal component (I – Band function) covering the whole GBM/LAT range, and peaking around 200 keV, an *a priori* thermal component at lower energies (II – quasi-blackbody) and an additional non-thermal component (III) becoming important at higher energies, possibly with a break around 1 TeV.

2.2.3 Origin of the emission

Short and long GRBs are suspected to be of different origins:

— the short GRBs are believed to be originating from the collapse of a binary system such as two neutron stars or a neutron star and a black hole, engendering two collimated jets;

— the long GRBs have been more observed, thus more studied, than the short ones. They have been linked to the death of massive stars: two collimated jets would produced when a supernova collapses to form a black hole.

In both cases, the jet is relativistic and is observed in the line of sight. Several models propose an explanation of this jet emission, assuming a thermal component, and a synchrotron emission (Band). To test them, one would need to access to more polarization measurements of the detected photons.

Their variation on short timescales (during flares, for blazars), their emission at high energies and their high redshift make flares of blazars and gamma-ray bursts excellent tools for testing time of flight of photons and for conducting measurements of a potential dispersion of light in vacuum. Blazars and GRBs present different observed characteristics (timescales, available energy range, etc.) as shown in Table 2.1. Short GRBs are expected to be the prime "guinea pigs" for LIV studies. Such analyses are presented in Chapters 7 and 8.

Property	Better if...	Gamma Ray Bursts	Blazars
Redshift	larger	**up to 8.2**	up to 0.6 [5]
Energy range of emission	higher extend	up to tens of GeV	**up to TeV**
Relevant time scales	narrower	**down to few tens ms**	minutes
Knowledge of intrinsic effects	better	uncertain	**moderate**
Example sources		GRB 090510 with *Fermi*	PKS 2155–304 with H.E.S.S.

Table 2.1: Comparative strengths of blazars and GRBs for constraining dispersion in (very) high energy photons. In blue, the most favorable characteristics. Adapted from presentations of V. Vasileiou.

Chapter 3

H.E.S.S.: A leading IACT

Contents

Ground-based γ-ray telescopes are optical telescopes with large collecting area, to detect Cherenkov light cones originated from cosmic rays (e.g. γ photons, leptons, hadrons) interacting with the atmosphere.

The type of an incoming particle (γ, lepton, hadron), its direction and energy are reconstructed using the shape of the projection of the shower with various techniques (geometrical methods, 2D or 3D model of the shower, ...).

This chapter focuses on the H.E.S.S. telescopes[1] and gives the main details needed to understand how the characteristics of the incoming gamma photons are measured, and separated from the background events (mis-identified leptons or hadrons).

1. The term "H.E.S.S.-1" will be used throughout this chapter to refer to the earlier design of four 12 m telescopes, and "H.E.S.S.-2" for the full array of 5 telescopes. Additionally, "H.E.S.S.-1 telescopes" refers to the 12-meter telescopes (CT1-4) and "H.E.S.S.-2 telescope" to CT5.

3.1 Atmospheric showers and IACTs

The atmosphere acts as a inhomogeneous calorimeter; at very high energies:

— a gamma photon or an electron/positron will trigger an electromagnetic shower with pair creation and Bremsstrahlung processes, engaging only photons and e^+/e^- (see Figure 3.1, left). The development of the shower is symmetric and isotropic (Figure 3.2, left and middle). The altitude of interaction and the lateral extension of the shower depend mainly on the energy of the impinging particle.
During their first interaction in the atmosphere, e^+/e^- lose energy through Bremsstrahlung: the associated Cherenkov emission starts generally higher.

— a hadron will trigger a more complex hadronic shower (eq. to a jet in a particle detector), involving more particles (see Figure 3.1, right). They lead to multiple electromagnetic sub-showers, developing randomly. They are generally more penetrating, and have a larger lateral extension than electromagnetic showers (see Figure 3.2, right).

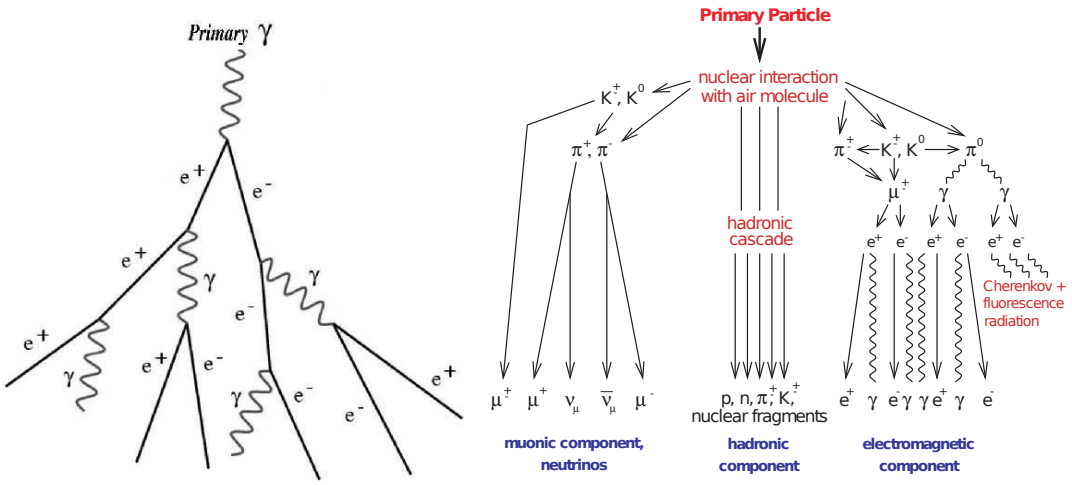

Figure 3.1: Schematic representations of electromagnetic showers (left, from [**?**]) and hadronic showers (right, from [35]).

The detection of the particle is done, in our case, by measuring the Cherenkov light pool parameters on the ground (extension, amplitude). When a charged particle travels faster than light in a particular dielectric medium, an electromagnetic radiation is emitted, in the near ultraviolet domain (wavelength $\lambda \sim 300 - 600\,\mathrm{nm}$). For the atmospheric showers mentioned above, it results in a Cherenkov light cone following the development of the shower, with an angle θ_C to the axis given by:

$$\theta_C = \arcsin\left(\frac{c}{nv}\right)$$

where v is the particle velocity, c the speed of light in vacuum, n the refractive index of this medium. The number of photons emitted is, in a first approximation, directly proportional to the energy of the incoming particle.

Most of the Cherenkov photons are emitted at the maximum development of the shower, *i.e.* at an elevation of $\sim 10\,\mathrm{km}$ [2]. Thus the observation of these photons requires an *early* detection:

2. $\sim 7\,\mathrm{km}$ for a 20 TeV photon and $\sim 12\,\mathrm{km}$ for a 20 GeV photon.

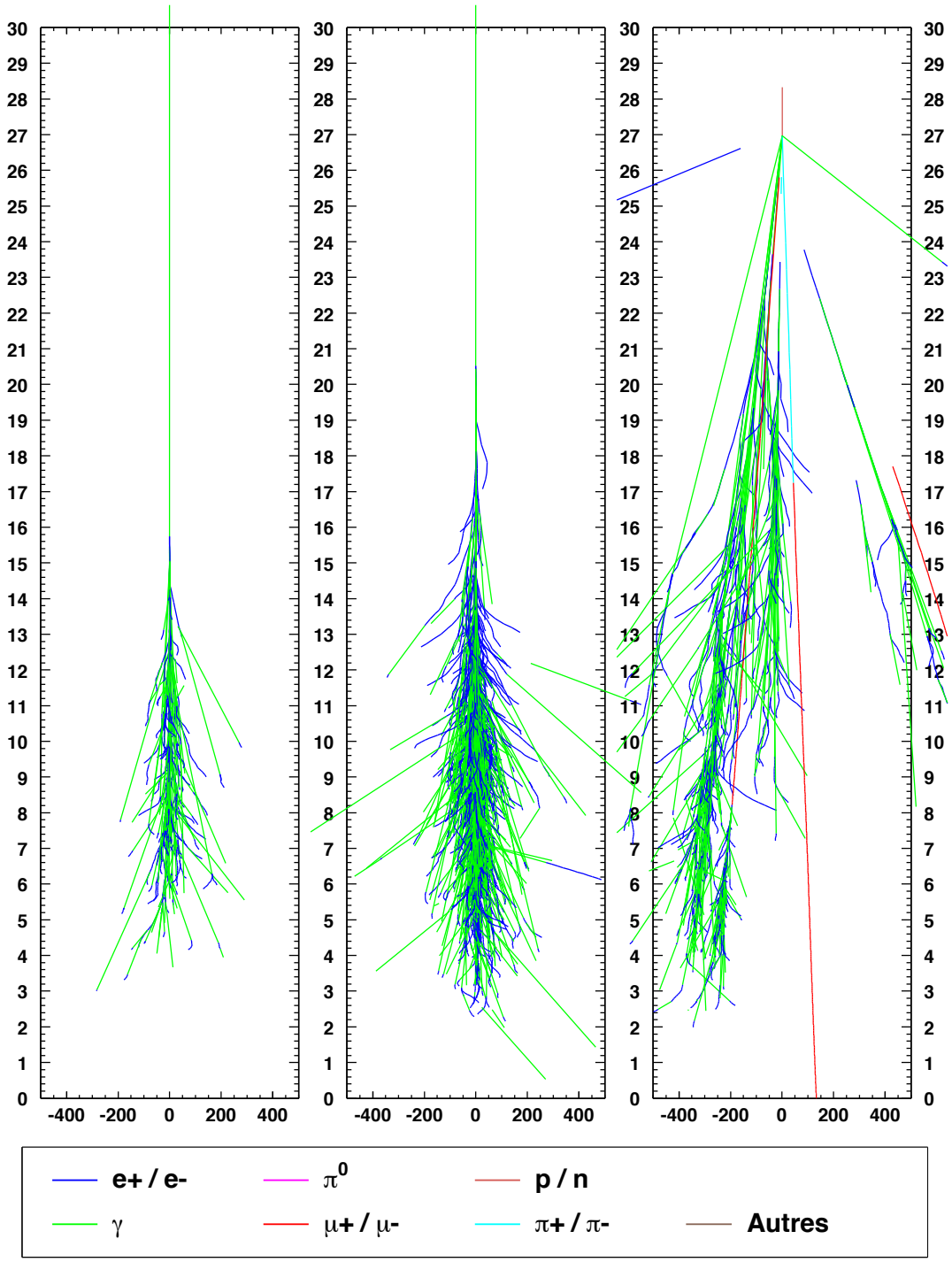

Figure 3.2: Simulated electromagnetic shower at 50 GeV (left), at 300 GeV (middle); simulated hadronic shower at 300 GeV (right). Hadron-initiated showers are more complex, as they lead to multiple sub-showers (muonic and electromagnetic components, besides the purely hadronic cascade). The development of these sub-shower is less predictable. They are generally more penetrating, have a larger lateral extension. Development of the hadronic shower differs from a shower to another. Here, it is shifted on the left. From [36].

to detect a sufficient amount of the Cherenkov light, the Cherenkov observatories are located high above the sea level.

The Cherenkov emission is very brief ($\sim$ ns). To observe these flashes, a *fast* detection is needed. This can be achieved using fast acquisition electronics.

Detecting very high-energy gamma rays requires huge collecting areas. For instance in order to detect a few gamma photons in one hour from the Crab Nebula above 1 TeV, the collecting surface should be about $10^4\,\mathrm{m}^2$. [3]

Large collecting areas and the detection of the fast Cherenkov flashes can be obtained by the Imaging Atmospheric Cherenkov Telescopes (IACTs) which use large dishes ($\sim 100\,\mathrm{m}^2$) with photomultipliers tubes (PMTs) in their focal points operated by fast (GHz) electronics. This approach was pioneered by Whipple [37].

The current generation of imaging Cherenkov telescopes benefits from improvements tested and validated by the second generation IACTs: finely pixelated cameras (CAT [38]) and stereoscopic observations (HEGRA [39]). Current IACTs include MAGIC [40], VERITAS [41] and H.E.S.S. [42]; table 3.1 compares their characteristics: location, altitude, number of telescopes composing the array, collecting area per telescope, total effective area, number of pixels per camera, field of view, and energy threshold. The energy threshold of a Cherenkov telescope, *i.e.* the minimum detectable energy of a particle, is function of the solid angle of the PMTs Ω, the integration time Δt, the average luminosity of the night sky ϕ_{NSB}, the effective area A and the optical efficiency ϵ:

$$E_{\mathrm{threshold}} \propto \sqrt{\frac{\Omega \Delta t \phi_{\mathrm{NSB}}}{A\epsilon}}$$

In the following section, the H.E.S.S. detector is described in more details.

Instrument	Lat. (°)	Long. (°)	Alt. (m)	n_{tels}	Area/tel. (m^2)	Tot. area (m^2)	Pixels	FoV (°)	Thresh. (TeV)
H.E.S.S.	-23	16	1800	5	107 & 614	1042	960 & 2048	5 & 3.2	0.05
VERITAS	32	-111	1275	4	106	424	499	3.5	0.05
MAGIC	29	18	2225	2	236	472	1039	3.5	0.03
Whipple	32	-111	2300	1	75	75	379	2.3	0.3
HEGRA	29	18	2200	5	9	43	271	4.3	0.5
CAT	42	2	1650	1	18	18	600	4.8	0.25

Table 3.1: Comparison of the H.E.S.S. telescopes with selected IACTs: location, altitude, number of telescopes composing the array, collecting area per telescope, total effective area, number of pixels per camera, field of view, and energy threshold. Two numbers are provided for H.E.S.S. to distinguish between the four 12 m telescopes and the 28 m telescope. Adapted from [43].

3. These huge collecting areas can be obtained on Earth; the constraints on the satellite detectors specifications do not allow such area, and thus the detection of photons with such energies, in space.

3.2 The H.E.S.S. array

The High Energy Stereoscopic System (H.E.S.S.) is an array of Imaging Atmospheric Cherenkov Telescopes (IACT) located in the Khomas Highland in Namibia. It is composed of a total of five telescopes: four 12 m telescopes and one 28 m telescope. The site has been chosen for the high optical quality of the atmosphere, and for it is an excellent location – close to the Tropic of Capricorn – to observe most of the Galactic plane.

The first 12 m telescope was finished in June 2002. The first phase of the array, with the four 12 m telescopes [4] started in December 2003. The fifth, 28 m, telescope saw its first light in July 2012: this is the start of the second phase of the experiment [5].

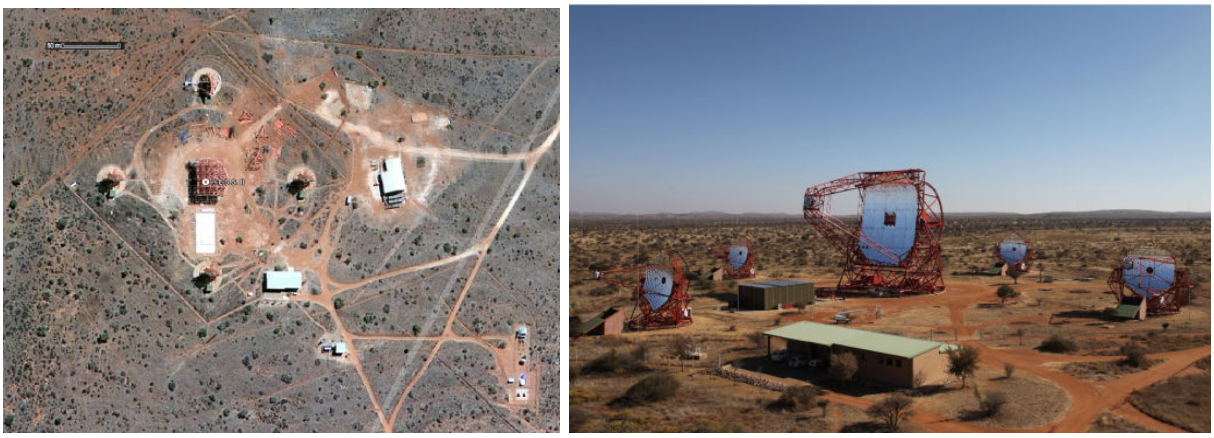

Figure 3.3: Satellite view of the H.E.S.S. site (extracted from Google maps) and photograph of the full H.E.S.S. array: CT1-4 on the corners and CT5 in the middle.

Figure 3.3 (left) shows a satellite view of the site: the four 12 m telescopes form a square of side 120 m; CT5 is in the center of the square. The distance between the four medium telescopes was set so that they are close enough to allow several images of the same atmospheric shower, and far enough in order to get a better stereoscopic reconstruction and a higher total effective area.

Figure 3.3 (left) shows a photograph of the five telescopes. Each dish of CT1 to CT4 is composed of 380 spherical mirrors (⌀60 cm) totalizing 107 m^2 and arranged on a Davis-Cotton mount in order to reduce the coma aberration of the telescope. A drawback of this layout is that it induces an anisochronism, increasing quadratically from the center to the edge of the dish (up to 5 ns). The dish of CT5 is composed of 875 hexagonal mirrors (90 cm flat to flat) totalizing 614 m^2. The shape of the dish is parabolic; considering its size, a Davis-Cotton mount would have entailed anachronisms of up to 9 ns on the edges of the dish.

3.2.1 Cameras

The cameras, at the focal point of the dishes, are finely pixelated: 960 (CT1–4) and 2048 (CT5) PMTs (also called pixels), allowing the record of the fine structure of the image of an atmospheric shower. They are operated by a fast electronic to allow for proficient rejection of the background events (∼ a thousand background events for every gamma photon).

4. CT1–4 ≡ H.E.S.S.-1
5. CT1–4 + CT5 ≡ H.E.S.S.-2

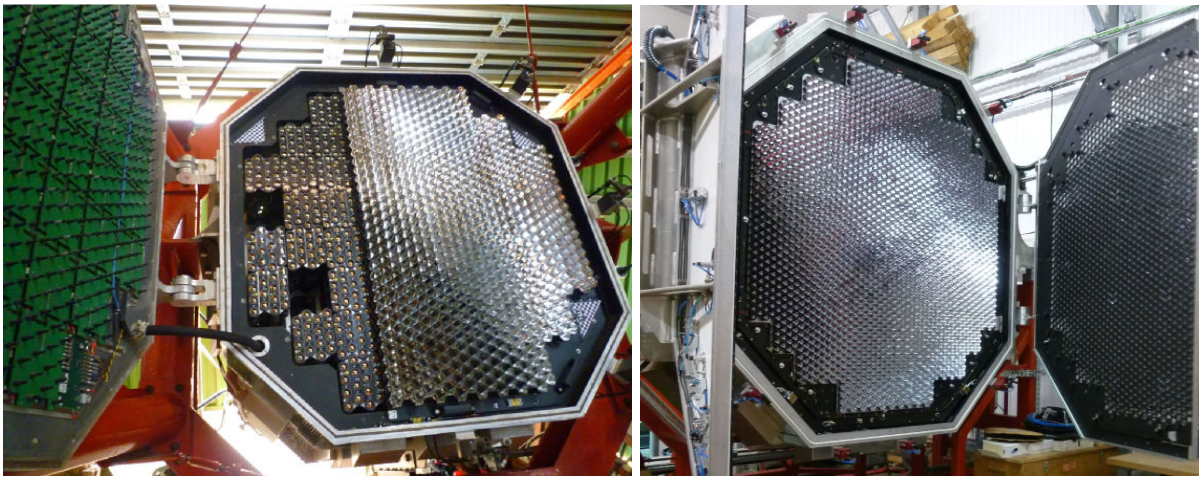

Figure 3.4: Photographs of a H.E.S.S.-phase 1 camera (left, showing the drawers, *i.e.* the groups of 16 pixels) and CT5 (right).

Each PMTs is completed by a Winston cone in order to limit their field of view to the size of the dish, to reduce the empty space between the PMTs and to cut the light coming from the side of the camera and from the ground. CT1–4 PMTs have a solid angle of 0.16°, leading to a total field of view of 5° for these telescopes; CT5 PMTs have a solid angle of 0.07°, leading to a total field of view of 3.2°.

The PMTs are put together in *drawers*, groups of 16 pixels: 60 drawers for CT1-4 and 128 drawers for CT5. Each drawer is controlled by two analogic cards (2 × 8 PMTs) and one slow control card. The signal from each PMT is split in two sampling channels (and one trigger channel): the low gain channel covers signal from 15 to 600 photo-electrons, the high gain channel covers signal from 1 to 150 photo-electrons. The common range will be used to intercalibrate the two channels. For each channel, the amplified signal is stored in analogical memories (**A**nalog **R**ing **S**ampler for CT1–4 and **S**wift **A**nalog **M**emory for CT5) which sample the signal in 128 cells (CT1–4) or 256 cells (CT5) at a rate of 1 GHz [6]. When the sector triggers, the amplitudes of 16 cells are read and summed (this corresponds to 16 ns); this aggregated signal is then digitalized by an Analog-to-Digital Converter (ADC). The total dead time is 64 μs for CT1-4 and 1.5 μs for CT5. The acquisition for the gain in both channels for CT1–4 is illustrated in Fig. 3.5; the acquisition system is similar for CT5, with SAM chips instead of ARS and different values of the gains.

Additionally, CT5 provides timing informations for each channel (high/low gain), thanks to the enhanced capabilities of the analog cards: the time of the maximum charge (TOM) and the time above threshold, allowing to derive the signal duration in each pixel. These improvements are used to clean the image of the showers; a time-dependent analysis/reconstruction algorithm is also being worked on.

3.2.2 Trigger

Different levels of trigger exist. In the first level, the cameras are divided in sectors; a minimum number of pixels in a sector should exceed a given charge threshold in order to trigger the acquisition by this sector. The first level trigger rate is of about 1 kHz for CT1–4 and a few dozen kHz for CT5.

6. SAM chips allow for a higher sampling rate, up to 3 GHz.

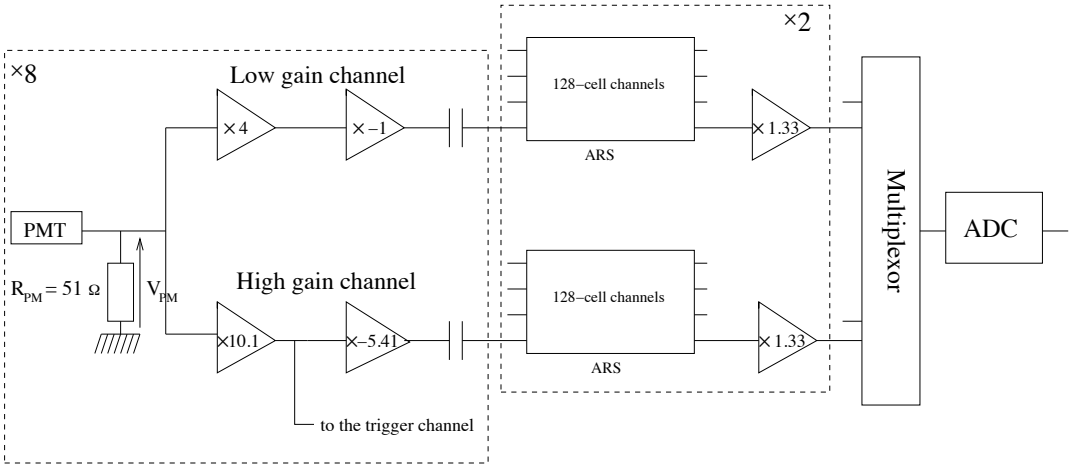

Figure 3.5: Charge acquisition in both channels for one acquisition card (8 PMTs) of CT1–4 (from [44]).

A second level is required to reduce this trigger rate. Two strategies are implemented:

— *hybrid* mode: several telescopes should trigger. This allows to reach an energy threshold down to 50 GeV.

— *mono* mode: below 50 GeV, H.E.S.S.-1 telescopes are not able to trigger anymore. In this mode, the observation is triggered by CT5 alone.

The times of each trigger/observation are synchronized by a time-stamp card, to associate a unique number to each event detected by different cameras.

3.2.3 Observations

There are several types of data-taking:

— dedicated measures to calibrate the data and correct for deviation from nominal values. This includes flatfield measurements, single photo-electron response, autofocus (CT5).

— observation of actual γ sources: physics runs and pointing runs. These observations are performed during the night, after the twilight and before the dawn, when the moon is hidden beyond the horizon. Physics runs are observations of target sources of physical interest; they are also used to estimated the NSB noise and the hadron contribution. Pointing runs are taken so as to correct the measured direction of sources, taking in consideration the deformation of the structure of the telescopes.

The target physics sources are chosen by the Observation Committee (OC), based on proposals by the members of the collaboration. Targets include:

— point-like extragalactic sources, such as blazars; an effort is being made toward observing Gamma ray Bursts emission with CT5.

— point-like and extended galactic sources;

— diffuse emissions (intra- and extragalactic).

3.3 Calibrating the data

Here the calibration process is described in order to understand how the raw data is obtained before the reconstruction (section 3.5) and also to introduce the run quality studies performed (chapter 4).

3.3.1 Overview

The total measured Cherenkov light of an event detected by a H.E.S.S. camera is not known immediately. It is stored in ADC counts for each pixel: the aim of the calibration is to convert this measurement to a number of Cherenkov photons actually detected by a pixel.

A first part is to get the number of photo-electrons (p.e.); it involves the following steps:

— determination of the pedestal, *i.e.* the electronic baseline, for each channel (low gain and high gain);

— measure of the high gain coefficient, from a single photo-electron spectrum;

— measure of the ratio high gain over low gain from physics runs. Indeed, the low gain is measured indirectly from the high gain.

— determination of the flatfield coefficients, *i.e.* correction of the inhomogeneity of the camera (differences in measured p.e. by the different pixels for a same input signal);

The calibrated charge in p.e. ("intensity") of an event in the high gain channel I^{HG} is thus obtained from the ADC count ("charge") in this channel ADC^{HG}:

$$I^{HG} = \frac{ADC^{HG} - P^{HG}}{\gamma_e^{ADC,HG}} \times FF$$

with P^{HG} the pedestal (retrieved from dedicated runs), $\gamma_e^{ADC,HG}$ the high gain (directly measured on data), and FF the flatfield coefficient specific to the considered pixel (retrieved with dedicated measurements). The low gain cannot be calculated directly; it is obtained from the high gain:

$$I^{LG} = \frac{ADC^{LG} - P^{LG}}{\gamma_e^{ADC,HG}} \times (HG/LG) \times FF.$$

The ratio HG/LG of the high gain over low gain is measured directly on data in the overlapping range between the two channels.

An additional step toward absolute calibration consists in converting the number of photo-electrons in term of actual Cherenkov photons reaching the PMT of the pixel, *i.e.* to measure the optical efficiency of the system [mirror + Winston cone + atmosphere]. This is done using images of measured muons.

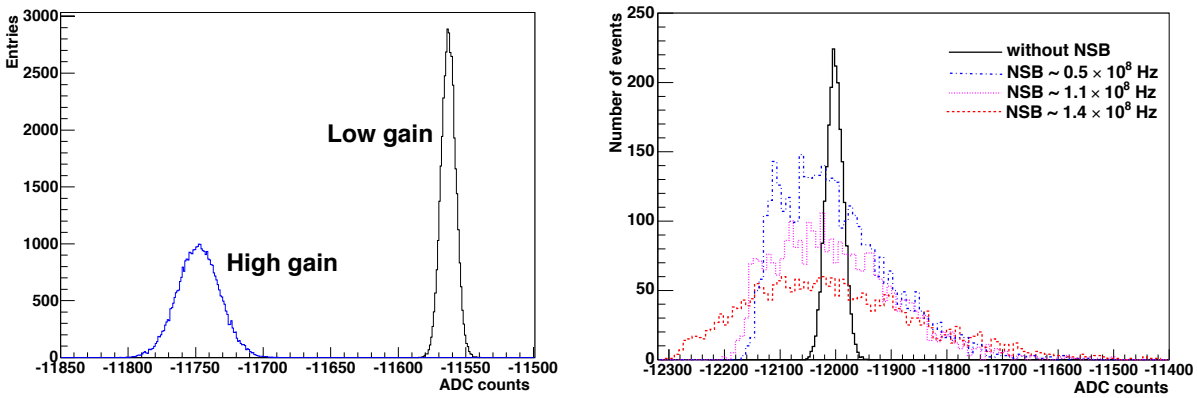

Figure 3.6: Left: Distribution of the ADC counts measured in absence of Cherenkov signal for both channels. The mean of each distribution gives the position of the pedestal: here $P^{HG} \simeq -11750$ and $P^{LG} \simeq -11560$ ADC counts. Right: The distribution of the pedestal gets larger with increasing NSB light. From [44].

3.3.2 Pedestal estimation

The pedestal value is the number of ADC counts measured when there is no Cherenkov signal. Two components account for the pedestal: the electronic noise of the apparatus and the night sky background (NSB).

Electronic pedestal

The electronic pedestal is measured with the lid closed, without any external source (LED or sky). ADC counts are recorded in both channels, high gain and low gain. Figure 3.6 (right) shows such distributions obtained in both channels, superimposed. The distribution for a given channel is centered on the value of the pedestal (P^{HG} and P^{LG}).

Night sky background

The ambient light and the stars light modify this nominal value of the pedestal. The variation of the pedestal due to the NSB is measured during the observations: for each event recorded, only the pixels not reached by the Cherenkov light (non-triggering pixels) are considered. The mean of the pedestal is calculated regularly during the night/the run, when enough events are recorded. Figure 3.6 (right) shows the ADC distribution of the pedestal for various NSB intensities. The more the NSB contribution, the wider the pedestal distribution.

Common modes

An other correction is applied for CT1-4 cameras: a shift of the electronic pedestal is observed between the two halves of a camera. This is due to a capacitive coupling between the power unit and the acquisition system. This effect affects mainly the low gain channel. The study and the correction of this effect are explained in [45].

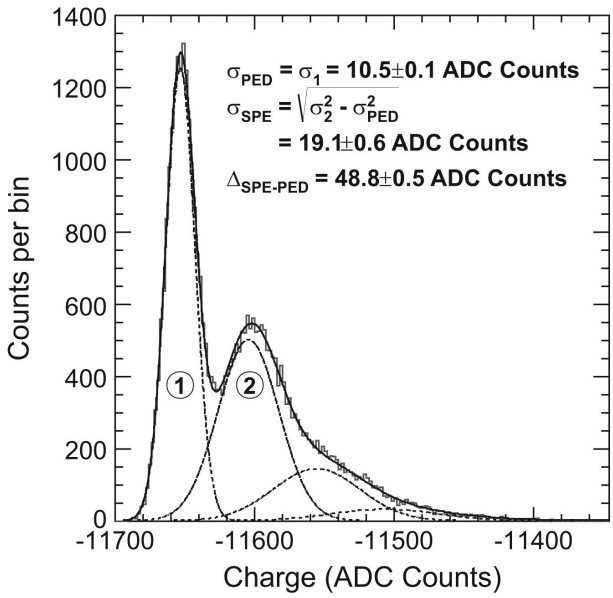

Figure 3.7: ADC counts distribution corresponding to a single photo-electron, for a CT5 PMT in the high gain channel. The full line is a fit with function 3.1. The dotted lines show the separate components, including the pedestal distribution (peak 1) and the 1 p.e. distribution (peak 2). From [46].

3.3.3 ADC to PE coefficients

High gain channel

The high gain coefficient $\gamma_e^{ADC,HG}$ is measured from dedicated runs, using a LED (+ a diffuser) illuminating the whole camera at low intensity, close to a single photo-electron. A series of pulses of mean of 1 p.e. is emitted. The ADC count are recorded for the series. An example of the obtained ADC distribution is shown in Figure 3.7. This distribution can be fitted using a sum of Gaussian functions [47]:

$$\mathcal{G}(x) = N \times \left(\frac{e^{-\mu}}{\sqrt{2\pi}\sigma_P} \exp\left[-\frac{1}{2} \left(\frac{x - P^{HG}}{\sigma_P} \right)^2 \right] + N_S \sum_{n=1}^{m \gg 1} \frac{e^{-\mu}}{\sqrt{2\pi n}\sigma_{\gamma_e}} \frac{\mu^n}{n!} \exp\left[-\frac{1}{2} \left(\frac{x - (P^{HG} + n\gamma_e^{ADC,HG})}{\sqrt{n}\sigma_{\gamma_e}} \right)^2 \right] \right) \tag{3.1}$$

The first term corresponds to the pedestal distribution (mean P^{HG}), the second term to a sum of the distributions obtained with 1, 2, ... n photo-electrons; each such distribution has a mean of $P^{HG} + n\gamma_e^{ADC,HG}$. Thus the gain $\gamma_e^{ADC,HG}$ can be obtained as the relative position of the means of the pedestal and the single photo-electron peak (n = 1).

Low gain channel

The low gain channel is not sensitive enough to enable a direct measurement of the coefficient using the same method. It is calculated from the high gain coefficient; the ratio between the two channels is calculated from the observation data itself, in their overlaping sensitivity range

(between about 30 and 150 p.e. for CT1-4). In this range, the amplification is linear for the two channels: the simultaneous measure of the ADC counts in both channels ADC^{HG} and ADC^{LG}, combined with the previous measure of the pedestal values P^{HG} and P^{LG} allow the calculation of

$$HG/LG = \frac{\gamma_e^{ADC,HG}}{\gamma_e^{ADC,LG}} = \frac{ADC^{HG} - P^{HG}}{ADC^{LG} - P^{LG}}.$$

3.3.4 Flatfield coefficients

The flatfield coefficients FF, correcting the relative difference in the light collection between the pixels, is measured from dedicated runs, using a LED (+ a diffuser) illuminating the whole camera uniformly. The mean intensity on the pixel $< I >_{\text{Pixel}}$ and the mean intensity on the whole camera $< I >_{\text{Camera}}$ are measured. For each pixel, the flatfield coefficient is then:

$$FF = \frac{< I >_{\text{Camera}}}{< I >_{\text{Pixel}}}.$$

3.3.5 Collection efficiency

To obtained the absolute energy scale calibration, one need to know the system collection efficiency, which takes into account the mirrors, the Winston cones and the absorption of the Cherenkov photons is the lower part of the atmosphere. This is done using images of muons going through or falling on the side of a telescope.

Each image of a muon is fitted with a ring model with the collection efficiency and the ring width as free parameters. The measure (*i.e.* the fit) of the collection efficiency is done on a regular basis during observations. It allows to monitor the degradation of the mirrors (and the Winston cones) over time. Figure 3.8 shows its evolution for CT2. The mirrors were replaced in 2010: this manifests as a rise of the efficiency, around run 61000.

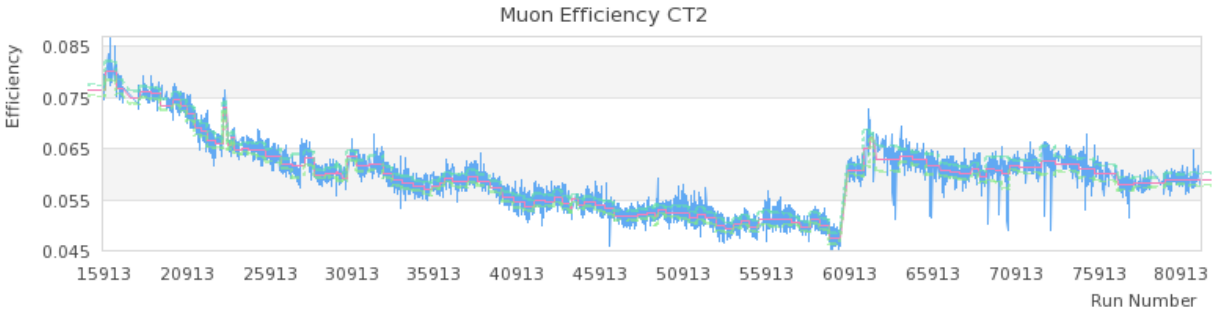

Figure 3.8: Optical efficiency of CT2 as a function of the run number (eq. of the time). The rise around run 61000 is due to the replacement of the mirrors in 2010. Figure from [48].

3.4 Selecting the data: quality criteria

Global (array) and local (per telescope) criteria exist to assess the quality of data from the first phase of H.E.S.S. (4 telescopes). The global criteria include:

— the run duration: only runs of 5 minutes or more are considered in the analyses. While a typical run last about 28 minutes (± 1 min), shifters on site can decide to stop an ongoing

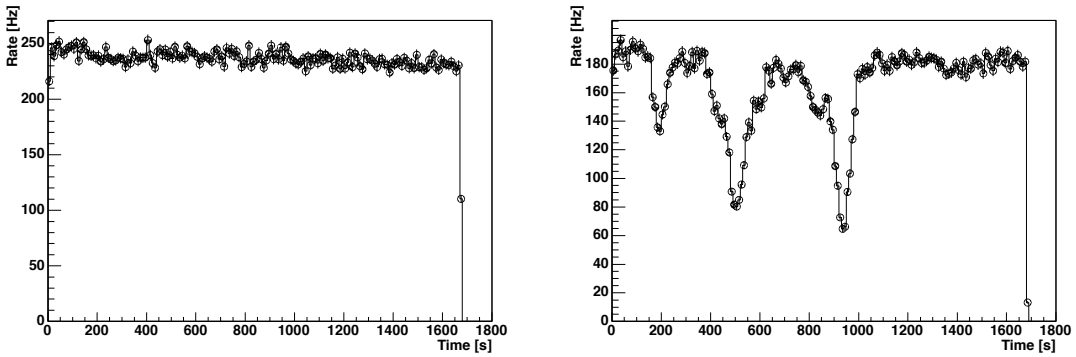

Figure 3.9: In stable meteorological conditions, the system trigger rate is stable (left); when clouds are passing in the field of view, sharp decreases in the trigger rate are observed (right). Figures from [49].

observation, in case of technical problems with a telescope or for other issues with the data acquisition system (DAQ).

— the dead time: it has to be known accurately in order to properly evaluate the measured photon fluxes. The system dead time depends on the multiplicity of the trigger (number of participating telescopes) and on the required trigger threshold. For two participating telescopes and 2.5 pixels with a minimum intensity of 4 p.e., the system dead time fraction is of the order of 10 %. A higher fraction, of the order of 20 %, means that an issue occurred during the acquisition: the run is rejected.

— the system trigger rate: it can be affected by the atmospheric and meteorological conditions. Clouds in the field of view lead to a decrease of the trigger rate during a run, as seen in Fig. 3.9. Thus, a minimum trigger rate of 100 Hz at zenith [7] is required, as well as a maximum dispersion of the rate of 4% between the beginning and the end of the run. Variations of the trigger rate over long periods are normal (aging of the mirrors) and are taken into account in the calibration process (correction using the images of muon rings).

Selection and cuts on per-telescope variables include:

— the Mean and RMS over the camera of the per-pixel raw data distribution (ADC counts)

— the number of broken pixels: the term “broken” only means that the corresponding photomultipliers were either deactivated (due to the presence of a bright star in the field of view) or not responding due to a hardware issue;

Recent developments have been made on the understanding of the monitoring of the atmosphere:

— use of dedicated instruments (LIDAR),

— study of the transparency coefficient.

These criteria can be applied on runs involving CT5. Additionally, we would like to get an idea of the quality of the calibration on its whole, including broken pixels, pedestal variations, flatfield, High gain-to-low gain ratio, gain (ADC to pe). A study of the calibrated charge has been performed and is detailed in next chapter (4).

7. the cut value is corrected for the zenith angle

3.5 Reconstruction and analysis

The analysis of the raw data, including the reconstruction of the direction of the events, the conversion of the total calibrated charge into energy of the particle, and the identification of the particle triggering the shower, was made using the software ParisAnalysis, developed mainly by Mathieu de Naurois. Two versions were used: ParisAnalysis 0-8-22 and ParisAnalysis 0-8-24. Main different between the two versions: in ParisAnalysis 0-8-24, a recalculation of the pointing allowed to get a better reconstruction of the direction of the showers, leading to an increase of the excess [8], up to 40 %.

3.5.1 Reconstruction

3.5.1.1 Simulation of camera images induced by atmospheric showers

The reconstruction methods presented in next subsections rely strongly on Monte-Carlo simulations of atmospheric showers and their detection by H.E.S.S. (response of the instrument).

Simulations of atmospheric showers

The simulation of atmospheric showers is done using KASKADE [50], a code developed for Whipple, with a further improvement of the propagation model [51]. The propagation is simulated for each individual particle. It takes into account the different interaction processes, the pair production cross-section, the energy losses (ionization, Bremsstrahlung, positrons annihilation, inelastic scattering), the multiple diffusion and the effects of the Earth magnetic field. The Cherenkov emission is computed along the track as the considered particle travels across the atmosphere. The Cherenkov photons absorbed by the atmosphere, or falling outside the finite wavelength range of the PMTs, or reaching the ground instead of a telescope dish, are not considered. Only the remaining photons are stored in file.

Response of the instrument

The simulation of the detector is done using `SMASH`, a H.E.S.S.-dedicated code, and incorporates the following parts of the telescopes: reflexivity of the mirrors, the conversion of the Cherenkov photons by the PMTs and their processing by the acquisition system. The particular geometry of each telescope (*e.g.* shadow from the mount and the camera) is taken into account.

3.5.1.2 Hillas reconstruction

A reconstruction method using geometrical properties of the images of atmospheric showers in the camera was developed and first applied on the data of Whipple telescopes [52]. Each image of a shower in the camera is assumed to be an ellipse. Figure 3.10 (left) shows a schematic representation of such an image recorded in the camera (see "Telescope 1 image"), with the following extracted variables, called the *Hillas parameters*:

— the width w and the length l of the ellipse;

— the image barycenter;

— the distance ("Distance") between the image barycenter and the center of the camera.

Additional information per camera include the image amplitude and higher order moments (*e.g.* skewness).

8. The excess s is defined from the comparison between ON-source and OFF-source region, as seen latter in paragraph 3.5.2: $s = n_{\mathrm{ON}} - \alpha n_{\mathrm{OFF}}$. It can also be obtained from the angular distribution – see *e.g.* Fig. 7.1 in Chapter 7 – by determining the background contribution away from the source (*e.g.* at $\theta^2 > 0.02\,\mathrm{deg}^2$) and extrapolating around $\theta^2 = 0\,\mathrm{deg}^2$.

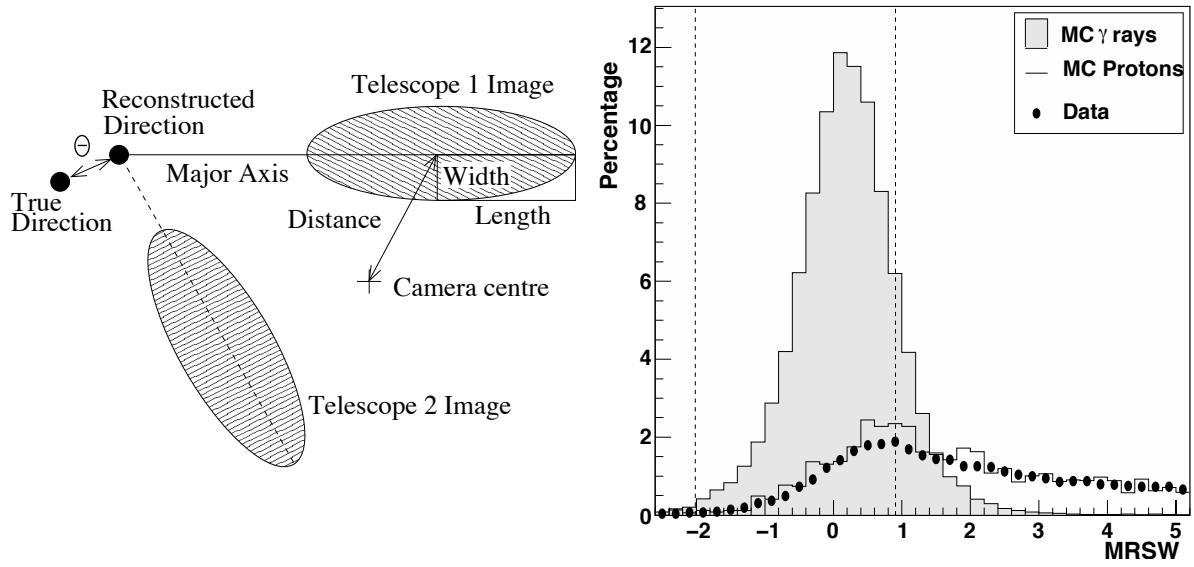

Figure 3.10: Left: Definition of the Hillas parameters. Right: Distribution of the Mean Scaled Width for simulated gammas (gray), simulated protons (line) and OFF-source data (dots). The distribution of the MSW for the data and the simulated protons are in excellent agreement. The vertical lines correspond to standard cuts on MSW. Figures from [49].

For stereoscopic observation (several telescopes in use), additional information comes up:

— the direction of the primary particle, determined from the intersection of the major axes from each telescope image;

— the angle θ between the reconstructed and the expected position of the source;

— the impact parameter, *i.e.* the intersection of the direction of the axes in the shower images obtained from the different telescopes.

The width w and the length l of the ellipse are used to distinguish between photons and hadrons. They are scaled to allow a comparison with expected distributions for gammas and hadrons, and also to take into account the fluctuations arising in the shower development. For a telescope, the Scaled width SW and the Scaled Length SL are:

$$SW = \frac{w - < w >}{\sigma_w}$$

$$SL = \frac{l - < l >}{\sigma_l}$$

with $< w >$ (resp. $< l >$) the mean of the widths (of the lengths), and σ_w (σ_l) their standard deviation.

When using several telescopes (stereoscopic observations), the variables are averaged over the telescopes; the Mean Scaled width MSW and the Mean Scaled Length MSL are:

$$MSW = \frac{1}{n_{\text{tels}}} \sum_{i=1}^{n_{\text{tels}}} SW_i$$

$$MSL = \frac{1}{n_{\text{tels}}} \sum_{i=1}^{n_{\text{tels}}} SL_i$$

The distributions of these two scaled variables strongly depends on the type of primary particle (photon, hadron). Figure 3.10 (right) shows the distribution of the Mean Scaled Width for simulated gammas (gray), simulated protons (line) and OFF-source data (dots). The distribution of the MSW for the data and the simulated protons are in excellent agreement. Cuts are applied on these variables to select the gamma-like events, while rejecting a good proportion of hadrons. For a source with a spectral energy distribution $\Lambda(E) \propto E^{-2}$ observed with H.E.S.S., the cuts on these parameters are:

$$-2 \leq MSW \leq 0.9$$

$$-2 \leq MSL \leq 2$$

3.5.1.3 Model analysis

A more powerful reconstruction procedure, making the most use of the finely pixelated cameras, is based on a comparison of the actual shower images detected in the camera with camera images of showers simulated with a semi-analytical model. First developed for the reconstruction of CAT observations [53], the procedure was further developed and adapted for analyzing H.E.S.S. data.

The model is explained in detail in [54]. It takes into account the electron spectrum, their angular distributions, their position *wrt* the axis of the shower. The distributions of these parameters is obtained from Monte-Carlo simulations and then fitted to get analytical expressions. The particle response of the atmosphere and the detector is taken in consideration. The model predicts *in fine* the amount of light collected by each pixel of a camera.

Fitting procedure

The principle of the fitting procedure is to compare the actual amplitude measured in a pixel by its prediction from the model. For each pixel i, the likelihood/probability $P_i(s|\mu, \sigma_P, \sigma_{1\,\mathrm{p.e.}})$ to get a given signal s with an amplitude μ, pedestal width σ_P, single photo-electron width $\sigma_{1\,\mathrm{p.e.}}$ is computed. The *telescope likelihood* is obtained by multiplying individual pixel likelihoods over all the pixels in the camera:

$$L_{\mathrm{tel}} = \prod_{i=1}^{n_{\mathrm{pixels}}} P_i(s|\mu, \sigma_P, \sigma_{1\,\mathrm{p.e.}}).$$

Non operational ("broken") pixels are not taken into account in this product. The fitted parameters (not shown in this expression) are the direction and the impact parameter of the shower, the depth of the first interaction, and the energy of the impinging particle.

A variable is constructed so as to estimate the quality of the fit and to discriminate between gamma-like events and hadrons: the *goodness-of-fit* is the normalized sum of the log-likelihood. To make the most of the differences between showers originating from gamma photons and hadrons, the pixels are classified in two categories:

— the pixels corresponding to the core of the shower image are used to construct the *ShowerGoodness*;

— the pixels corresponding to the rest of the camera are used to construct the *BackgroundGoodness*;

Cuts on these two variables allow to efficiently remove background events while keeping most gamma-like events.

Analysis cuts

Different sets of cuts exist depending on the source at study. The two considered during the H.E.S.S. analysis of AGNs used for the LIV studies are the "Standard" cuts and the "Loose" cuts; the latter is optimized to have an increase in the effective area (more excess), at the loss of a worse background rejection (smaller S/B ratio):

	Standard cuts	Loose cuts
Total intensity of the image in the camera	> 60 p.e.	> 40 p.e.
ShowerGoodness	< 0.6	< 0.9
Depth of first interaction	$\in [-X_0, 4X_0]$	–
Squared angular distance	< 0.01 deg^2	< 0.0125 deg^2

Additionally, common cuts are applied:

— the images of at least two telescopes should follow the first two conditions (minimum intensity and maximum Shower goodness value);

— the maximum distance between the barycenter of the shower image and the center of the camera is set to 2°.

Performances

The performances of Model *vs.* Hillas reconstruction for H.E.S.S.-1 are the following:

— The effective areas (Figure 3.11) are similar for the two reconstruction methods for Std cuts (minimum of 60 p.e. in the camera). Using Loose cuts (required minimum of 40 p.e.) allow to get a lower threshold and a larger effective area at low energies.

— The energy resolution (Figure 3.12, left) is better than 12 % for the whole energy range, compared to a maximum 15 % for Hillas reconstruction.

— Energy biases (Figure 3.12, right) are less than 5 % above 100 GeV, and definitely smaller than Hillas' is this range. However, it increases drastically at lower energies, up to 20 % at 80 GeV.

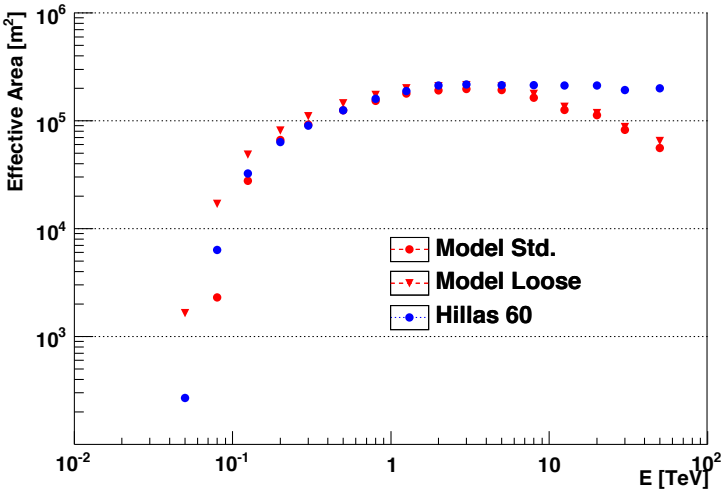

Figure 3.11: Effective area as function of the energy (at zenith) for Model (Std and Loose cuts) and Hillas (Std cuts) reconstructions. Figure from [55].

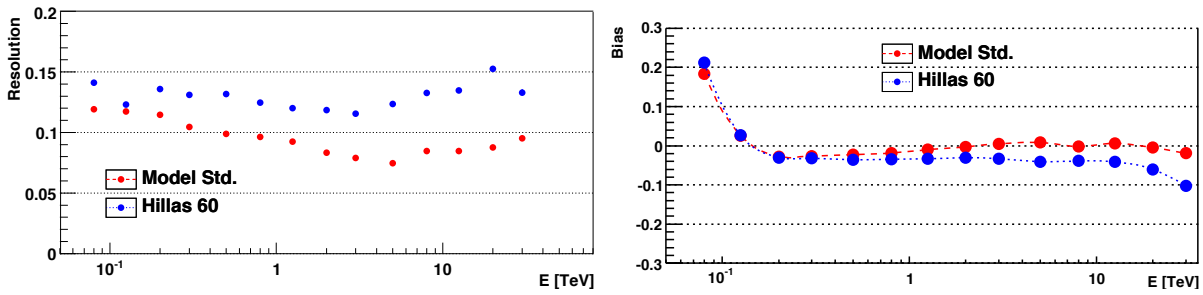

Figure 3.12: Energy resolution (left) and bias (right) as function of the energy (at zenith) for Model (Std cuts) and Hillas (Std cuts) reconstructions. Figure from [55].

3.5.2 Background subtraction

The reconstruction of the events provides the direction and energies of all the gamma-like events within the field of view. It does not discriminate between the gammas originating from the source at study and photons coming from diffuse emissions. Also, in spite of the rejection algorithm, the data is still contaminated by π^0 decay from proton showers, misidentified electrons, or heavy elements such as helium.

The comparison with an OFF-source region allows to estimate the level of background remaining in the region of interest. In particular, the *Multiple-OFF* subtraction method makes use of observations in *wobble* mode. Figure 3.13 shows the principle of this subtraction method: the ON-source region (striped lines), centered on the position of the source, is offset (here by 0.5°) *wrt* the pointing direction. Several OFF-source regions (in yellow) can be defined, offset by the same amount. Thus the ON- and OFF-source regions share the same instrument response (*e.g.* same radial acceptance).

The estimated numbers of signal events s (the excess) and background events b present in the ON region are retrieved from the number of events in the ON region n_{ON}, the total number of events in all the OFF regions n_{OFF}, and the ratio α of the ON-source area to the (summed) OFF-source area: $s = n_{ON} - \alpha n_{OFF}$ and $b = \alpha n_{OFF}$

Other estimations of the background exist – other shapes using wobble observations, estimation with a ring-shaped region around the region of interest, ON-OFF alternated observations – and are not described here.

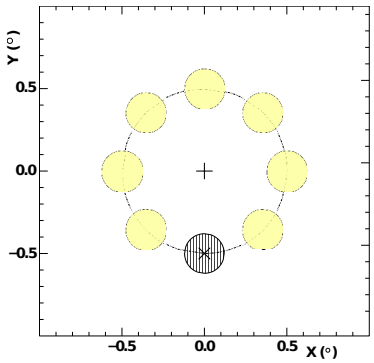

Figure 3.13: Principle of the *Multiple-OFF* subtraction method. The telescope observe in *wobble* mode: the ON-source region (striped lines), centered on the position of the source, is offset (here by 0.5°) *wrt* the pointing direction. This allows to define several OFF-source regions (in yellow) which are offset by the same amount. Thus the ON- and OFF-source regions share the same instrument response (*e.g.* same radial acceptance). Figure from [49].

3.5.3 Significance of the excess

To measure the significance of the excess relative to the background, Li and Ma [56] proposed the following test.

Two parameters are unknown: the expectation $< s >$ of the number s of signal photons and the expectation $< b >$ of the number b of background events. The null hypothesis (H_0) tested is that "all the observed events are background events", *i.e.* $(H_0) :< s >= 0$, modeled by the likelihood function $L(n_{ON}, n_{OFF}|H_0)$. The alternate hypothesis (H_1) is "some of the observed events are signal events", *i.e.* $(H_1) :< s >\neq 0$, modeled by the likelihood function $L(n_{ON}, n_{OFF}|H_1)$.

In the general case, the expected number of signal and background events is obtained from a comparison of ON-source and OFF-source regions, with α accounting for the ratio of the ON-source time to the OFF-source time[9]:

$$\begin{aligned} < s >= & \quad n_{\mathrm{ON}} - \alpha n_{\mathrm{OFF}} \\ < b >= & \quad \alpha n_{\mathrm{OFF}} \end{aligned} \tag{3.2}$$

In the specific case of (H_0) being true, *i.e.* in the case of no signal events in the ON source region, the expected numbers of signal and background events become:

$$\begin{aligned} < s >= & \quad 0 \\ < b >= & \quad \tfrac{\alpha}{1+\alpha}(n_{\mathrm{ON}} + n_{\mathrm{OFF}}) \end{aligned} \tag{3.3}$$

This allows to get explicit expressions of $L(n_{ON}, n_{OFF}|H_0)$ and $L(n_{ON}, n_{OFF}|H_1)$. It follows that the maximum likelihood ratio eventually reads as:

$$\lambda \equiv \frac{L(n_{ON}, n_{OFF}|H_0)}{L(n_{ON}, n_{OFF}|H_1)} = \left[\frac{\alpha}{1+\alpha}\left(\frac{n_{\mathrm{ON}} + n_{\mathrm{OFF}}}{n_{\mathrm{ON}}}\right)\right]^{n_{\mathrm{ON}}} \left[\frac{1}{1+\alpha}\left(\frac{n_{\mathrm{ON}} + n_{\mathrm{OFF}}}{n_{\mathrm{OFF}}}\right)\right]^{n_{\mathrm{OFF}}}$$

If (H_0) is true, and since (H_0) involves only 1 parameter ($< s >$), $-2\ln\lambda$ will asymptotically follow a χ^2 distribution with 1 degree of freedom. In this case, the significance S of the observed results is taken as:

$$S = \sqrt{-2\ln\lambda}$$

When a source is detected (significance above $5\,\sigma$), it is possible to perform further analysis of the data, such as morphological and spectral analyses. The morphological analysis[10] is performed by doing a likelihood fit of the reconstructed events' directions to a pre-assumed shape of the source. Similarly, the spectral analysis is performed by doing a likelihood fit of the reconstructed events' energy, assuming a defined shape of the spectral distribution. So far these analyses are performed separately. A common fit of both the morphology and the spectral shape is planned to be implemented in ParisAnalysis framework.

9. In the case of the *Multiple-OFF* subtraction described in the previous paragraph, α does not account for the ratio of the ON-source time to the OFF-source time, but for the ratio of the ON-source area to the (summed) OFF-source area.

10. The morphological analysis is not described here as it was not used in this work. A detailed description of the procedure can be found in [57].

3.5.4 Spectral reconstruction

The spectral reconstruction of a source is achieved using a forward-folding method [58]. It relies on a log-likelihood comparison of the ON-source and OFF-source events.

A spectral shape $\Lambda(E)$ of the energy distribution needs to be assumed. The most common shape used is a power-law (PL) function ($\Lambda(E) \propto E^{-\Gamma}$ where the photon index $\Gamma \sim 2-3$ for many sources). However, this simple shape is sometimes not enough to take into account specific features; derived shapes are then used: PL with exponential cut-off, curved or broken PL [11].

The data is split into bins in reconstructed energy $\mathrm{E_{rec}}$, zenith angle δ, off-axis ψ and optical efficiency ϵ. In each energy bin [$\mathrm{E_{rec\ ,i}}$,$\mathrm{E_{rec\ ,i+1}}$], the expected number of signal events s (gammas) is obtained by integrating the assumed spectral shape $\Lambda(E_{true})$ over reconstructed energies. As the resolution is not perfect, and also in order to take into account the acceptance of the instrument, a second integral over the true energy is needed:

$$s = \int_{E_{rec}=E_{rec,i}}^{E_{rec,i+1}} \int_{E_{true}=0}^{\infty} D(E_{rec}, E_{true}|\delta,\psi,\epsilon) A_{\mathrm{eff}}(E_{true}|\delta,\psi,\epsilon) \Lambda(E_{true}) dE_{true} dE_{rec}. \tag{3.4}$$

The effective area of the detector $A_{\mathrm{eff}}(E_{true}|\delta,\psi,\epsilon)$, *aka* the acceptance, and the energy resolution of the detector $D(E_{rec}, E_{true}|\delta,\psi,\epsilon)$, functions of the true energy E_{true}, are calculated from Monte Carlo simulations, and stored in tables.

For each bin, the probability of observing $\mathrm{n_{ON}}$ and $\mathrm{n_{OFF}}$ events is then given by the product of two Poisson distributions:

$$P(n_{\mathrm{ON}}, n_{\mathrm{OFF}}|s,b) = \mathrm{Pois}(n_{\mathrm{ON}}|s+b) \cdot \mathrm{Pois}\left(n_{\mathrm{OFF}}|\frac{b}{\alpha}\right) \cdot \tag{3.5}$$

The best estimate of b is obtained by maximizing the likelihood $L = P(n_{\mathrm{ON}}, n_{\mathrm{OFF}}|s,b)$.

For each energy bin, the residuals are calculated to check that the fit gives a relevant result.

3.5.5 Lightcurves

The light curve, *i.e.* the evolution of the flux over time, can be obtained by a similar approach as the spectrum determination, using a log-likelihood maximization procedure.

However for the LIV studies presented in the dedicated chapters, we used a simpler method which consists in calculating the excess in binned time intervals:

$$s = n_{ON} - \alpha n_{OFF}.$$

The events were weighted to take into account the effective area (which varies with the conditions of observation: true energy, zenith angle, off-axis and optical efficiency).

11. Note that very different shapes can be used for particular analyses, such as annihilation lines or continuous spectra for the indirect search for dark matter.

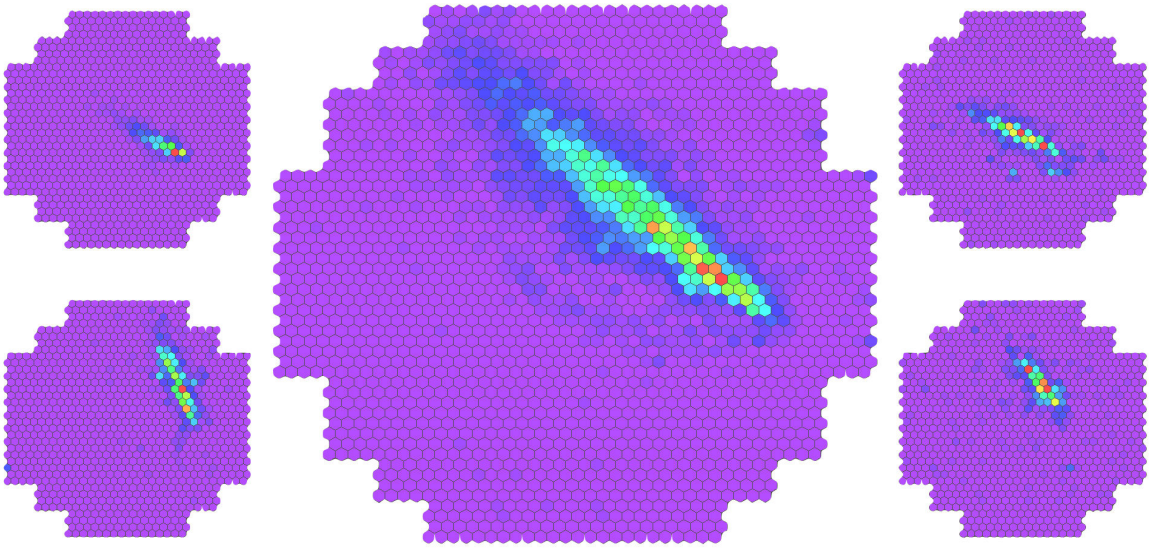

Figure 3.14: One of the first events detected in July 2012 by the full H.E.S.S. array including CT5, in the center. From [59].

Chapter 4

Study of the calibrated charge

Contents

With the new 28m telescope CT5, a new energy domain is opening, down to 20 GeV. While the spectral reconstruction with the four telescopes CT1–4 is now mastered, it is much more difficult to obtain energy spectrum with CT5: systematic uncertainties still need to be understood. In Mono mode, when only CT5 is triggering, the data are overwhelmed by the background, composed mainly of images of muons. In Hybrid mode, the low energies are still dominated by the data in CT5, but the reconstruction energy is backed by the strength of the four telescopes CT1–4. In this case, the background is better discriminated. Filtering runs using robust quality criteria is essential for a good reconstruction of the energy of incident particles.

Throughout this chapter, the term “intensity” will refer to the calibrated charge in photoelectrons, as opposed to the simple non-calibrated “charge” in ADC counts.

4.1 Context and aims of the calibrated charge studies

H.E.S.S. fifth telescope is in operation since July 2012. During a first phase of commissioning, calibration sources – Sgr A*, PKS 2155–304, PG 1553+113, the Crab nebulae – were observed to understand the new instrument. Physics runs started to be taken in 2013.

Several criteria (see 3.4) exist for the first phase of H.E.S.S. with 4 telescopes to assess the quality of the data and have been adapted for the full 5-telescope array. Additionally, we would like to get an idea of the quality of the calibration on its whole, including pedestal variations, high and low gain, flatfield and broken pixels. The study of the calibrated charge can provide such global information. A procedure has been establish to:

— show coarse discrepancies occurring during the calibration process;

— characterize major differences between CT5 and CT1–4;

— check if the response is source-dependent;

— monitor the status and the quality of the calibration over time.

In the following sections, the performed studies will focus on CT5. However, the procedure was also applied to CT1-4 measurements to get similar quality criteria.

4.2 Intensity distribution

As explained in previous chapter, the calibrate charge in the high gain channel I^{HG} of an event is obtained from the ADC count in this channel ADC^{HG}, in which the pedestal P^{HG} was subtracted; the pedestal-subtracted ADC count is then divided by the gain $\gamma_e^{ADC,HG}$ and multiplied by a flatfield coefficient FF specific to the considered pixel:

$$I^{HG} = \frac{ADC^{HG} - P^{HG}}{\gamma_e^{ADC,HG}} \times FF.$$

For the low gain channel, the process is similar, with the gain calculated from the high gain and the ratio HG/LG ("HiLo"):

$$I^{LG} = \frac{ADC^{LG} - P^{LG}}{\gamma_e^{ADC,HG}} \times (HG/LG) \times FF.$$

The calibrated charge is used during the reconstruction: it is read or displayed per event, then processed in order to get one image on the whole camera per event. The idea here is to get individual intensities per event, per pixel, and then stack all the event intensities per pixel.

4.2.1 Intensity histograms for an individual pixel

The intensity is already calculated by the official French analysis software, `ParisAnalysis`. We built a mechanism to stack all events seen by a pixel, for a given run. The output is one `.root` file per run, which contains 1 histogram per pixel (960 for CT1–CT4, 2048 for CT5); such distribution is shown in Fig. 4.1 for one CT5 pixel.

Part of the events shows a negative intensity, but the mean of the distribution of the intensities over a run is positive. There is a peak at -1: this value is a flag from `ParisReco::IntensityMaker` [1] when a calibration coefficient is missing, *i.e.* when a pedestal value, a gain coefficient, the HiLo or the flatfield coefficient is not known, or when the pixel is deactivated (flagged as "Broken" [2]).

1. part of the calibration code which combine all the separate calibration information (*e.g.* coefficients) to calculate the calibrated charge from the raw charge, event by event.
2. NB: the flag "Broken" for a pixel can change during the run

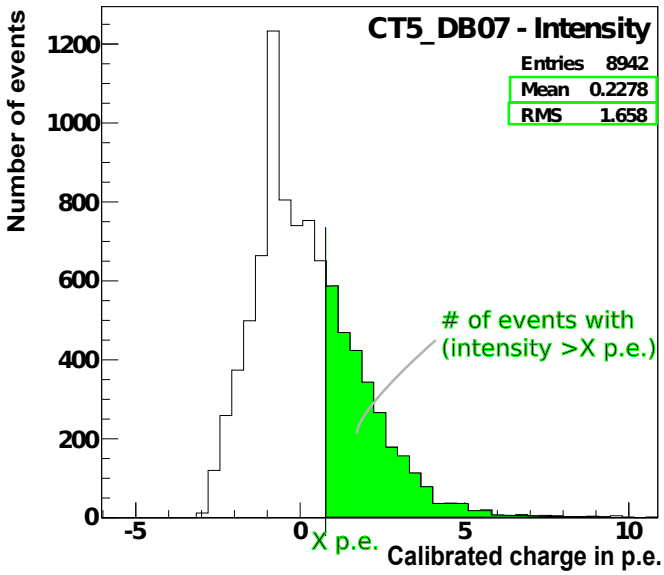

Figure 4.1: Distribution of the intensities for the pixel CT5_DB07 over a run of SgrA*. The mean of the distribution of the events over a run is positive; the negative values are within the resolution of the PMT. There is a peak at -1: this value is a flag from `ParisReco::IntensityMaker` when a calibration coefficient is missing, *ie.* when the HiLo, the FlatField, the gain or the pedestal value is not known, or when the pixel is deactivated during the whole run.
The parameters extracted from the distribution of the calibrated charge of a pixel are shown in green: mean and RMS of this per-pixel distribution, total number of events recorded by this pixel during the run, number or fraction of events over a threshold (e.g. > 3 photo-electrons).

This basic output per pixel and per run has been studied in order to assess the quality of a run, calibration-wise. It has also been used to identify faulty pixels.

4.2.2 Parameters derived from the intensity histograms for one pixel

As shown in Fig. 4.1, several parameters can be extracted from each pixel histogram:

— Mean and RMS of per-pixel distributions;

— total number of events;

— number or fraction of events over a threshold (e.g. $> X$ photoelectrons).

The distribution of these values over the camera will be studied in the following section.

4.3 Preliminary study

4.3.1 Principle

A visual scan of the intensity displays and intensity histograms (projection over the whole camera) was performed for a set of runs. The camera displays of the means and RMS were examined for 66 runs of SgrA* from March to September 2013 (set called **SGRA_2013_66**).

The visual scan gives us a first clue of what a well calibrated run or a poorly calibrated run look like, *a priori*. Fig. 4.2 shows the displays and projections for a well calibrated run, which presents the following expected behaviour:

— **Homogeneous displays**: as the intensities are summed over a run, and shower images can show up in any part of the camera, randomly, the displays of the means and of the RMS are expected to be homogeneous;

— **Positive means, close to zero**: the photomultiplier can either detect signal (photons, converted into photo-electrons) or pedestal signal (converted to 0 p.e.): for a perfect calibration, all means should be positive. Also the NSB is non negligible compared to the actual signal: as a consequence, means should not be too far from 0 p.e. (pedestal subtraction).

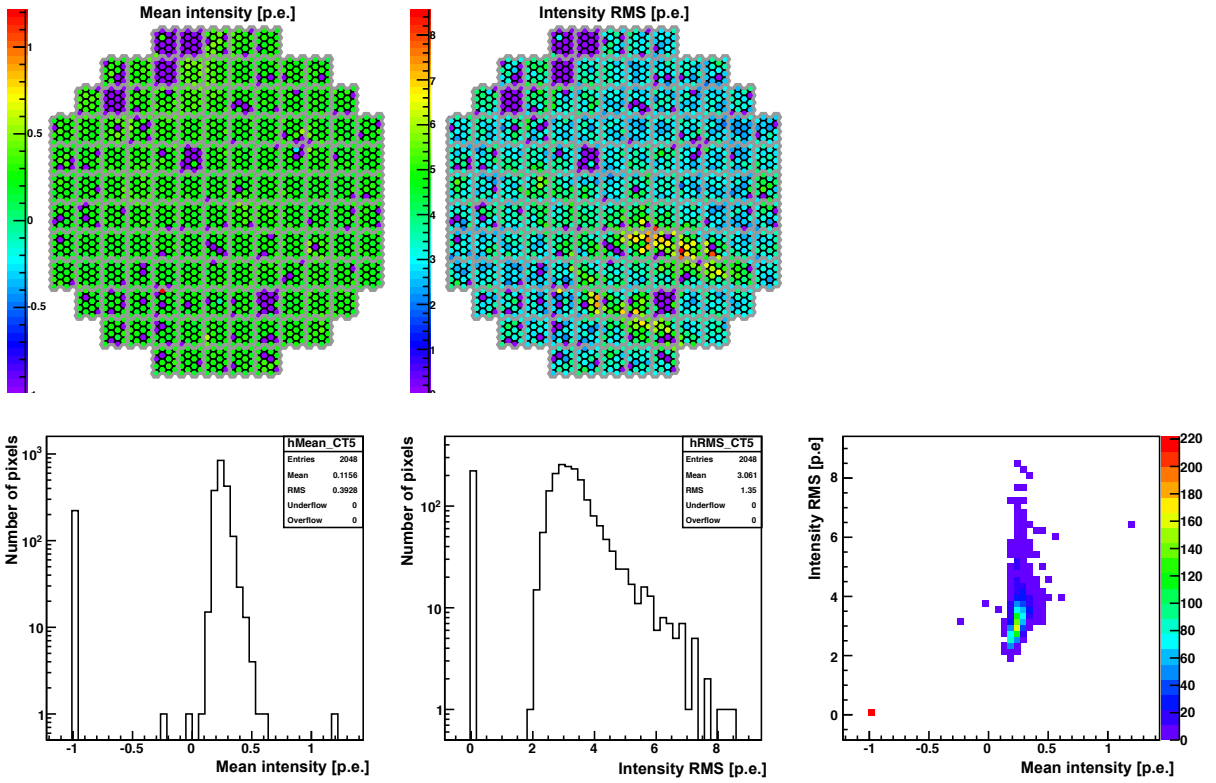

Figure 4.2: **An *a priori* well calibrated run**: camera displays (top) and projections (bottom) of the means (left) and RMS (middle) of the per-pixel distribution of the intensity in p.e. for run 83091. Note that the values of the mean and RMS are relatively small, around 0 p.e. of the means and between 2 and 7 for the RMS values. The scatter plot on the right shows the means *vs.* the values of the RMS (1 point/count = 1 pixel): there is no obvious correlation between the two variables.

— **Modest RMS values**: here they are between 2 and 7 p.e. Large RMS values, *e.g.* above a few tens of photo-electrons, would indicate a problem in the calibration.

The projections provide additional information – and criteria:

— **Means and RMS not correlated**: this is indeed the case for this run.

— **Few "Dead pixels"**: generally, pixels with a problem, characterized in these histograms by a RMS value equal to zero; discussed more later in this chapter. For this run, there are about 200 such pixels, *i.e.* about 10 % of the total camera pixels. Most of them also have a mean intensity equal to -1, which is a flag from `ParisReco::IntensityMaker` when a calibration coefficient is missing, indicating a faulty calibration. This might be a hardware problem – which would be surprising as CT5 is very recent – or a problem in the calibration software – some of it not being fully adapted yet to the new camera.

4.3.2 Found issues and debugging

Several faulty cases were detected during this preliminary procedure.

Large and correlated values of the mean and RMS

Fig. 4.3a shows the displays and projections for run 84571. Both displays look homogeneous; however a few pixels have large Means and RMS. The 2D projection histogram shows that large means are correlated with large RMS. This is a possible indication of a problem occurring during the calibration. Debugging followed two steps: we first looked at single pixel distributions, then checked individual events.

Looking at the distributions of individual faulty pixels, we found that the large mean and RMS value came from one single event with a huge absolute reconstructed intensity ($\sim \pm 10^6$ p.e. !), leading to the observed behaviour in the defective pixels: large and correlated means and standard deviations.

Looking at the detailed characteristics of this event, it appeared that it had a wrong associated time stamp t_{event} (event file), dated back to year 1970, significantly different from the pedestal time stamp (in pedestal file): year 2013. Since a correction proportional to the difference $t_{\text{event}} - t_{\text{pedestal}}$ is applied on the pedestal calculation, the large differences in the two time stamps led to absurdly huge values of the corrected pedestal.

We fixed this issue by hand-removing this event. New displays and projections are given in Fig. 4.3b: most of the mean intensities lie now between 0 and 1 p.e., while most of the standard deviations are between 1 and 10 p.e. A non negligible amount of pixels have a mean intensity of -1 coupled with a zero standard deviation: this flag corresponds to missing calibration coefficients or to a deactivated pixel. These pixels are further refered as "Dead pixels".

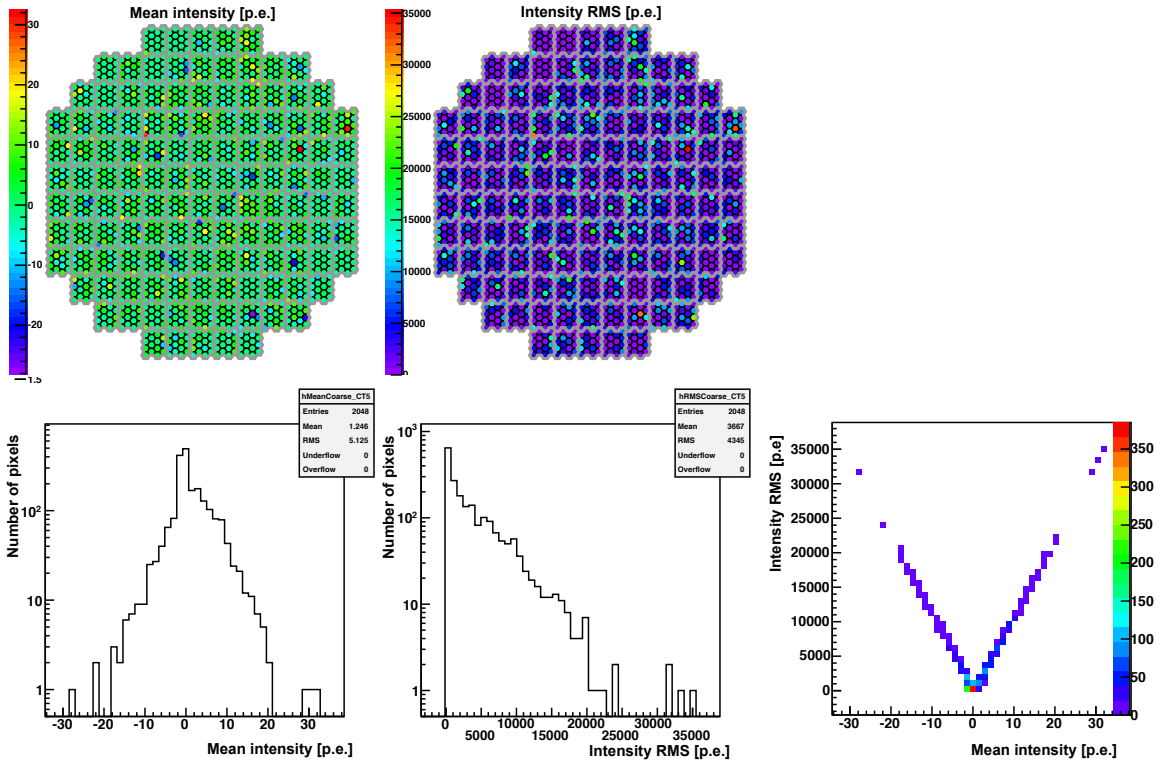

(a) Initial displays and projections. A few individual pixels have large mean and RMS values. The 2D projection histogram (left) shows that large means are correlated with large RMS.

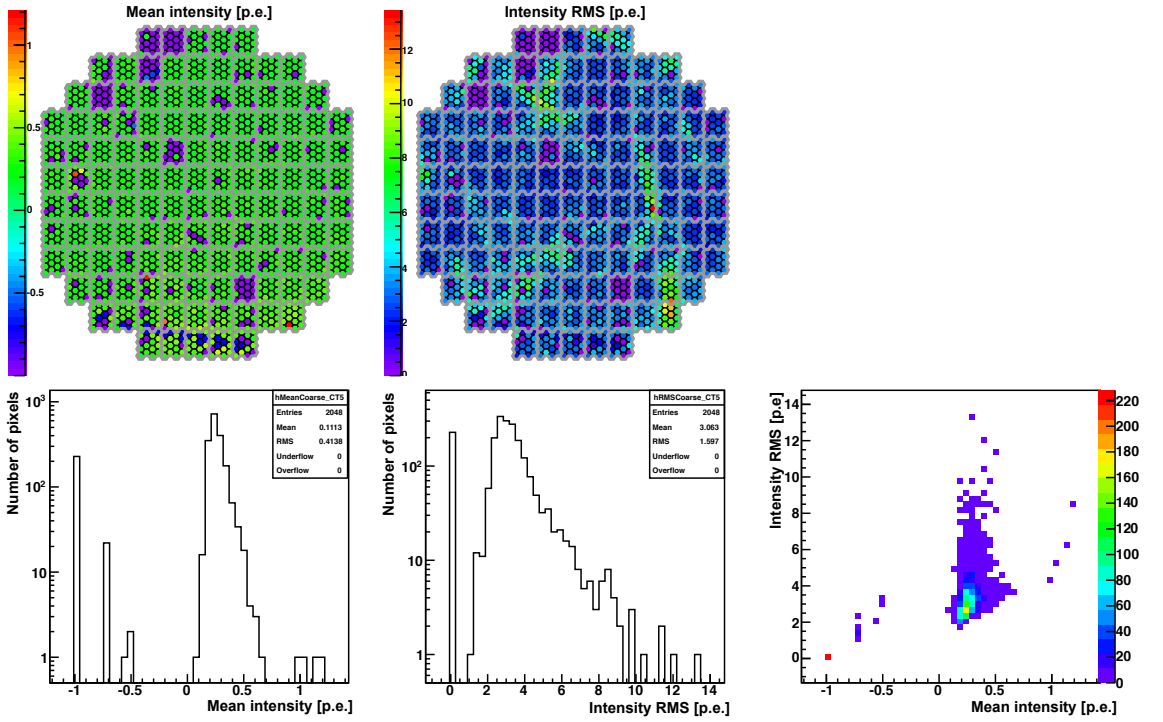

(b) After hand-removing the messing event

Figure 4.3: **Large and correlated values of the mean and RMS**: Intensity displays and projections for the run 84571, before and after a first debugging.

Large number of "Dead pixels"

Figure 4.4a (in appendix) shows the displays and the mean *vs.* RMS scatter plot for run 85237. The projections show a large number of Dead pixels (RMS = 0) originating from a problem in the calibration (missing coefficient or pixel deactivated during the whole run). They are mostly grouped in drawers. The 2D projection histogram (left) shows a continuum of mean and RMS values between -1 and 0 p.e. (means) and 0 to 2 p.e. (RMS).

We first checked `ParisReco::IntensityMaker`. It appeared that a hard cut on the High voltage was set at 10 volts, originally for CT1–4. Events with a higher HV values were ignored. We loosened the cut to HV < 100 volts. Figure 4.4b shows the new displays after the release of the HV cut. The number of Dead Pixels has decreased by about a factor 3 (~ 600 to ~ 200 Dead pixels). Note that this is only a temporary fix: the cut on HV should be tuned in a more proper way for CT5, for instance by setting a cut value proportional to the pedestal value.

To understand the origin of the remaining Dead pixels, we looked into the output of `ParisReco::IntensityMaker`. The following table gives the missing information for one event:

Ped not known	44 - 47
HiLo not known	2
High gain not known	5
FlatField not known	**210**
BrokenPixel	1
Total non valid	239

Crosschecking with the database entries, it was found out that there was no flatfield coefficient for the incriminated drawers. A problem has occurred during their calculation and had not been reported earlier to this study. Following our report, the flatfield code was checked and the coefficients, reprocessed. The number of missing flatfield coefficients went down to 107.

Bus patterns

The displays of the means and RMS in Figure 4.5 displays of the means, RMS and number of events for run 86258. The display of the means, and more strikingly the display of the number of events saved during the run per pixel, show patterns that follow two specific buses of the camera.

The projected distributions of the mean and RMS values are really similar to the ones shown in Fig. 4.2: they can not probe these patterns. On the contrary, the distribution of the number of events per pixels may help uncovering such behaviour. For the moment, following to the visual scan, the affected runs are discarded from the data quality run selection. Further studies have shown that these "bus" structures originate from a hardware issue (connectivity problem of the camera).

4.3.3 Summary of the found issues

The scanning of the displays enabled us to identify issues that may be present at the end of calibration:

— large mean values;

— large RMS values;

— correlation between mean and RMS values;

— dead pixels: missing calibration information or pixel deactivated *during the whole run*;

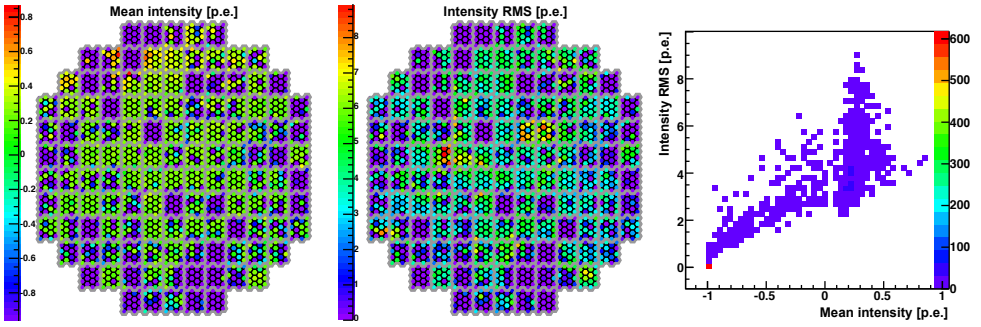

(a) Initial displays and projections. The displays show a large number of Dead pixels (RMS = 0), grouped in drawers. Note the continuous values of mean/RMS in the projection histogram.

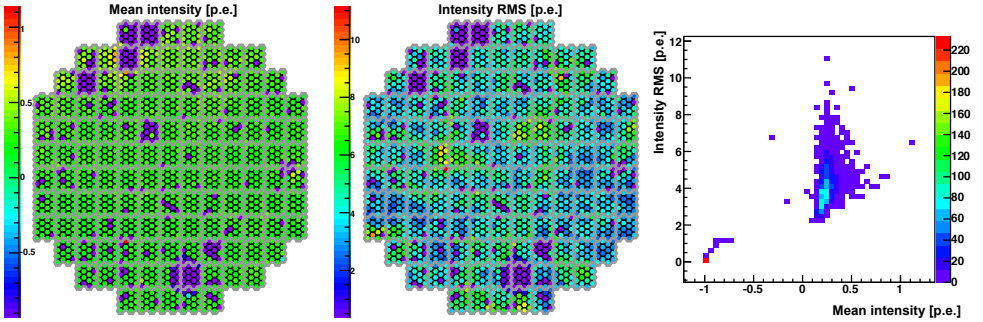

(b) After changing the maximum cut value on the High Voltage

Figure 4.4: **Large number of dead pixels**: intensity displays and 2D-projection for the run 85237.

— different mean, RMS values or different number of events between pixels, bringing up patterns in the displays;

Some of these issues were solved during this preliminary study: removal of badly time-stamped events, change in the HV cut, check of the flatfielding code and recalculation of the coefficients. The next step is to get automated procedure to spot these issues in a given run.

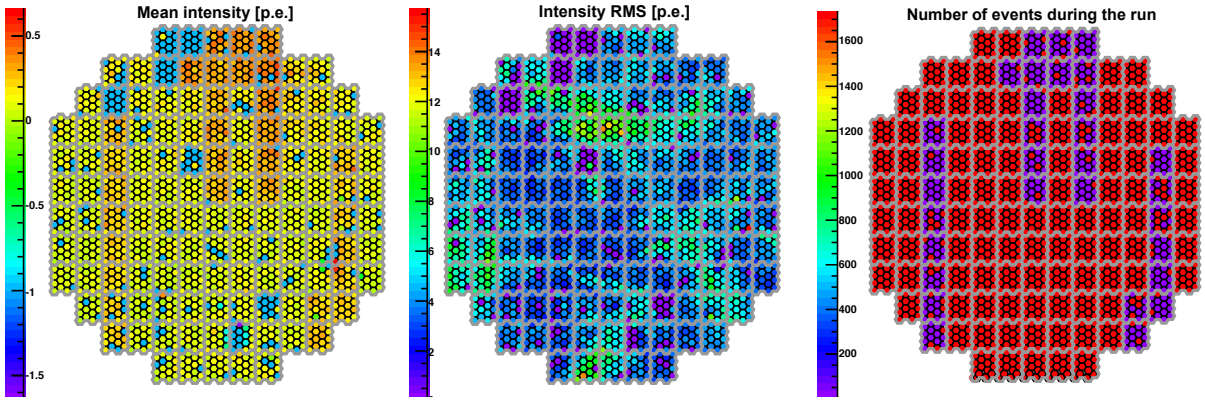

Figure 4.5: **Bus patterns**: Displays of the means (left), RMS (center) and number of events per pixel (right) of the per-pixel distribution of the calibrated charge for the run 86258. They reveal patterns following the buses of the camera.

4.4 Distributions per camera: stacking all runs, all pixels

The previous dataset was composed of 66 runs of SgrA*. As we would like to get criteria that do not depend on a particular source, we used a new set of runs. Moreover, following the preliminary studies, changes/fixes have been performed in the calibration chain – flatfield coefficient reprocessed, cuts on HV changed, events with bad time stamp removed – so we needed to reprocess the raw data anyway. We also need more statistics to get evolution over time/period and distributions over runs. For this and the subsequent sections, we used a selection of 517 runs taken between April 2013 and January 2014, with a duration of more than 1600 seconds, with CT5 participating.

In order to identify relevant parameters, the following distribution were scrutinized:

— Distribution of the means: distributions obtained by stacking the means of all pixels

— Distribution of the standard deviations: distributions obtained by stacking the standard deviations of all pixels

— Distribution of the total charge per pixel

— Distribution of the number of events

— Distribution of the number of events over 100 p.e.

— Distribution of the number of events over Mean + 100 RMS

Figure 4.6 shows the distributions of the mean intensities per telescope, stacked for all pixels in all runs. The distributions zoomed around the main peak, on a log scale: the central parts of the distributions follow a Gaussian function (fit in red); yet the tails reveal secondary populations. Indeed, by mixing all the runs and all the pixels, we get a mixture of all possible states of pixels: a bright star entering the field of view (before getting deactivated), NSB, particular sources... and possibly artifacts arising from a (still) preliminary calibration.

It is noteworthy that, for CT1–4, the mean intensities lie between -2 and 6 p.e., whereas for CT5, the distribution extends outside this range. This feature seen in CT5 is problematic as in the Hillas analysis, a cleaning is applied on the calibrated charge: any pixel for which the intensity is greater than 7 p.e. is kept for reconstruction. We do not expect any more events with absurdly huge intensity, that could drag the mean intensity to high (> 7 p.e.) values. So, there must be a fair amount of events with high intensities, for this pixel and this run. A cut ("cut 1") could be set on the to remove the pixels which have to large mean intensities, for instance at the cleaning threshold (7 p.e.).

Additional distributions were studied:

— The distribution of the intensities' RMS per telescope, stacked for all pixels in all runs from the set **ALL_517**: they reveal two different populations. However, there is no reason to reject either population.

— The distributions of the intensities' charge integrated over a run and the number of events: they showed no discrepancy.

— The distributions of the number of events over 100 p.e., shown in Figure 4.7 for the five telescopes: they show two populations. For each telescope, most of the distribution follows a Gaussian function (fit in red). A secondary population can be seen at low number of events for all telescopes: it might correspond to pixels with a high charge due to a star in the field of view. For CT5, there is a tail, which could point toward faulty pixels. A "safety" cut ("cut 2") rejecting pixels/runs with two many events over 100 p.e. could be set (> 600 events with more than 100 p.e. for instance). However no further study has been performed yet on these events.

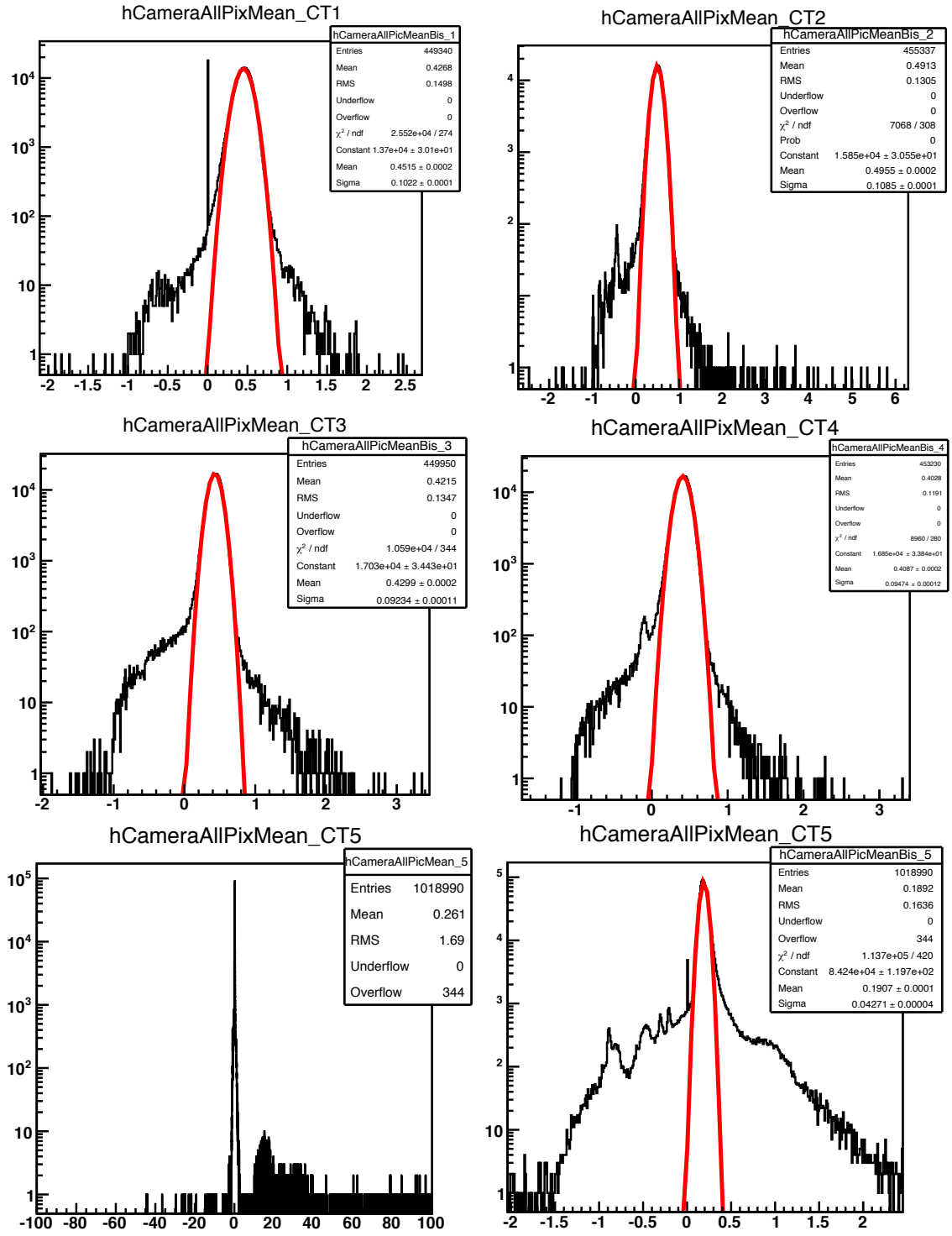

Figure 4.6: Distribution of the mean intensities per telescope in p.e., stacked for all pixels in all runs from the set **ALL_517**. While for telescopes CT1 to CT4, the means range between –1 and 2 p.e., CT5 means extend far outside this range (unzoomed distribution, left). The central parts of the distributions follow a Gaussian function (fit in red); yet the tails reveal secondary populations.

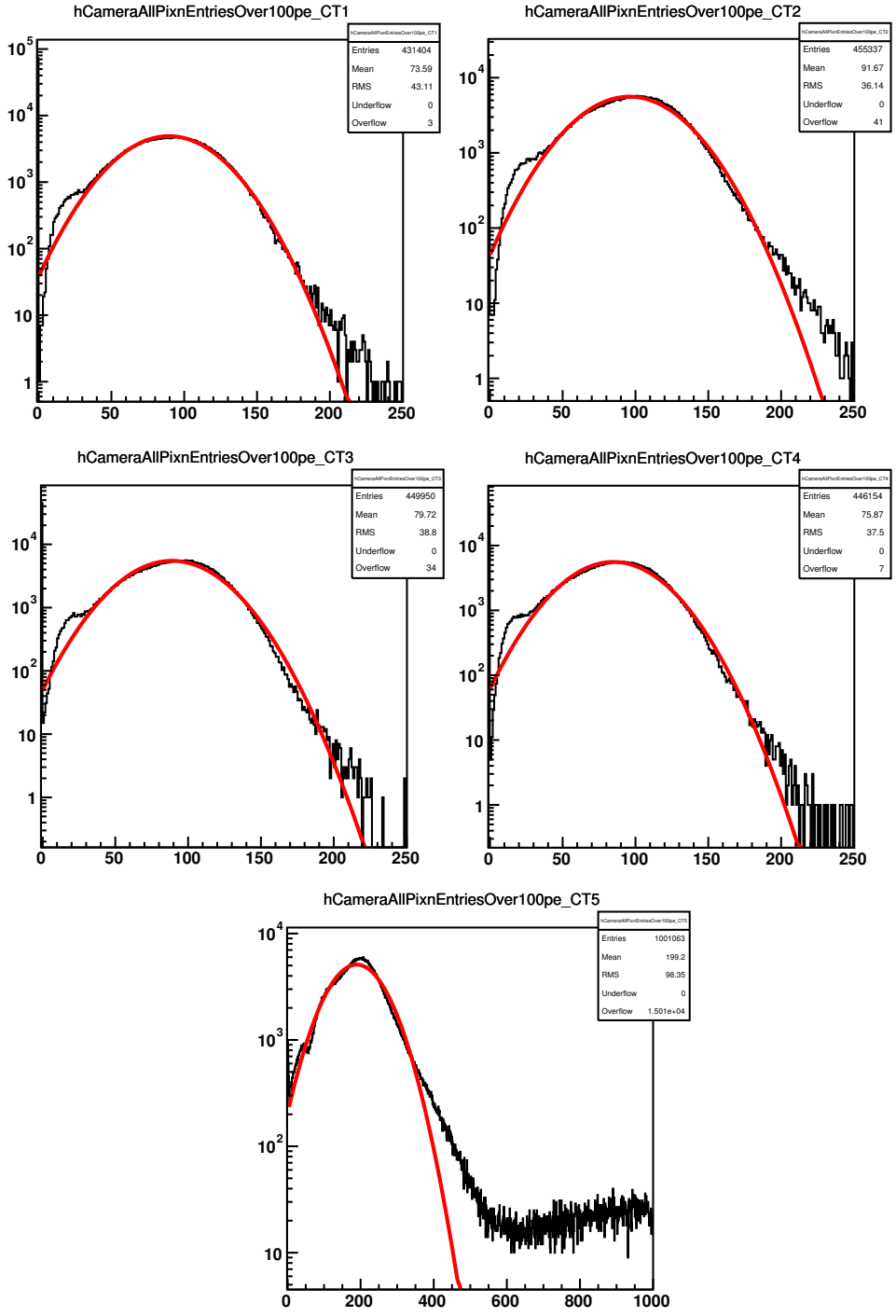

Figure 4.7: Distribution of the number of events over 100 p.e., stacked for all pixels in all runs from the set **ALL_517**. For each telescope, most of the distribution follows a Gaussian function (fit in red). A secondary population can be seen at low number of events for all telescopes: it might correspond to pixels with a high charge due to a star in the field of view. For CT5, there is a tail, which could stand for faulty pixels.

4.4.1 Parameters derived from the projections over the whole camera

Following the preliminary study and looking at the stacked distributions, we proposed these variables on the whole camera for each run to detect each possible issue:

— number of Dead pixels, *i.e.* pixels for which the standard deviation is zero: the distribution of the intensities is a peak at –10 (no intensity histogram), at –1 (problem during the calibration) or at 0 (unknown problem).

— mean over the camera of the per-pixel means

— mean over the camera of the per-pixel RMS

— number of pixels with means over 7 p.e.

We performed tests to choose, among the different proposed cut variables, the one which would enable a discrimination between "good", "doubtful" and "bad" runs. We then proposed a cut on the chosen variable.

To evaluate the discriminating power of each of the proposed parameters, we checked the two following criteria:

1. The distribution of the parameter over all the runs could show two (or more) visible populations, and should allow a cut to be set, so as to identify "good", "doubtful" and "bad" runs.
2. It should show an evolution over time;

A summary of the tests on each variable is given in table 4.1.

	Test 1: 2 populations or dubious tail	Test 2: evolution with time?
1) # dead pixels	**yes**	**yes**
2) mean(mean)	**yes**	-
3) mean(RMS)	no	-
4) # pixels with means > 7 p.e.	**yes**	-

Table 4.1: Summary of the tests on each proposed discrimination variable.

The remaining criterion is the number of Dead Pixels. The evolution over period is given Fig. 4.8. This number is stable for most of the runs; however a couple of runs in periods 2013-05, 2013-06 and 2013-10 show a larger amounts of such pixels. The nice evolution over time allows the monitoring of the differences between the runs.

4.4.2 Quality flags

The proposed cuts on the number of Dead pixels (DP) are the following:

— **Good** if DP $< 5\%$

— **Doubtful** if $5\% <$ DP $< 10\%$

— **Bad** if DP $> 10\%$

With these cut values, the DP flags for the 517 studied runs are distributed as follows:

— 18 were flagged as "bad"

— 30 were flagged as "doubtful"

— 429 were flagged as "good"

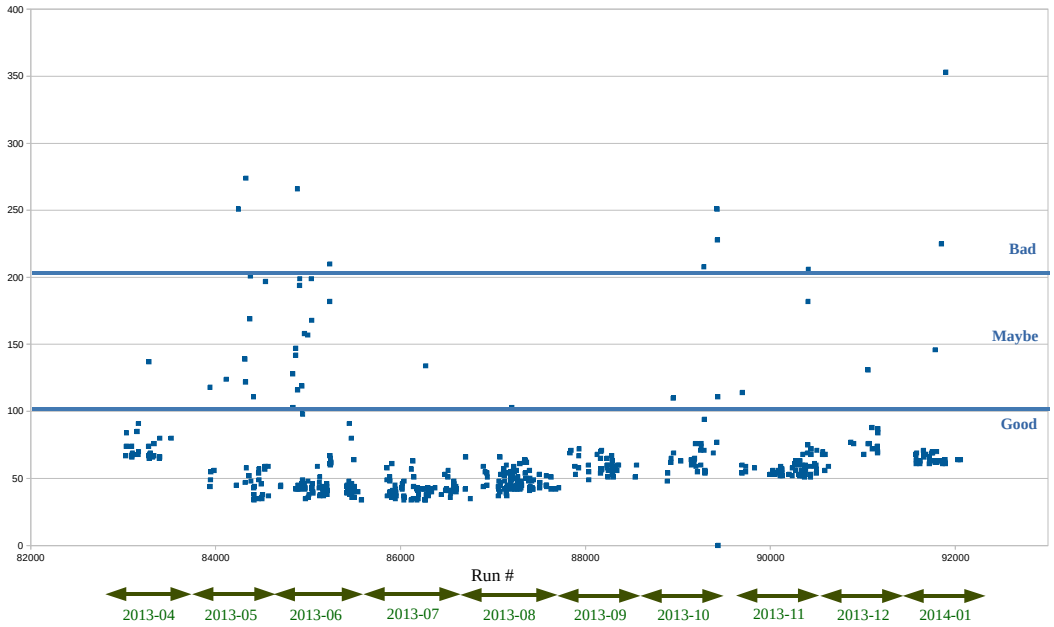

Figure 4.8: Evolution of the number of dead pixels per run. This number is stable for most of the runs; however a couple of runs in periods 2013-05, 2013-06 and 2013-10 show a larger amounts of such pixels.

4.4.3 Database entries

We proposed to store the following in the database, per run:

— per pixel: mean and RMS. This corresponds to 960×2 values for each telescope CT1–4 and 2048×2 values for CT5);

— per camera: flag, number of dead pixels, means per camera, RMS of the number of events per pixel, *i.e.* 3 values for each telescope.

Additionally, variables providing information on the reason of the rejection of the run are:

— RMS of the entries > 0: indicates a bus problem;

— RMS of the means $= 0$ and Mean $= -1$: indicates a problem in calculating the intensities: pixel flagged as broken during the whole run;

— RMS of the means $= 0$ and Mean $= 0$: no histogram. Possibly no charge in ADC stored $\rightarrow$ drawer problem;

— mean of mean > 7 p.e. and/or there are pixels for which number of means > 7 p.e. : hot pixel, calibrated charge overestimated: will cause the reconstruction algorithm to detect a shower event in this part of the camera. [3]

3. These hot pixels are actually taken care of in Model++: additional cuts are defined to remove them during the analysis.

4.5 Physics case: SgrA* energy distribution

We would like to test the impact of the quality criteria on the spectral energy reconstruction. A set of 60 runs of SgrA* taken with CT5 have been considered. The number of Dead pixels has been retrieved for each of the runs. This allowed to sort the set from the quality of the runs, using the combined criteria. Among the 60 runs:

— 3 were flagged as "bad"

— 4 were flagged as "doubtful"

— 53 were flagged as "good"

There is not enough statistics with the 7 runs flagged as bad+doubtful to produce the spectral energy distribution. Thus, to illustrate the impact of the combined criteria, the set was split into two: one subset composed of the 30 runs with the best quality (lowest number of Dead Pixels) and one subset with the 30 runs with the lowest quality. The first subset has a mean number of Dead Pixels of 44 ($\sim 2.1\%$ of the pixels) while the second subset has a mean number of Dead Pixels of 138 ($\sim 6.7\%$ of the pixels). A reconstruction with Model++ Mono has been performed on each of the two subsets. Fig. 4.10 shows the spectral energy distribution for SgrA* using the two subsets of runs. The impact lies on the flux normalization at 1 TeV:

— $(2.8 \pm 0.4) \times 10^{-12} \mathrm{cm}^{-3}\mathrm{s}^{-1}\mathrm{TeV}^{-1}$ for the best quality runs,

— $(1.5 \pm 0.3) \times 10^{-12} \mathrm{cm}^{-3}\mathrm{s}^{-1}\mathrm{TeV}^{-1}$ for the lowest quality runs, about half the flux computed with the best quality subset of runs.

We cannot conclude from this comparison of the two spectra as is. A dedicated study of the systematic errors on the spectral reconstruction associated with the dead pixels is needed. For example we could take the same list of runs (from data or simulated runs), and manually "kill" a series of pixels (5%, 10%, 15%, etc.) to see the impact on the spectral reconstruction. The variation by a factor of 2 of the flux may come from other aspects: atmosphere, period of data taking, flare of the source, or zenith angle during observation.

4.6 Conclusion

Studying the evolution of the calibrated charge over time allowed to show coarse discrepancies occurring during a run: patterns in the camera, large means and RMS of the intensities. The proposed criterion (number of dead pixels) does not allow to detect all these issues, but gives a first idea of the quality of the calibration.

The study of the calibrated charge could be extended: some of the criteria could be studied further (large RMS, large means). The natural extension of this work is to build automatic debugging tools.

Integrating the intensity not over a run but over a whole period allows also the detection of faulty pixels, with calibration issues over whole periods; these pixels are highlighted in camera displays in Appendix A.2. Following up these studies would allow to check a possible period-dependence of these faulty pixels.

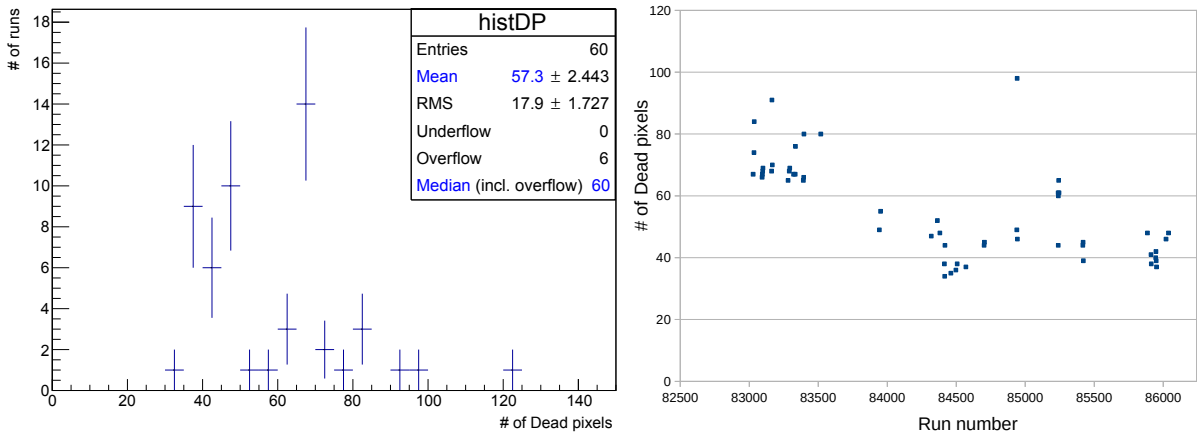

Figure 4.9: Distribution of the number of Dead pixels per run (left): two populations of runs can be seen (Median ~ 60). Number of Dead pixels as a function of the run number for the same runs: the ones with more than 60 Dead pixels are gathered in the first period (run number < 83800).

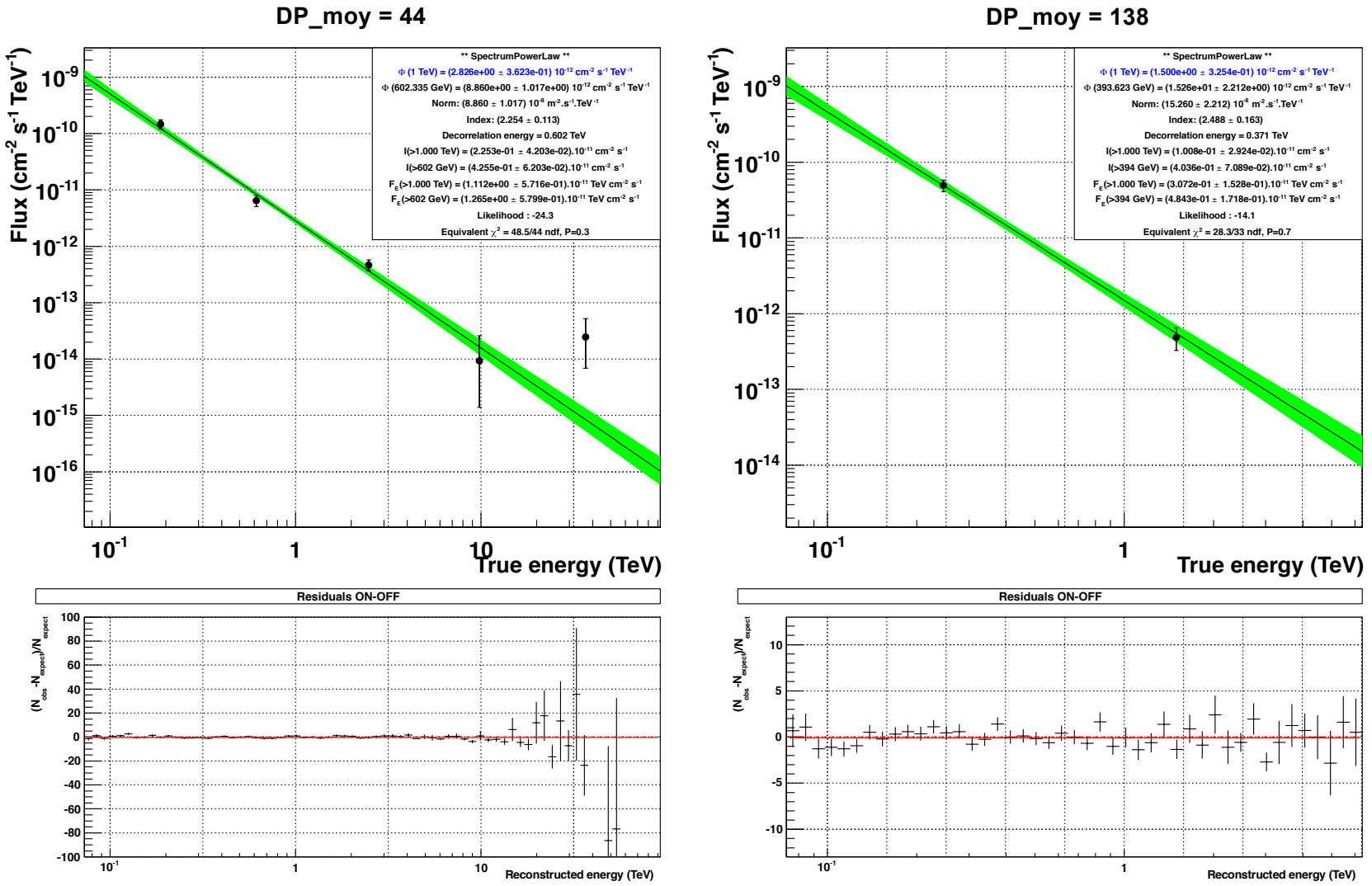

Figure 4.10: Spectral energy distribution for SgrA* using two subsets of runs taken with CT5, reconstructed with Model++ Mono. Left: 30 runs with the highest quality (lowest number of Dead Pixels). Right: 30 runs with the lowest quality. The impact lies on the flux normalization: there is a factor 2 between the two flux values.

Chapter 5

Fermi-LAT

Contents

5.1 Detecting gamma photons in space

While very high energy (VHE) photons, above a hundred GeV, require huge collecting areas ($\sim 10^4\,\mathrm{m}^2$) to be detected, high energy photons, from a few MeV to tens of GeV, can be observed by detectors with smaller areas. This is due to the fact the cosmic and gamma ray fluxes increase with decreasing energy.

It is then possible to conceive and launch detectors on board satellites, freeing the observations from the influence of the atmosphere. The pioneer gamma telescope was *Explorer 11* [60], launched in 1961; it was using scintillator detectors along with a Cherenkov counter. The following satellite instruments – SAS-B [61], COS-B [62], EGRET [63] – used the spark chambers technique: particles traveling through a gas volume trigger its ionization.

AGILE [64] introduced the use of tungsten plates and scintillators, combined with cesium iodide calorimeter. *Fermi* (formerly *GLAST*) uses the same principle with improved setup.

5.2 *Fermi*-LAT

Fermi space telescope was launched in June 2008. It is revolving round the Earth on a quasi circular orbit, at an altitude of 565 km. On board, two complementary instruments: the *Gamma-ray burst monitor* (GBM) and the *Large area telescope* (LAT). The GBM is dedicated to the early detection of gamma-ray bursts at low energy (8 keV to 40 MeV). It is composed of 12 Sodium iodide detectors (8 keV to 1 MeV) and two scintillators (200 keV to 40 MeV). With a field of view of 8 sr, it observes two thirds of the sky at any time with an accuracy of 0.17° (part of the sky not hidden by the Earth). Its coverage of the sky makes it a powerful tool to study

GRBs, especially when combined with the LAT, to which it sends a trigger for each detection of a burst.

5.2.1 Structure

The LAT [65] is a pair-conversion detector. It measures the direction, energy and time of arrival of gamma photons from 20 MeV to 300 GeV. It has a wide field of view (2.4 sr at 1 GeV), allowing the observation of the full sky in 3 hours, *i.e.* within two orbits. It composed of:

— a **tracker**, totaling 16 separate towers, alternating tungsten (photon converter) and silicon plates. Thanks to a high atomic number, the 16 tungsten plates facilitates the conversion of a photon into a pair e^-/e^+. With one *Silicon strip detector* (SSD), it is possible to measure the coordinates of a charged particle in 1 direction; using two consecutive orthogonal SSDs allows to get the coordinates in two dimensions. Eventually, the succession of 18 SSDs allows to reconstruct the full track of a charged particles, in 3D. The thickness of the tungsten plates are thiner at the beginning of the track ("FRONT") to get a good angular resolution, and thicker for the last four plates ("BACK"), so as to force the conversion of the remaining photons, right before entering the calorimeter.

— an **imaging calorimeter**, also split in 16 parts positioned under each tracker tower. Each part is composed of 8 layers of 12 bars of cesium iodide, alternated orthogonally. The charged particles ionize the atoms of the calorimeter: the light emitted when the atoms de-excite is collected by two photo-diodes on each side of the bar. Thus the calorimeter, besides precisely measuring the energy of an incoming charged particle, enables the reconstruction of its direction.

— a **anti-coincidence system**, composed of scintillator plates; they are covering (almost) all the surface of the satellite. It vetoes the charged events entering the detector.

Additionally, the satellite is shielded to protect it from the micro meteorites. This structure of the *Fermi* telescope is depicted on Figure 5.1.

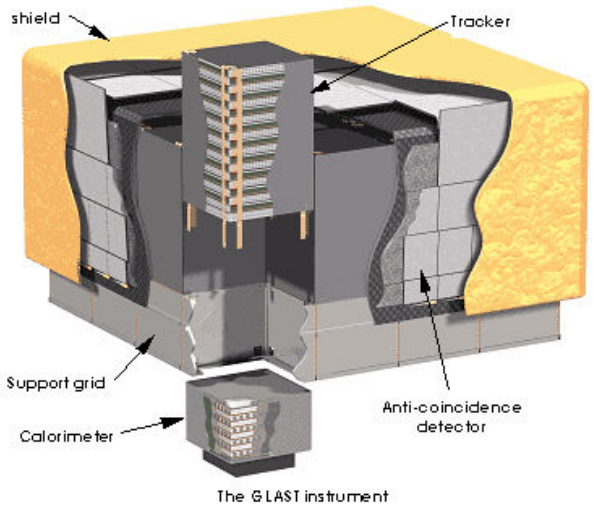

Figure 5.1: Structure of the *Fermi* telescope, revealing the 16 towers forming the tracker and the calorimeter; one such tower is separated from the rest, to better show the inner layers of the tracker and the calorimeter.

5.2.2 Observations

The observation time is split between survey mode and pointing on specific sources:

— during the **survey** mode, the aim is to observe the sky uniformly. This mode corresponds to $\sim 70-80\,\%$ of the observation time.

— **pointed observations** are aimed at getting more statistics for a particular source, useful for instance to get fine lightcurves on short timescales. They can be scheduled, triggered by external instruments ("Target of Interest") or triggered internally (*e.g.* GBM trigger when detecting a GRB).

Advantages and limitations of the two modes are discussed in [66].

5.3 Reconstruction and analysis with *Fermi*-LAT

5.3.1 Identification of the events and background removal

Raw data is processed by reconstruction algorithms to get the direction and energies of the incoming particles, combining the signal from the tracker, the calorimeter and the veto plates.

Both charged cosmic particles and gamma photons can trigger a measurement by the tracker and the calorimeter. The anti-coincidence plates detect charged particles entering the detector and can veto their participation in the data. This helps reducing the total amount of data by about a factor 10, from ~ 2 kHz to a few hundred Hz. A non-reducible source of background, however, is composed of neutral pions decaying just before entering the detector: in this case, the anti-coincidence do not identify the hadronic origin of the two product photons.

5.3.2 Available processed data

As these algorithms are regularly improved, different sets ("*Passes*") of processed data are available. Pass 6 and 7 were used for the analysis of the GRBs described in Chapter 8; the latter pass (7) has improved classification algorithms, leading to an increase in the effective area below 300 MeV. Recently, reprocessed sets have been released, Pass 8, with further improvement of the algorithms, leading to an increase in the effective area of the order of 10 % [67].

Different "*classes*" of events are used, corresponding to different cuts applied on the processed data. In particular, the analyses in this work where performed with Class "Transient", tuned for the search of transient objects with limited statistics such as GRBs: small angular cuts and short time intervals, with an overall background rate of a few Hz.

5.3.3 Performances

The following instrument response functions (IRFs) are presented shortly for Pass 7: effective area for different energies of a gamma, angular resolution and energy dispersion. They can be found will great details in Ref. [68].

Effective area

Effective area can be obtained from Monte Carlo (MC) simulations or from in-flight data, using bright point-like sources. The effective *Transient* class, compared with other classes in Figure 5.2, was obtained from MC; it shows a better effective area compared to class *Source*, by up to 20 %.

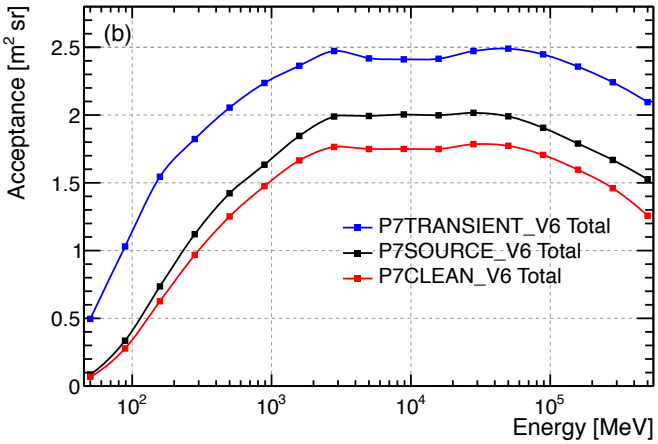

Figure 5.2: Effective area of the LAT as a function of energy for different classes. The *Transient* class shows a better effective area, by up to 20 %. From [68].

Angular resolution

The angular resolution of the LAT for class *Transient* is given in Figure 5.3 for different incidence angles. Only the angular resolution for the FRONT part of the tracker is shown: it has been indeed optimized for getting a better angular resolution (thinner tungsten layers).

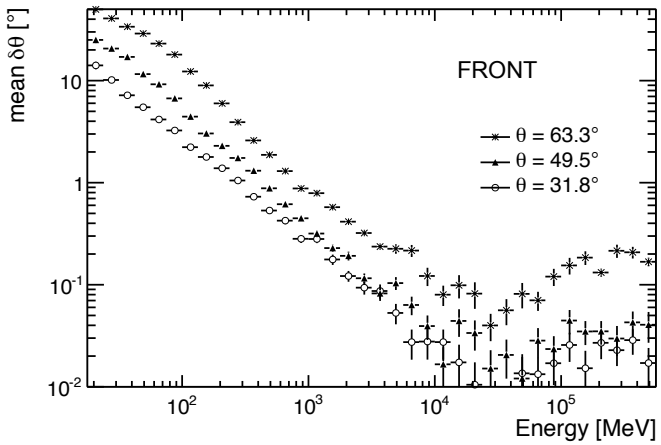

Figure 5.3: Angular resolution of the LAT for class *Transient* for different incidence angles. Only the – optimized – angular resolution from the FRONT part of the tracker is shown. From [68].

Energy dispersion

The energy dispersion for class *Source*[1] is presented in Figure 5.4: it is lower than 20 % for energies above 20 MeV. The best energy resolution is obtained in the range 1 GeV – 100 GeV; for higher energies, the loss in precision comes from a partial energy measurement (leakage).

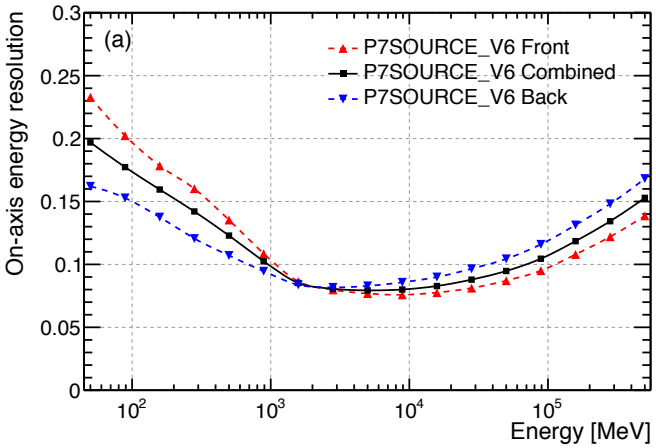

Figure 5.4: Energy dispersion for class *Source*: it is lower than 20 % for energies above 20 MeV. The best energy resolution is obtained in the range 1 GeV – 100 GeV. From [68].

1. Energy dispersion for class *Transient* was not publicly available, but is expected to be lower than 15% in the analysis range from 20 MeV to 30 GeV

Chapter 6

Probing the dispersion in the data with a maximum likelihood method

Contents

Introduction

The analysis of strongly varying fluxes of GRBs and AGNs during bursts and flares requires precise measurement methods with a good control of the systematics. Previous methods in use, such as cross-correlation functions and wavelet transforms, focused on a comparison of the light curves in two energy bands. For many years, these binned methods allowed to provide interesting results in the context of LIV analyses, whereas unbinned methods have been implemented more recently. The main advantage of the unbinned approach is that it makes the best use of the

information provided by time-delay measurements. Unbinned methods used in the search for LIV effects include maximum sharpness methods (Energy cost function [69], DisCan [70], SMM [71]) and the maximum likelihood method (ML). Likelihood maximization methods have been commonly used in high-energy physics as well as in many subfields for more than 30 years. They are particularly suited in case of low statistics such as dataset provided by astrophysical observations. A few aspects of these methods can be considered a weakness. As a principle, we need to know the model to be probed in the likelihood fit. Besides, in case of ON/OFF source observation, it is not possible to do a direct subtraction $ON - OFF$ to get the signal, and we need to model the background contribution. Also, ML methods are CPU time-consuming, compared to binned method.

The idea of using a ML maximization method for determining time lags is quite recent. Martinez and Errando [72] were among the first to introduce its formulation for measuring the dispersion parameter in the data of flaring astrophysical sources. The MAGIC collaboration [69] applied this method to a flare of Mkn 501 while the H.E.S.S. Collaboration [14] carried out a LIV analysis using ML with a flare of PKS 2155–304.

General procedure – notations

A set of events are reconstructed in the observation region ("ON" region); for each event with index i, we get the information of the arrival time t_i and its observed energy E_i. Selection cuts are applied and restrict the range of the analysis: for each event, time between $\mathrm{t_{min}}$ and $\mathrm{t_{max}}$, energy between $\mathrm{E_{min}}$ and $\mathrm{E_{max}}$.

A maximum likelihood method is used, to make the best use of the information contained in the data. A sharing energy $\mathrm{E_{cut}}$ is chosen so as to split the dataset into two sets with approximately the same statistics: the lowest-energy events (with $E < E_{\mathrm{cut}}$) are used to build a template lightcurve representing the injected LIV model, while the $\mathrm{n_{ON}}$ high energy events ($E > E_{\mathrm{cut}}$) are processed in the calculation of the likelihood.

6.1 Likelihood formula

For most studied flares, the background is negligible ($\mathrm{S/B} \gg 1$): the original formulation by Martinez and Errando applies well for these datasets. The formulas for the case where $\mathrm{S/B} \gg 1$ are recalled in section 6.1.1. However, in some cases, the background constitutes a significant part of the observed data ($\mathrm{S/B} \sim 1$): in this case, a specific procedure has been developed to take the background contribution into account: this is explained in section 6.1.2.

The aim here is to measure the dispersion parameter τ_n, defined in the previous chapter for LIV models: for two photons of arrival times t_1 and t_2 and energies E_1 and E_2 as the ratio of the difference of arrival times over the difference of their energies to the power n:

$$\tau_n \equiv \frac{\Delta t}{\Delta(E^n)} = \frac{t_2 - t_1}{(E_2^n - E_1^n)} \tag{6.1}$$

The definition of this parameter can be extended for more than two photons: in the case of the maximum likelihood method, it stands for the most probable common dispersion parameter experienced by a set of photons in a given energy range.

6.1.1 Case of negligible background

For a given dispersion parameter τ_n, for a set of n_{ON} events detected in the source ON region included in the fit range $[E_{cut};E_{max}]\times[t_{min};t_{max}]$, the unbinned likelihood function is:

$$\mathcal{L}(\{E_i,t_i\}_{i\in[1;n_{ON}]}|\tau_n)=\prod_{i=1}^{n_{ON}}P_{\rm Sig}(E_i,t_i|\tau_n) \tag{6.2}$$

The probability density function (PDF) associated with each gamma-like particle characterized by its time t_i and energy E_i is:

$$P_{\rm Sig}(E_i,t_i|\tau_n)=\frac{1}{N_{\rm Sig}(\tau_n)}\cdot R_{\rm Sig}(E_i,t_i|\tau_n) \tag{6.3}$$

where

$$R_{\rm Sig}(E,t|\tau_n)=\int_{E_{true}=0}^{\infty}D(E,E_{true})A_{\rm eff}(E_{true},t)\Lambda_{\rm Sig}(E_{true})F_{\rm Sig}(t-\tau_n\cdot E_{true}^n)dE_{true} \tag{6.4}$$

and $N_{\rm Sig}$ is a normalization factor.

$P_{\rm Sig}$ takes into account the emission (time distribution $F_{\rm Sig}$ and energy spectrum $\Lambda_{\rm Sig}$ at the source), the propagation (delay $\tau_n\cdot E_i^n$ due to possible LIV effect) and the detection of a photon by the detector (energy resolution D and effective area $A_{\rm eff}$). The template light curve $F_{\rm Sig}$ describes the emission of the photons at the source. It can be modeled within the framework of a specific theory or derived from a parameterization of the time distribution of the low energy photons in the dataset.

The normalization factor $N_{\rm Sig}$ of the PDF $P_{\rm Sig}$ is the integral of $R_{\rm Sig}$ where the likelihood function is defined, *i.e.* on the range $[E_{cut};E_{max}]\times[t_{min};t_{max}]$; for a given dispersion parameter τ_n,

$$N_{\rm Sig}(\tau_n)=\int_{t=t_{min}}^{t_{max}}\int_{E=E_{cut}}^{E_{max}}R_{\rm Sig}(E,t|\tau_n)dEdt \tag{6.5}$$

The best estimate $\widehat{\tau}_n$ of the dispersion parameter τ_n is obtained by maximizing the likelihood $\mathcal{L}(\{E_i,t_i\}_{i\in[1;n_{ON}]}|\tau_n)$.

6.1.1.1 Possible simplifying assumptions

Perfect energy resolution approximation

The effect of the energy resolution $D(E,E_{true})$ can be considered to be negligible if the precision on the energy measurement is excellent in the range $[E_{cut};E_{max}]$ [1]. In this case, the integration over energy in the expression of $P_{\rm Sig}(E_i,t_i|\tau_n)$ can be removed:

$$P_{\rm Sig}(E_i,t_i|\tau_n)=\frac{1}{N_{\rm Sig}(\tau_n)}\cdot A_{\rm eff}(E_i,t_i)\Lambda_{\rm Sig}(E_i)F_{\rm Sig}(t_i-\tau_n\cdot E_i^n) \tag{6.6}$$

The implication of this simplification on the results is studied in Section 6.2.2.2 of this chapter. This assumption was used for the measurement on *Fermi* GRBs and on PG 1553+113 (see next chapters).

1. The actual energy resolution is of the order of 10 % in this range, *i.e.* between $E_{\rm cut}$ = 300 GeV and a few TeV for H.E.S.S. and above 100 MeV for *Fermi*-LAT

Effective area

The effective area $A_{\rm eff}(E,t)$ can be averaged over the varying observing variables, leading to a simplified expression, where $A_{\rm eff}$ depends only on the energy:

$$A_{\rm eff}(E,t) = A_{\rm eff}(E). \tag{6.7}$$

For satellite telescopes, this assumption is applicable when the direction of the source in instrument coordinates do not vary much during the observation period considered in the analysis. For Cherenkov telescopes on ground, this can be assumed in the case when the observing conditions (e.g. atmosphere, zenith angle) do not change substantially during the night.

We will quantify the impact of theses assumptions with Monte Carlo simulations in the section 6.2.

6.1.2 Case of flares with important background contribution

The background comes from π^0 decays in proton showers, electrons or heavy elements misidentified as photons. In case of a poor signal-over-background ratio S/B, the background has then to be included as an additional term in the formulation of the probability density function (PDF): in the most general case, for a given number of signal and background events s and b in the observation region ("ON" region) and for a given dispersion parameter τ_n, the unbinned likelihood is:

$$L(n_{\rm ON}, n_{\rm OFF}|s,b,\tau_n) = {\rm Pois}(n_{\rm ON}|s+b)\cdot{\rm Pois}\left(n_{\rm OFF}|\frac{b}{\alpha}\right)\cdot\prod_{i=1}^{n_{\rm ON}} P(E_i,t_i|s,b,\tau_n) \tag{6.8}$$

This time, the PDF $P(E_i,t_i|s,b,\tau_n)$ associated with each gamma-like particle characterized by its time t_i and energy E_i contains two terms (signal and background):

$$P(E_i,t_i|s,b,\tau_n) = w_s\cdot P_{\rm Sig}(E_i,t_i|\tau_n) + (1-w_s)\cdot P_{\rm Bkg}(E_i,t_i) \tag{6.9}$$

where w_s is the relative weight of the signal in the ON dataset:

$$w_s = \frac{s}{s+b}. \tag{6.10}$$

$n_{\rm ON}$ is the number of events detected in the source ON region included in the fit range $[E_{\rm cut};E_{\rm max}]\times[t_{\rm min};t_{\rm max}]$. $n_{\rm OFF}$ is the number of events in the OFF regions, in the same (E, t) range; α is the inverse number of OFF regions. ${\rm Pois}(n_{\rm ON}|s+b)$ (${\rm Pois}(n_{\rm OFF}|b/\alpha)$) is the Poisson distribution with index $n_{\rm ON}$ ($n_{\rm OFF}$) and parameter $s+b$ (b/α). The likelihood function can be simplified by fixing s and b from a comparison of ON and OFF sets: $s = n_{\rm ON} - \alpha n_{\rm OFF}$ and $b = \alpha n_{\rm OFF}$. In this case, the Poisson terms are equal to 1 in Eq. 6.9.

The probability $P_{\rm Sig}$ is defined as before in section 6.1. The probability $P_{\rm Bkg}$ is defined as:

$$P_{\rm Bkg}(E_i,t_i) = \frac{1}{N_{\rm Bkg}}\cdot R_{\rm Bkg}(E_i,t_i) \tag{6.11}$$

with

$$R_{\text{Bkg}}(E,t) = \int_{E_{true}=0}^{\infty} D(E,E_{true}) A_{\text{eff}}(E_{true},t) \Lambda_{\text{Bkg}}(E_{true}) F_{\text{Bkg}}(t) dE_{true}. \tag{6.12}$$

N_{Bkg} is the normalization factor of the PDF P_{Bkg} in the range $[E_{cut};E_{max}] \times [t_{min};t_{max}]$ where the likelihood fit is performed:

$$N_{\text{Bkg}} = \int_{t=t_{min}}^{t_{max}} \int_{E=E_{cut}}^{E_{max}} R_{\text{Bkg}}(E,t) dE dt \tag{6.13}$$

$P_{\text{Bkg}}(E_i,t_i)$ is not expected to be variable with time, thus $F_{\text{Bkg}}(t)$ is a uniform time distribution: $F_{\text{Bkg}}(t) = F_{\text{Bkg}}$. The background energy distribution Λ_{Bkg} is measured from the OFF regions.

The final form of the unbinned likelihood function is given by:

$$\mathcal{L}(\tau_n) = \prod_{i=1}^{n_{ON}} w_s \cdot P_{\text{Sig}}(E_i,t_i|\tau_n) + (1-w_s) \cdot P_{\text{Bkg}}(E_i,t_i) \tag{6.14}$$

with the relative weight of the signal fixed as:

$$w_s = \frac{n_{ON} - \alpha n_{OFF}}{n_{ON}}. \tag{6.15}$$

As before, the best estimate $\widehat{\tau}_n$ of the dispersion parameter τ_n is obtained by maximizing the likelihood $\mathcal{L}(\{E_i,t_i\}_{i\in[1;n_{ON}]}|\tau_n)$.

6.1.2.1 Possible simplifying assumptions

Similar assumptions as for the background-free formulation can be made. In particular, assuming a perfect energy resolution $D(E,E_{true})$ leads to simplified expressions of $P_{\text{Sig}}(E_i,t_i|\tau_n)$ and $P_{\text{Bkg}}(E_i,t_i)$:

$$P_{\text{Sig}}(E_i,t_i|\tau_n) = \frac{1}{N_{\text{Sig}}(\tau_n)} \cdot A_{\text{eff}}(E_i,t_i) \Lambda_{\text{Sig}}(E_i) F_{\text{Sig}}(t_i - \tau_n \cdot E_i^n) \tag{6.16}$$

$$P_{\text{Bkg}}(E_i,t_i) = \frac{1}{N_{\text{Bkg}}} \cdot A_{\text{eff}}(E_i,t_i) \Lambda_{\text{Bkg}}(E_i) F_{\text{Bkg}} \tag{6.17}$$

6.1.3 Template light curve determination

The time distribution at the source is needed in the formulation of the likelihood function. It can be obtained with a model of the time emission or from a subset of the data. In order to be as model-independent as possible, the template was retrieved from a parameterization of the low energy subset of events. The sub-dataset used to derive the light curve template was not kept for the likelihood fit.

There are at least three ways of getting a template from the data:

1. binning the data and taking the resulting histogram itself – normalized to 1 – as a PDF;
2. fitting the histogram with a given parameterization. Depending on the shape of the binned light curve histogram, the fitting function could be a single Gaussian or the sum of Gaussian functions, a single asymmetric Gaussian function or a sum of several

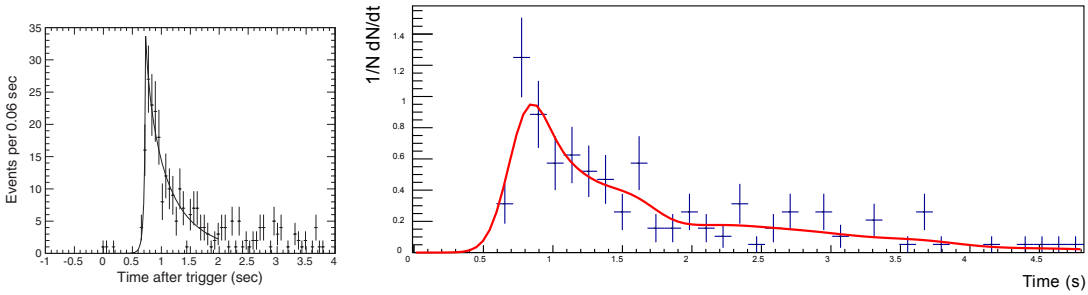

Figure 6.1: Templates for GRB090510 light curve. On the left, a parameterization using a fit of the data to a Norris function. On the right plot, a Kernel Density estimation of the data, with a Gaussian kernel. The histogram (third template estimation) is displayed on both plots, with different binnings.

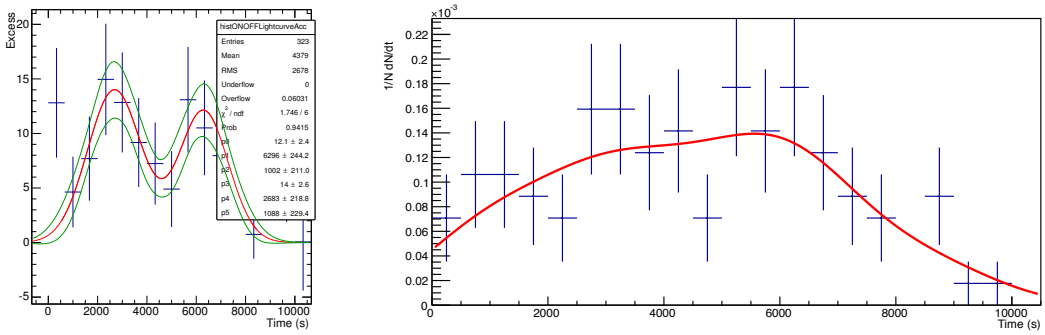

Figure 6.2: Templates for PG 1553+113 light curve. On the left, a parameterization using a fit of the data to a Double Gaussian function. On the right plot, a Kernel Density estimation of the data, with a Gaussian kernel. The histogram (third template estimation) is displayed on both plots, with different binnings.

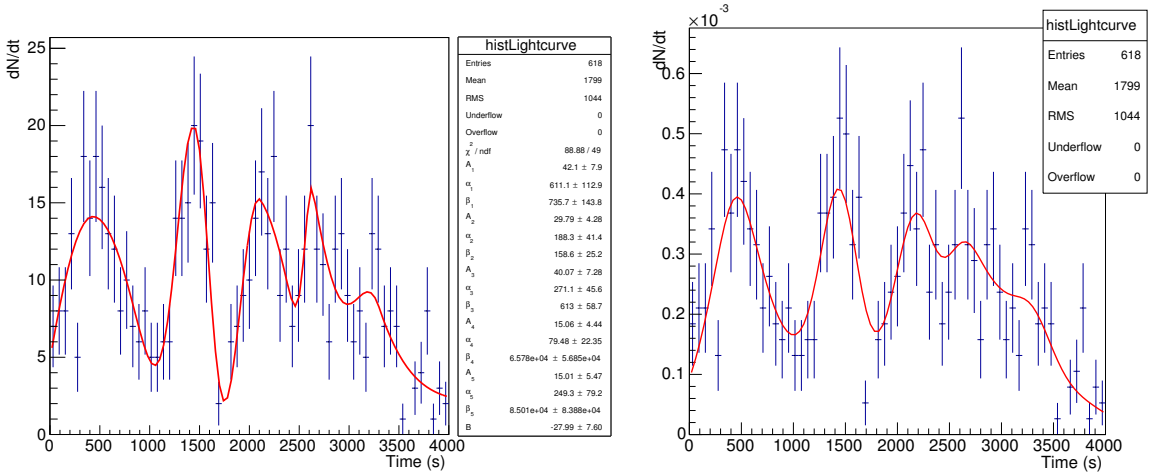

Figure 6.3: Templates for PKS 2155–304 light curve. On the left, a parameterization using a fit of the data to the sum of 5 asymmetric Gaussian functions. On the right plot, a Kernel Density estimation of the data, with a Gaussian kernel. The histogram (third template estimation) is displayed on both plots, with the same binning but different normalization.

asymmetric Gaussian functions, a Norris parameterization (fast rise functions), or others functions.

3. a Kernel Density Estimate (KDE) of the distribution. Different Kernels are available: most used are Gaussian and triangular kernels.

The first two options have been used extensively in previous works (e.g. [14]) and do not need additional description.

The KDE of the distribution of a given dataset $\{t_i\}_{i\in[1;n]}$ is:

$$f_0(x) = \frac{1}{nh}\sum_{i=1}^{n} K\left(\frac{x-t_i}{h}\right)$$

where K is the "kernel", *i.e.* a normalized even function with a maximum at 0 and h is a smoothing parameter (the "bandwidth"). Thus the contribution of each point is spread, represented by the kernel $K\left(\frac{x-t_i}{h}\right)$. A common choice of K is a Gaussian with mean = 0 and width = 1:

$$K(x) = \frac{1}{\sqrt{2\pi}}\exp(-x^2/2)$$

This allows a good definition of the estimate, especially at the edges of the distribution: continuous and differentiable on $\mathbb{R}$. More details on the kernel density estimate can be found in Appendix B.

Examples of the three possible templates used later are shown for the following sources: GRB090510 (Figure 6.1), PG 1553+113 Flare of April 2012 (Figure 6.2) and PKS 2155–304 Big Flare (Figure 6.3). The left hand-side plots show a parameterization using fits to the data, while the plots on the right-hand side demonstrate a Kernel Density estimation of the data, with a Gaussian kernel. The histogram is displayed on both plots, with different binnings.

6.1.4 Confidence intervals and coverage

In addition to the confidence intervals (CIs) obtained on the data sample from a given cut on the likelihood profile, the confidence intervals will be calculated using Monte Carlo simulated sets. This will allow a better estimation of the statistical uncertainties associated with the dispersion measurement. Indeed, the measurement of the dispersion parameter on the original dataset very much relies on the luckiness of the unique observation.

The simulated sets should have the same statistics, light curve model and spectrum as the original data. No intrinsic dispersion was included when determining the CIs. Each simulated data set produced a lower limit and an upper limit on τ_n from cuts on the likelihood profile, besides the best estimate $\hat{\tau}_{\rm best}$. The calibrated lower (upper) limit of the CI is taken as the mean of the distribution of the per-set individual lower (upper) limits.

Additional steps are needed to get a proper coverage. The procedure is iterative: we first set a fixed cut value on the likelihood profile $-2\Delta\ln L(\tau)$, which allow us to get individual CIs – a lower limit (LL) and an upper limit (UL) – for this particular cut. We then count the number of sets which give a CI that contains the true (i.e. simulated) value $\tau_{\rm inj}$: if this number corresponds to the desired confidence level, we keep the current cut value, otherwise the cut is changed until the coverage is insured. We define the lower (upper) limit LL^{MC} (UL^{MC}) for the measurement as the mean of the per-set LLs (ULs).

The CIs will be produced for a 95% 1-sided confidence level (CL), approximately equivalent to a 90% 2-sided CL.

The method described in this section was thoroughly tested with a Monte Carlo (MC) procedure.

6.2 Testing the method and the impact of the data with Toy Monte Carlo simulations

In order to estimate the sensitivity of the method and understand how the various input assumptions affect the results, tests on simulated datasets were conducted. The present section focuses on general aspects of the method such as the impact of the reconstruction algorithm on the LIV analysis, the performance of the method (linearity curve) or the parameters related to measurement conditions which affect the most the results.

Dedicated tests for specific analyses (PG 1553+113 and Fermi GRBs) will be detailed in the next chapters.

6.2.1 Toy Monte Carlo simulations

The common hypotheses for the MC set production were as follows:

— the simulation is for H.E.S.S.-1 only, for a configuration with 4 participating telescopes;

— the light curve produced is meant for illustrating a simple though typical AGN time profile as observed with H.E.S.S.-1: a perfect Gaussian profile;

— there is no injected spectral variability, *i.e.* the photon index of the power law spectrum does not evolve with time.

More complex cases (asymmetric light curve, double Gaussian, spectral evolution) will be studied in more detail in the next chapters, and give rise to specific Monte Carlo studies.

The initial parameters injected in the simulations were:

— n_{ON} = 900 ON events, with S/B = 2; so about $s = 600$ signal events and $b = 300$ background events;

— n_{OFF} = 3000 OFF events, with 10 OFF regions considered (background estimation with Multiple-OFF subtraction), equivalent to 300 weighted OFF events;

— $t_{min} = 0\,s$ and $t_{max} = 5000\,s$;

— single Gaussian light curve for the signal: centered around 2500 s, width of 1000 s;

— uniform background light curve;

— events were simulated with energies ranging from 100 GeV to 50 TeV;

— template determination: E_{min} = 200 GeV, E_{cut} = 400 GeV;

— fit range: E_{cut} = 400 GeV, E_{max} = 5 TeV;

— power-law spectrum with a photon index Γ_{Sig} of 3.5 for the signal;

— power-law spectrum with a photon index Γ_{Bkg} of 2.5 for the background;

— energy resolution and bias: no bias, E_{rec} drawn from a Gaussian centered around E_{true} with a width equal to 10% of E_{true};

— the acceptance is not variable with time and uniform for all energies.

To test its impact, each parameter was varied within observed variation in the analysed data samples. The modifications from these initial values will be mentioned when needed. In the next section, we will perform the likelihood analysis explained in section 6.1, varying the input parameters of the sets or the PDF formulation depending on the aspects to be probed.

Simulation procedure

Each set was composed of $n_{ON} = n_S + n_B$ ON events, as in the real data sample:

— s signal events (index i) were simulated following the procedure:

1. arrival times t_i were simulated from the template light curve, and then shifted by a factor $\tau_{n,\mathrm{inj}} \cdot \mathrm{E}_i$: $t'_i = t_i + \tau_{n,\mathrm{inj}} \cdot \mathrm{E}_i$, with injected dispersion $\tau_{n,\mathrm{inj}}$ from –1000 s/TeV to +1000 s/TeV for the linear case (n = 1) and from –1000 $\mathrm{s\,TeV^{-2}}$ to +1000 $\mathrm{s\,TeV^{-2}}$ for the quadratic case (n = 2);
2. energies E_i follow a power-law spectrum of photon index Γ_{Sig}, convoluted with the acceptance $A_i(E_{\mathrm{true}})$ and smeared by the energy resolution.

— b background events (index j) were produced in the same way as the signal events, except that the times t_j were not shifted since no LIV effect is expected. They were produced following a power-law spectrum of index Γ_{Bkg}, convoluted with the acceptance and smeared by the energy resolution.

6.2.2 Tests on the method

Different aspects of the method were studied by comparing, on simulated sets, the value of the dispersion τ_{inj} injected in the simulations with the dispersion τ_{rec} reconstructed with the ML method on those sets.

6.2.2.1 Refit of the template light curve *vs.* no refit

When applying the method on data, the template is obtained from a fit of the arrival time distribution of the low energy subset of events. To apply the exact same procedure on the simulated sets, the low energy time distribution should be fitted for each realization ("refit"). This requires a careful check of the quality of each fit. Alternatively, one can take the lightcurve model used to simulated the sets instead of performing a refit of the template.

New simulated sets – smaller in size (100 sets of 90 ON events and 1000 sets of 30 OFF events) – were processed within the likelihood fit, with and without a refit of the template light curve derived from the lowest energy events. Resulting linearity curves are given in Figure 6.4. The slope is softer when refitting the light curve for each realization: this is due to the fact that the template has already been shifted. Figure 6.5 shows the detailed distributions (best estimate, lower limits, upper limits) for $\tau_{\mathrm{inj}} = 0\,\mathrm{s/TeV}$. Refitting the low-energy light curve for each realization is very CPU time-consuming. In the following tests, the template will be fixed once for all datasets.

6.2.2.2 Energy resolution

The same simulated sets were processed within the maximum likelihood method, either considering the actual energy resolution or assuming a perfect energy reconstruction.

Making the assumption, in the formulation of the PDF, of a perfect energy reconstruction leads to a maximum change of 10% in the measure of the dispersion parameter. This works very well for GRBs in Fermi. The same approach was used for the analysis of PG 1553+113 where the results are mainly dominated by statistical limitations. A PDF created using a integral is quite slow to evaluate numerically. Thus a perfect energy reconstruction, not requiring the integration over the true energy, will be assumed in the following tests.

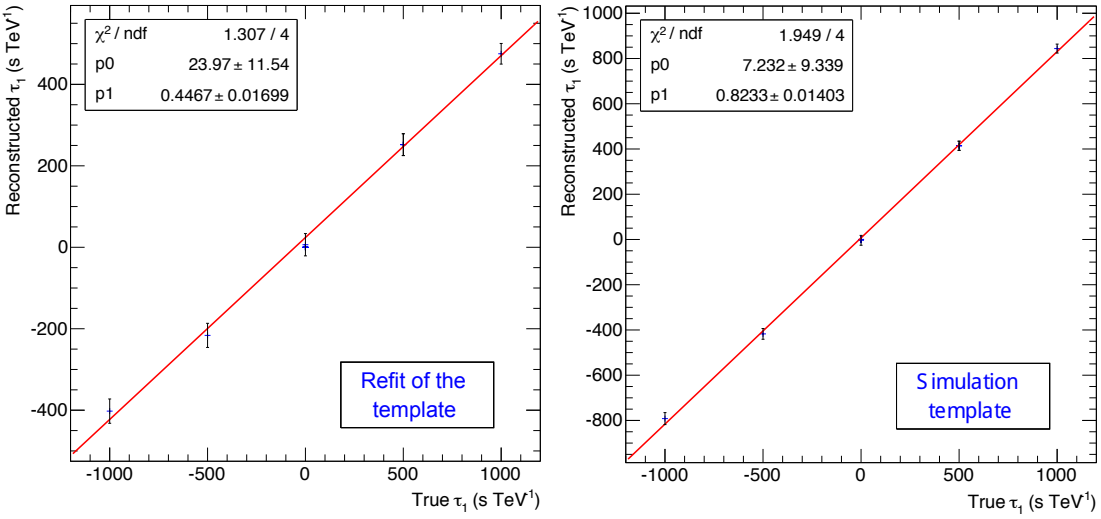

Figure 6.4: Linearity curves obtained with (left) and without (right) refitting the template light curve to the lowest energy events. The slope is less steep when refitting the light curve for each realization: the low-energy photons used in the template have indeed been shifted.

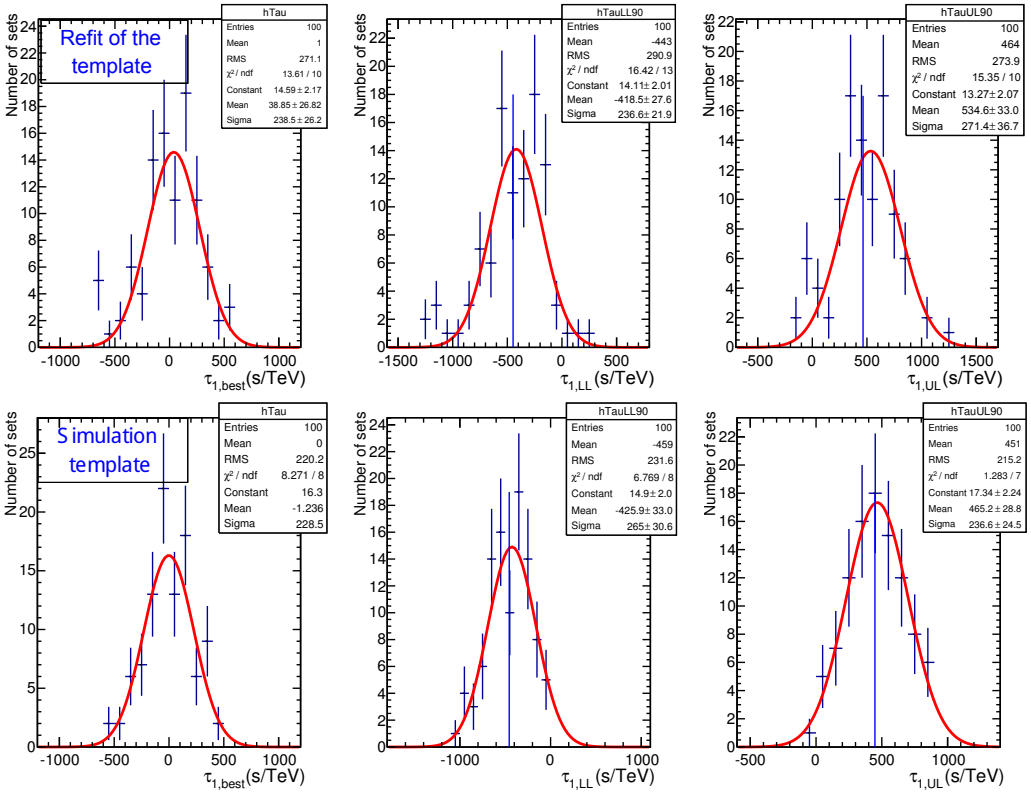

Figure 6.5: Distributions of the best estimates, the 95% 1-sided lower and upper limits from simulations in case of no injected dispersion ($\tau_{\rm inj} = 0\,$s/TeV), in two cases: refit of the low energy events to obtain the light curve model (top) and with keeping the set production template (bottom). The blue vertical line on the LL (resp. UL) distribution shows LL_{MC} (resp. UL_{MC}), defined as the mean of the distribution.

6.2.3 Tests on input parameters defined for the MC datasets

6.2.3.1 Impact of the background contamination

Different sets were simulated with various S/B ratios: S/B $\to \infty$, S/B = 3, 1, 1/3 and 0. Resulting linearity curves are given in Figure 6.6.

As the relative proportion of background events in the dataset increases, the method probes only a fraction of input parameters. The slope of the linearity curve follows the ratio of signal events in the ON dataset.

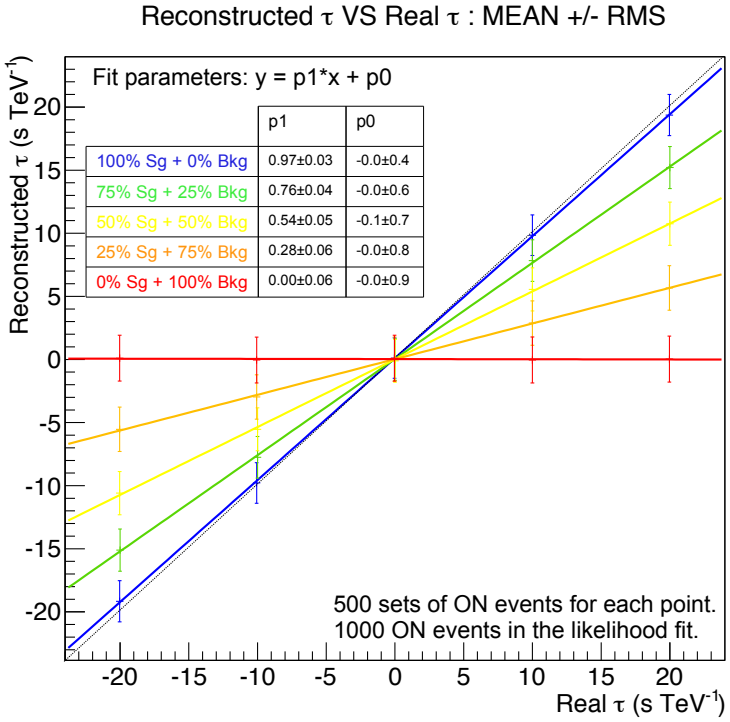

Figure 6.6: Linearity curves for the maximum likelihood method, for various S/B ratios (∞, 3, 1, 1/3 and 0). The errors bars correspond to 1 standard deviation of the distribution of the best estimates.

6.2.3.2 Impact of the energy distribution

Signal events were simulated with energies following power-law spectra with two different photon indexes: $\Gamma = 3.5$ and $\Gamma = 4.5$. Resulting linearity curves are given in Figure 6.7. No big difference can be seen in the fit values between the two cases. The distribution for individual injected dispersion are more spread for $\Gamma = 4.5$; for instance, at $\tau_{\rm inj} = 0\,$s/TeV, the standard deviation of the distribution for $\Gamma = 3.5$ is $\sim 40\,$s/TeV while it is $\sim 70\,$s/TeV for $\Gamma = 4.5$. It results in a better χ^2 for the latter case.

The fact the results are closely similar for two different photon indexes: the energy template in the likelihood model is indeed a weighting factor, and does not probe directly the dispersion parameter. In that sense, it is of lesser importance than the light curve template in the obtaining of the results. This guarantees that we can safely forget the acceptance term in the likelihood formulation (see Section 6.1.1.1).

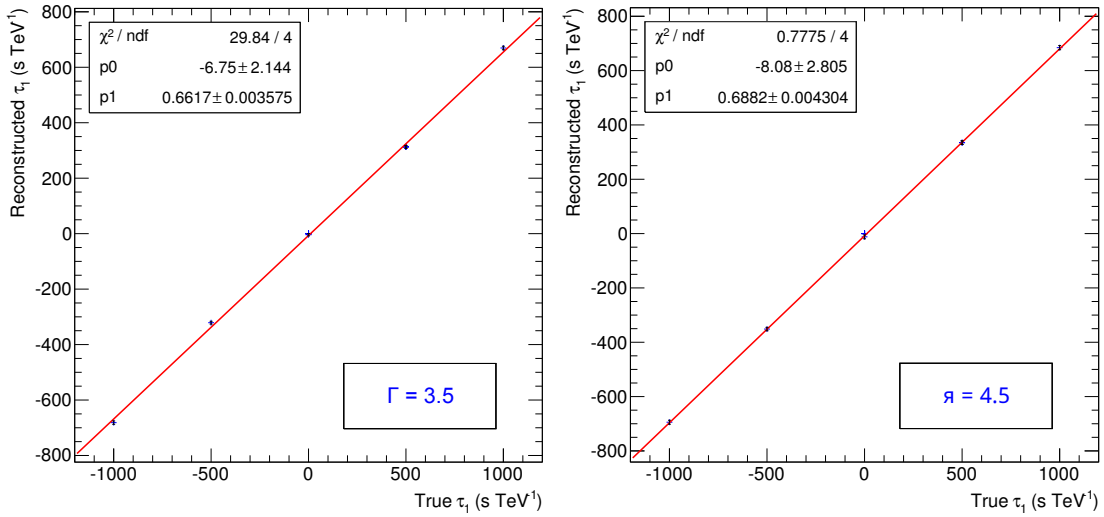

Figure 6.7: Linearity curves obtained from the application of the ML method on sets with different energy distributions: photon indexes $\Gamma = 3.5$ (left) and $\Gamma = 4.5$ (right) . Vertical bars show the error on the mean of the best estimates. No big difference can be seen in the fit values between the two cases. The distribution for individual injected dispersion are more spread for $\Gamma = 4.5$; for instance, at $\tau_{\rm inj} = 0\,$s/TeV, the standard deviation of the distribution for $\Gamma = 3.5$ is $\sim 40\,$s/TeV while it is $\sim 70\,$s/TeV for $\Gamma = 4.5$. It results in a better χ^2 for the latter case.

6.2.3.3 Impact of the width of the light curve

Signal events were simulated with two different width for the Gaussian template light curve: 1000s and 2000s. Resulting linearity curves are given in Figure 6.8. No big difference can be seen in the fit values between the two cases. The distribution for individual injected dispersion are more spread for a wider light curve template; for instance, at $\tau_{\rm inj} = 0\,$s/TeV, the standard deviation of the distribution is $\sim 40\,$s/TeV and $\sim 115\,$s/TeV for a width of $1000\,$s and $2000\,$s respectively. It results in a better χ^2 for the latter case.

6.2.3.4 Impact of the reconstruction method and analysis cuts

Reconstruction method and analysis cuts have an impact on the signal-to-background ratio S/B and on the total number of photons detected, obtained from the number of events in the observation region ("ON"), subtracting the weighted number of events in the "OFF" regions: $n_{\rm ON} - \alpha n_{\rm OFF}$. Typically, using Loose cuts rather than Standard cuts, one can gain 1.5 time the number of photons, at a cost of a S/B signal decreased by a factor 2. The following two cases are compared:

— Loose cuts: S/B = 2 and $n_{\rm ON} = 500$

— Standard cuts: S/B = 4 and $n_{\rm ON} = 200$

Resulting linearity curves are shown in Figure 6.9.

The reconstruction of the dispersion parameter τ_n is more biased with the "Loose" cuts: the slope of the linearity curve does not follow $\tau_{\rm rec} = \tau_{\rm inj}$.

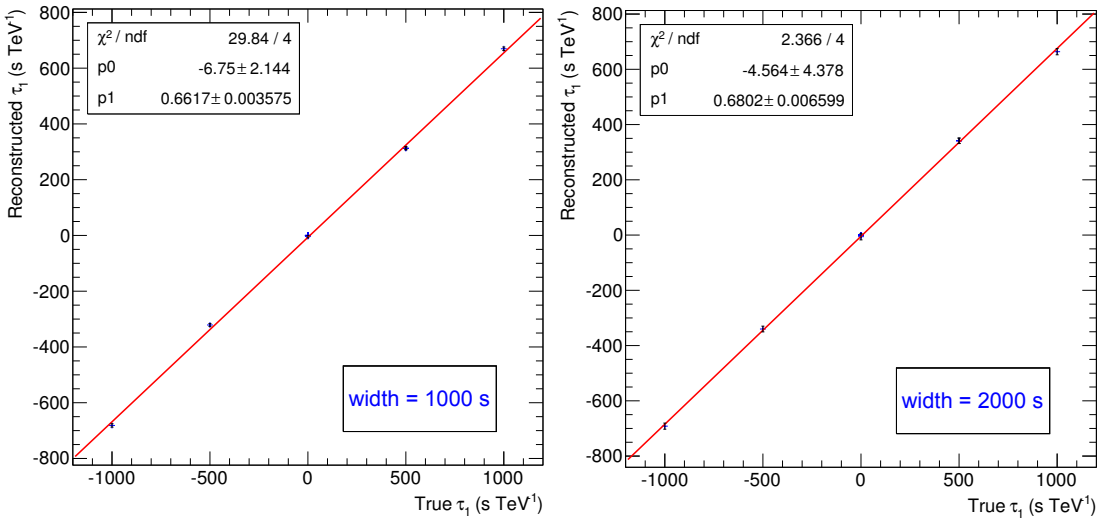

Figure 6.8: Linearity curves obtained from the application of the ML method on sets simulated from light curve templates with different widths: photon indexes 1000s (left) and 2000s (right). Vertical bars show the error on the mean of the best estimates. No big difference can be seen in the fit values between the two cases. The distribution for individual injected dispersion are more spread for a wider light curve template; for instance, at $\tau_{\rm inj} = 0\,$s/TeV, the standard deviation of the distribution is $\sim 40\,$s/TeV and $\sim 115\,$s/TeV for a width of 1000 s and 2000 s respectively. It results in a better χ^2 for the latter case.

6.3 Summary of the tests

The tests done with MC simulated data allow to get a first idea of the best conditions for using the maximum likelihood method to retrieve the dispersion with the measured data sample and to evaluate the most important systematic effects in the foreseen analyses:

— taking into account of the true energy resolution: assuming a perfect energy resolution leads to a change of about 10% only in the measured value of the dispersion parameter.

— template production: parameterization of the light curve is preferably to be used in all cases, especially in the presence of non-negligible background, or when the flux is not negligible at the beginning and/or at the end of the observation time interval. However, the use of a KDE -derived template can be pertinent in case of no background and negligible fluxes at the edges of the lightcurve, specifically for more complicated curves (2 peaks or more, asymmetric shapes).

— Standard cuts are preferred over Loose cuts for a more accurate determination of the dispersion parameter τ_n. It is not always possible to use Standard cuts, though; *e.g.* for the analysis of PG 1553+113 (next chapter), the use of Loose cuts was strongly advised to perform varied analyses on the exact same dataset (spectrum determination for rather faint blazars is done using Loose cuts), in spite of the fact they lead to slightly less precise results on the dispersion parameter determination.

The most favorable conditions actually depend on the specific observations; they will be given case by case in the following chapters.

As a general conclusion, the systematic uncertainties were found to come mainly from the background contribution (misidentification of the highest energy particles) and the determination of the light curve template. Other aspects of the data (photon index of the spectrum,

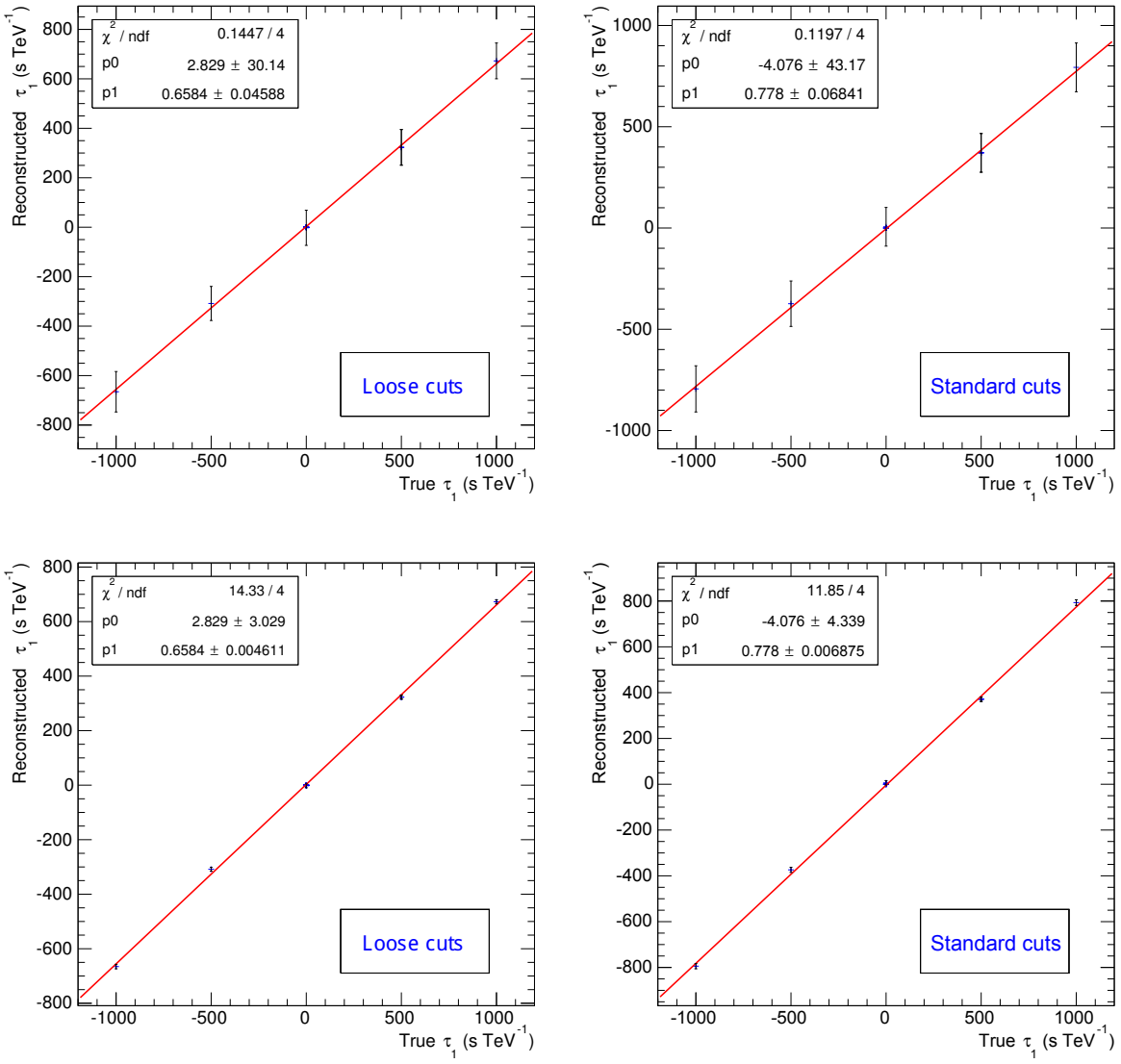

Figure 6.9: Linearity curves obtained with datasets emulating two different reconstruction configurations: Loose cuts (left) *vs.* Standard cuts (right). Top: errors are taken as the standard deviation of the distributions of the best estimates; Bottom: errors are taken as the error on the mean. Note that the quality of the fits in the bottom plots is poor (large χ^2): this shows that there are systematic uncertainties not taken into account in the fits. The reconstruction of the dispersion parameter τ_n is more accurate with "Standard" cuts, the slope of the linearity curve $\tau_{\rm rec} = f(\tau_{\rm inj})$ being closer to 1.

energy resolution, determination of the effective area) do not influence much the results (change up to 10%).

All systematics were not studied in this chapter as they depend on the physics case. Dedicated studies will be developed in the sections related to the analysis of the different types of sources.

6.4 Fast check with PKS 2155–304 sample

As an illustration, we applied the presented method on the H.E.S.S. flare data taken on MJD 53944 (July 2006), with templates taken as a sum of asymmetric Gaussians (from [14]) and as the KDE of the distribution. The following cuts were applied on the data:

— only the first 4000 s of data (7699 events) were considered;

— the template light curve was derived from the events with energies between 0.25 and 0.28 TeV;

— the likelihood fit is performed in the range 0.3–4 TeV;

Selections applied to the data are summarized in Table 6.1.

Table 6.1: Selections applied to the data

Selection	Number of selected events
Total sample	8126 (100 %)
(1) = Time in 0–4000 s	7699 (95 %)
(1) and E in 0.25–4.0 TeV	3693 (43 %)
(1) and E in 0.25–0.28 TeV	561 (7 %)

Figure 6.3 shows the light curve in the range 0.25–0.28 TeV with a binning of 61 s. On the left hand-side plot, a fit using a sum of 5 asymmetric Gaussians was done. On the right hand-side plot, the template was derived using the Kernel density estimate of the distribution.

Resulting likelihood profiles are given in Figure 6.10. Both curves are really similar, and give the same best estimate of the dispersion parameter τ_n; the 95% 1-sided LL and UL are different (see Table 6.2). In this particular case, using the parameterization yields a more precise measurement (narrower profile).

In both cases, the obtained values point to non-zero value of τ_1. However these results are at the level of 2 standard deviation, and cannot be considered as significant.

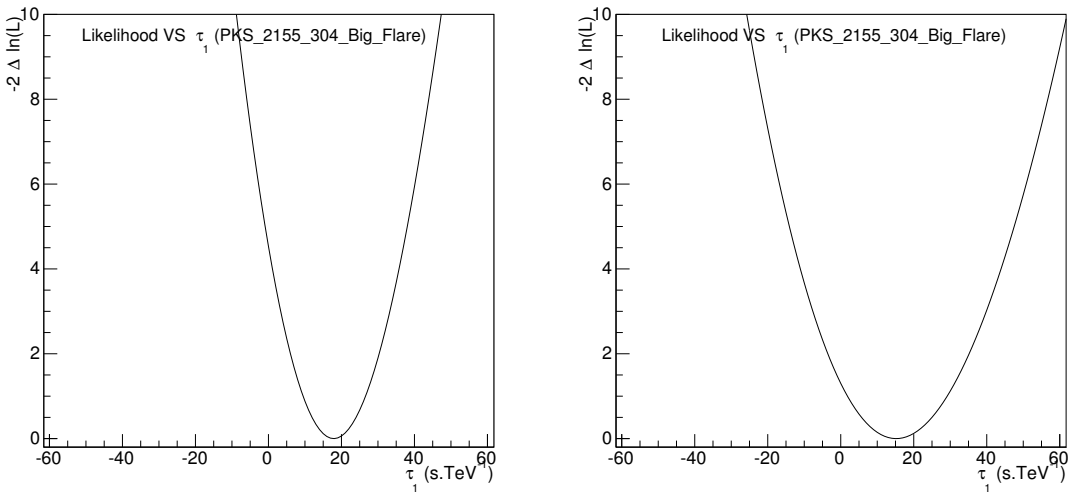

Figure 6.10: Likelihood profiles from the application of the ML method on the data of the "Big" flare of PKS 2155–304. Left, profile using a sum of asymmetric Gaussians as a template light curve; right, using the KDE of the time distribution.

Template	$\tau_{1,best}$	LL	UL
Parameterization	18	4	32
KDE	15	-7	39

Table 6.2: Linear dispersion parameter obtained with the two different templates from the data of PKS 2155–304 "Big" flare of 2006: best estimate, 95% 1-sided LL and UL. Dispersion parameters $\tau_{1,best}$, LLs and ULs are in s TeV^{-1}.

In the next two chapters the application of the maximum likelihood methods on the data will be detailed for two kind of sources: an AGN flare detected by H.E.S.S. (low statistics, high level of background), and 4 GRBs detected by *Fermi*-LAT (clean light curves, no background, spectral variability for some of the GRBs).

6.5 Conclusion

The maximum likelihood method presented in this chapter is well suited for precision measurement of the dispersion parameter τ_n in the data presenting flares. For the special case of a flare with non-negligible background, a procedure was also developed.

The tests with Monte Carlo simulated samples with a simple Gaussian light curve template allowed us to estimate features and the sensitivity of the method. The systematic uncertainties were found to be mostly under control, and depend on the source data considered further in this work. Specific tests will be conducted in the next chapters when analyzing GRBs observed with *Fermi* and an AGN flare observed with H.E.S.S..

Chapter 7

Search for Lorentz Invariance violation with a likelihood fit of the data of PG1553+113 flare of April 2012 observed with H.E.S.S.

Contents

In this chapter, the results obtained with the likelihood method applied to the data of a blazar at a high redshift – PG 1553+113 – will be presented. They have led to a publication of the H.E.S.S. Collaboration [73]. As explained in Chapter 2, blazars are AGNs for which one of the beamed jets is closely aligned to the Earth. Some of them are subject to variability in the GeV–TeV range.

In parallel to the data sample analysis, large number of sets simulated with a Monte Carlo procedure will allow a proper estimation of the statistical aspects of the measurement. The likelihood method described in the previous chapter will be applied first on the simulations, then on the real flare dataset, in order to measure the dispersion and provide 95% 1-sided [1] lower and upper limits on the dispersion parameter τ_n.

1. Note on the confidence level (CL) and confidence intervals (CIs), from [74]:
Confidence intervals are constructed at a confidence level, such as 95 %, selected by the user. It means that if the same population is sampled on numerous occasions and interval estimates are made on each occasion, the resulting intervals would bracket the true population parameter in approximately 95 % of the cases. A confidence stated at a 1-α level can be thought of as the inverse of a significance level, α. Confidence intervals can be one or two-sided. A two-sided confidence

7.1 The PG1553+113 Flare

7.1.1 Presentation of PG1553+113

The very high energy (VHE) emission of PG 1553+113 was discovered by H.E.S.S. following the observations taken in 2005 (publication in 2006 [75]). The emission was then characterized by a very soft energy distribution above 200 GeV, compatible with a power-law spectrum of photon index 4.0 ± 0.6. Danforth *et al.* [76] constrained its redshift between 0.43 and 0.58; these are the strongest constraints of the redshift of this source until now. A measure of the redshift of 0.48 has been recently proposed by the H.E.S.S. Collaboration [73], using a Bayesian model and properties of the Extragalactic Background Light (EBL). This value will be used to derive the modified cosmological distance and place the limits on the E_{QG} scale, in section 7.2.7.

A flare of this source was detected by MAGIC in April 2012 [77]. H.E.S.S. was able to observe the flare during the nights of April 26th and 27th, 2012.

7.1.2 Flare dataset – Analysis with ParisAnalysis 0-8-24

A total of eight runs of 28 minutes were taken with 4 telescopes during the flare. To perform the dispersion studies, only uninterrupted data have been kept, thus the analysis was conducted on the first 7 runs, taken during the night of April 26th Since this blazar is a point-like source with known position, one of the best strategies of observation is the wobble mode: the source is observed with an offset (here $\pm 0.5°$) in declination or in right ascension; the sign of the offset alternates between two successive runs. Last column of Table 7.1 shows the values of the offset of each run. This enables a background removal technique using multiple OFF subtraction regions in the field of view. Unlike separate ON and OFF data-taking, it keeps the same conditions for signal and background observations and enhances the sensitivity to the gamma signal.

The reconstructed data sample from the seven non-truncated runs was obtained using the Model++ analysis, described in chapter 3. The reconstruction was performed using "Loose" cuts, requiring a minimum of 40 photoelectrons in each camera in order to process a camera image [54]. It resulted in 461 on-source events recorded during the live time with an energy threshold of 240 GeV.

Figure 7.1 shows the squared angular distribution of the events for the 7 considered runs. The total significance of the signal is 19.4 σ. Table 7.1 shows the analysis output for each of the runs: the signal yields more than 5 σ in each of the 5 first runs. Hence, the source is detected by H.E.S.S. in all except the last two runs.

Spectrum and light curve

Determining the spectrum and light curve of this flare is of a primary importance for the LIV studies. Indeed, the fit of these two distributions – in energy and in time – are part of the model used in the maximum likelihood calculation.

To get the differential flux spectrum, a forward folding method was applied [58]: the energies of the detected events were fitted to a given spectral shape – here a power-law function. The result of the fit is given in Figure 7.2: the photon index is 4.8 ± 0.3, which corresponds to a very steep spectrum. The spectral points were not used in the forward-folding fit; they are only shown here for illustration. The fit results obtained in this analysis (7 runs) are compatible with the results published in the flare paper [73], which has an extended run selection (8 runs).

interval brackets the population parameter from above and below. A one-sided confidence interval brackets the population parameter either from above or below and furnishes an upper or lower bound to its magnitude.

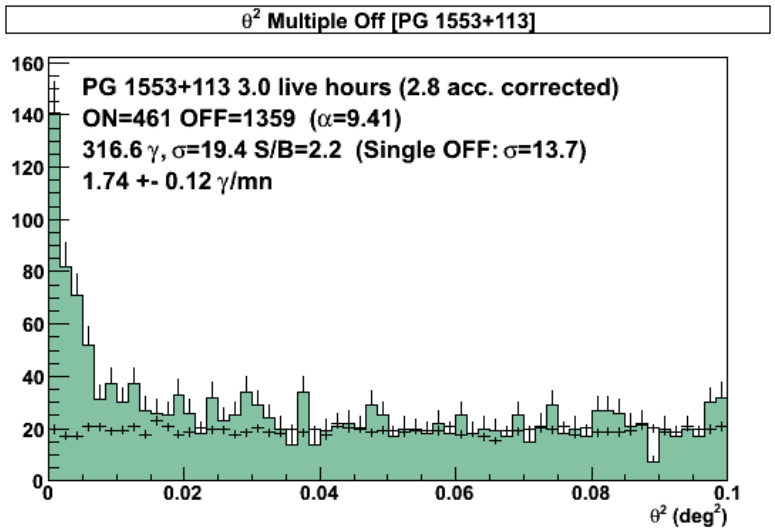

Figure 7.1: θ^2 distribution of the events in the ON and OFF regions. A selection cut at $\theta^2 = 0.0125\,\mathrm{deg}^2$ was set because of Loose cuts. The selected events were used for the calculation of the significance and signal-over-background ratio and were kept for the following LIV analysis.

Run number	n_{ON}	n_{OFF}	α	n_γ	S/B	σ	live time (h)	Offset	
								RA	Dec
70971	63	208	10	42.2	2.0	6.9	0.4	0	−0.5
70972	90	202	9	67.6	3.0	9.8	0.4	0.5	0
70973	83	216	9	59.0	2.5	8.6	0.4	−0.5	0
70974	94	213	10	72.7	3.4	10.6	0.4	0	0.5
70975	57	178	10	39.2	2.2	6.8	0.4	0	−0.5
70976	40	181	9	19.9	1.0	3.6	0.4	0.5	0
70977	34	161	9	16.1	0.9	3.2	0.4	−0.5	0
TOTAL	461	1359		316.7	2.2	19.4	2.8		

Table 7.1: Analysis output per run (Loose cuts): number of gamma-like events in the ON (observation) and OFF (estimation of the background) regions, number α of OFF regions considered, estimation of the number of signal events, significance of the detection determined with the Li and Ma formulation [56], live time. Last column shows the values of the wobble offset for each run.

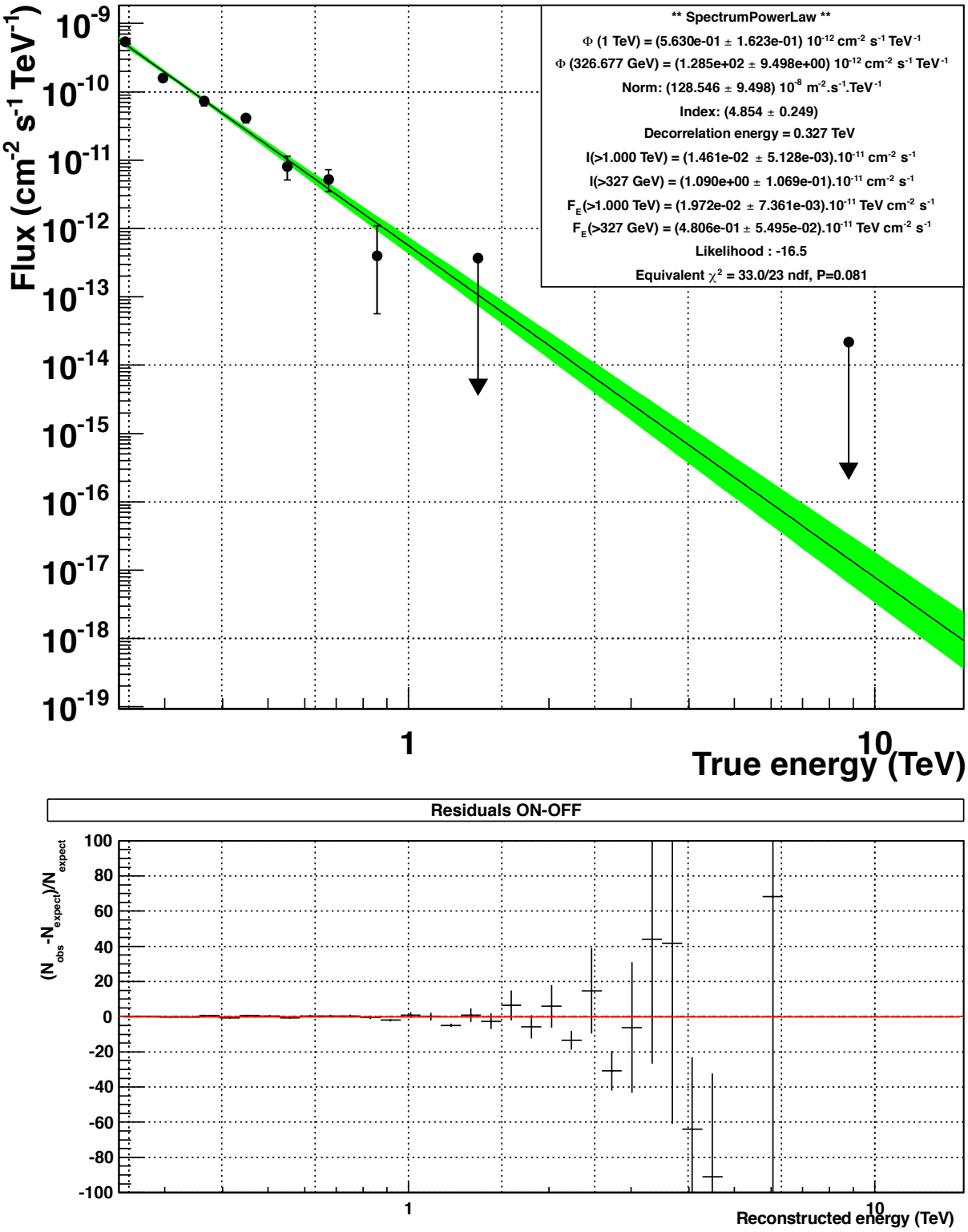

Figure 7.2: Differential flux measurement for PG 1553+113 during the night of April 26th, 2012, obtained with the forward folding method assuming it follows a power-law spectrum. The green area indicates the 1σ confidence contour (statistical errors only). The spectral points were computed so that their significance is above 3 σ each. Bottom plot represents the residuals.

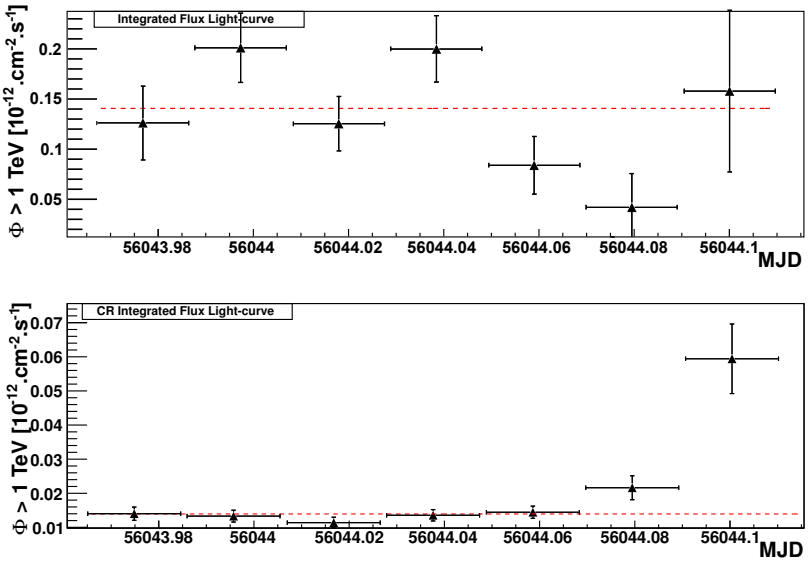

Figure 7.3: Run-integrated fluxes above 1 TeV for the signal (gamma-rays, top) and the background (cosmic rays, bottom) for PG 1553+113 during the night of April 26th 2012. Both fluxes show an evolution over the night. Notice the large statistical errors in the last run.

Figure 7.3 shows the fluxes integrated over the run duration, above 1 TeV, for the signal (gamma-rays) and the background (cosmic rays). The signal light curve shows a variation during the night: the 3rd and 5th runs emerge from the rest of the runs.

The background light curve also shows an evolution during the night. In particular, the cosmic ray flux increases a lot for the last run, due to a variation of the zenith angle during this night. This fact, along with its large statistical errors, leads us to remove the last run from the LIV analysis.

The cosmic ray flux variation may come from a change in the conditions of observation during the night; this encourages us to study them in more detail.

7.1.3 Evolution of the conditions of observations

The changing conditions of observation during the night influence the detection of the signal and background events. In this analysis all information on the changing conditions has been included when calculating the effective area, taking into account the zenith angle, the muon efficiency and the off-axis angle. The following distributions have been retrieved from the analysis output from ParisAnalysis files.

Zenith angle

The curve on Figure 7.4 corresponds to the evolution of the mean zenith angle with time, during the night (t = 0 at the beginning of the observation). The angle varies between 34° and 47°. Though the zenith angle of the source varies continuously during the night, jumps are observed in this curve: they are due to the observation in wobble mode, two consecutive runs having different offsets (see Table 7.1).

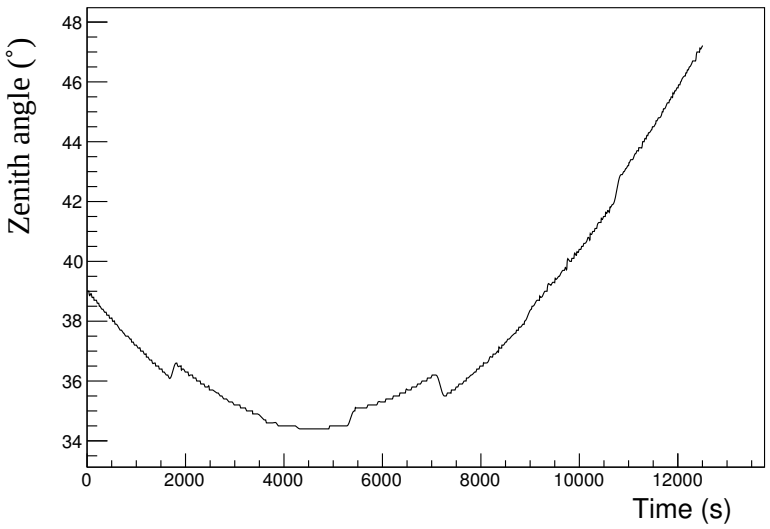

Figure 7.4: Evolution of the zenith angle, averaged over the four telescopes, over the night of April 26th, 2012. It varies from $\theta = 34°$ to 47°. The jumps observed are due to the observation in wobble mode, two consecutive runs having different offsets.

Off-axis

The observations were taken in wobble mode: the source was observed in a fixed off-axis position of 0.5°. However the off-axis angle fluctuates around the nominal requested value. Figure 7.5 shows its distribution, with a standard deviation of 0.06°.

Optical efficiency

The relative optical efficiency was considered to be constant during the night with a value of 0.6.

Effective area

Figure 7.6 gives the effective area in m^2 as a function of the cosine of the zenith angle and the logarithm of the energy of the detected events, for fixed values of the off-axis angle (0.5°) and of the optical efficiency (0.6). The values have been obtained from simulations and depend also on the analysis chain – here Model++ – and on the cuts applied to the discriminant variables – here ShowerGoodness – as described in Chapter 3.

This plot, along with the evolution of the zenith angle during the night, can explain the variation of the cosmic ray flux over the night. Indeed, a larger zenith angle (telescope pointing lower on the horizon) leads to a higher energy threshold, and to a larger collecting surface at higher energy. The telescopes are then more sensitive to energetic hadron showers. These changes in effective area have to be taken into account in the simulations (next section).

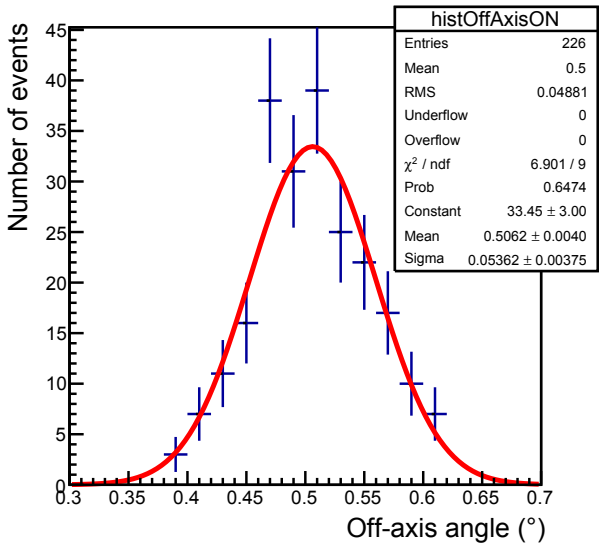

Figure 7.5: Distribution of the off axis angles during the night of April 26th, 2012.

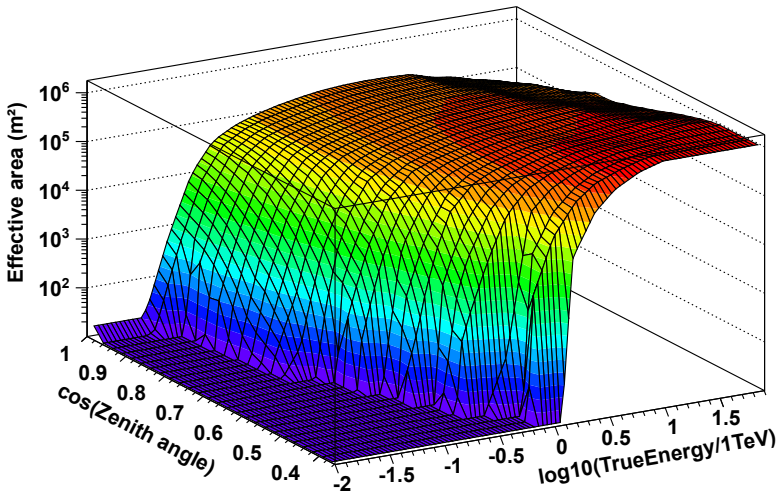

Figure 7.6: Effective area in square meters in function of the cosine of the zenith angle and the logarithm of the energy of the detected event. The values have been obtained from simulations and depend on the analysis chain – here Model++ – and on the cuts applied to the discriminant variables – here ShowerGoodness.

7.2 Maximum likelihood analysis

The modified maximum likelihood method developed in the previous chapter (Eq. 6.14) was applied to the flare data to calculate the dispersion parameter τ_n. The energy resolution $D(E, E_{true})$ was assumed to be perfect in the range $[E_{cut}; E_{max}]$; justification and cut values for the fit are given in the next section. Using Monte Carlo generated tables and knowing the evolution of the zenith angle during the night, it is possible to get the effective area $A_{eff}(E,t)$. The likelihood function is as follows (see Chapter 6):

$$\mathcal{L}(\tau_n) = \prod_{i=1}^{n_{ON}} \frac{n_{ON} - \alpha n_{OFF}}{n_{ON}} \cdot \frac{1}{N_{\rm Sig}(\tau_n)} \cdot A_{eff}(E_i, t_i) \Lambda_{\rm Sig}(E_i) F_{\rm Sig}(t_i - \tau_n \cdot E_i^n) \\ + \frac{\alpha n_{OFF}}{n_{ON}} \cdot \frac{1}{N_{\rm Bkg}} \cdot A_{eff}(E_i, t_i) \Lambda_{\rm Bkg}(E_i) F_{\rm Bkg} \tag{7.1}$$

7.2.1 Selection cuts

Owing to the fact that the search for dispersion in the data is very sensitive to the background level, the following cuts were applied on the energy of the reconstructed events. Within the ON dataset, the signal and the background spectra having two different indices ($\Gamma_{\rm Sig} = 4.8$ for the signal and $\Gamma_{\rm Bkg} = 2.5$ for the background) the ratio S/B is expected to decrease with increasing energy. An upper energy cut at $\rm E_{max}$ = 789 GeV was set, corresponding to the last bin with more than 3σ significance in the reconstructed photon spectrum (see differential flux during the flare in Fig. 7.2). It allows to partly get rid of hadrons misidentified as very high energy (TeV) photons. A lower cut on the energy at $\rm E_{min}$ = 300 GeV was used in order to avoid large systematic effects arising from high uncertainties on the H.E.S.S. effective area at lower energies.

The template light curve used in the likelihood fit was built with low energy events (with $E < E_{\rm cut}$), while the high energy events ($E > E_{\rm cut}$) were processed in the calculation of the likelihood to search for potential dispersion. Here $\rm E_{cut}$ was set to $\rm E_{cut}$ = 400 GeV, which is approximately the median energy of the ON event sample.

7.2.2 Determination of the template light curve and spectrum

The kernel density estimate (KDE) of the light curve is not relevant for studying time distribution where the flux level at the beginning and at the end of the light curve is high (more than 10 % of the maximum flux). Hence, here the fit of a binned histogram has been preferred.

In order to preserve the maximum detected variability in the PG 1553+113 flare, the binning of the time distribution was chosen so that at least two adjacent bins of the distribution yield a minimum of 3σ excess with respect to the average value.

Two parameterizations have been tested to fit the arrival time histogram of the total sample, and then obtained with the low energy photons: 1 Gaussian function and a sum of 2 Gaussian functions.

Figure 7.7 shows the different light curve templates obtained by fitting the binned data. The 2 Gaussian fit improves the quality of the fit by 90 % compared to the single Gaussian parameterization. This 2-Gaussian parameterization was kept to determine the light curve template from the low energy sample, shown in Figure 7.8.

The fit of the whole energy distribution (Fig. 7.2) is kept as the spectrum template in the likelihood model.

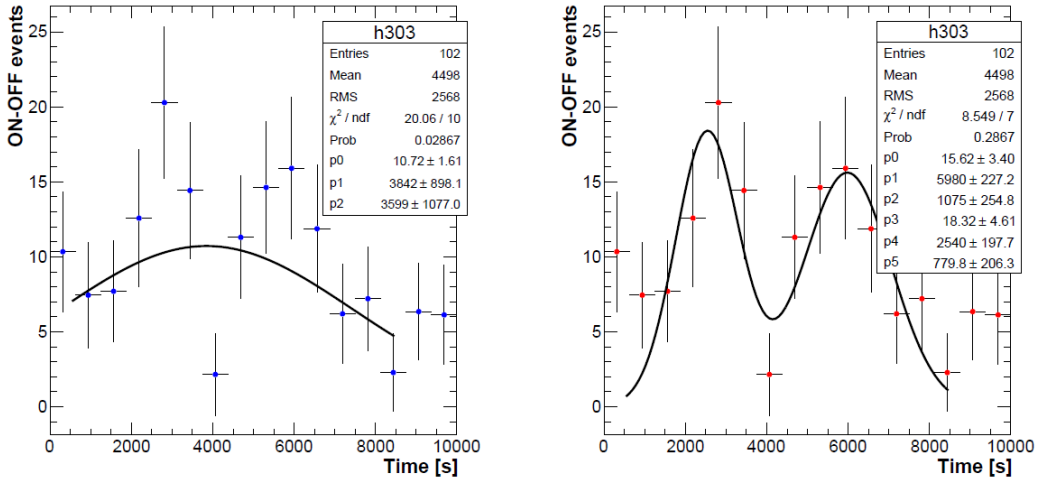

Figure 7.7: Two possible parameterizations of the arrival time distribution (all energies). The vertical bars correspond to $1\,\sigma$ statistical errors, the horizontal bars correspond to the bin width in time. The best fit is superimposed on the histogram.

7.2.3 Production of simulated sets with a Monte Carlo procedure

The method was tested on Monte Carlo (MC) simulated sets. Each set was composed of $n_{ON} = 72$ ON events, as in the real data sample:

— $s = 50$ signal events (with index i) were simulated following this procedure:

1. arrival times t_i were simulated from the template light curve (fig. 7.8), and then shifted by a factor $\tau_{n,\mathrm{inj}} \cdot \mathrm{E}_i$: $t'_i = t_i + \tau_{n,\mathrm{inj}} \cdot \mathrm{E}_i^n$;
2. a zenith angle is associated to the time t'_i, following the curve in Figure 7.4;
3. an off-axis angle is drawn from the distribution given in Figure 7.5;
4. the knowledge of the zenith and the off-axis angles, along with the optical efficiency (fixed to 0.6) allows to compute the effective area, as a function of the true energy $A_i(E_{\mathrm{true}})$;
5. energies E_i follow a power-law spectrum of photon index $\Gamma = 4.85$, degraded by the acceptance $A_i(E_{\mathrm{true}})$ and convoluted by the energy resolution [2].

— $b = 22$ background events (with index j) were produced in the same way as the signal events, except that the times t_j were drawn from a uniform distribution and were not shifted, since no LIV effect is expected. The background spectrum is a power-law spectrum of index $\Gamma = 2.5$, degraded by the acceptance and convoluted by the energy resolution.

In the following tests, the light curve and spectrum templates were not refitted for each realization: they were kept as the original ones, from data. For this reason, there was no need to simulate OFF sets.

2. For the MC-simulated sets, the true energy E_{true} is smeared by about 10 % to take into account the energy resolution. However, the model in the PDF ignores the non-perfect energy resolution, for calculation efficiency purpose.

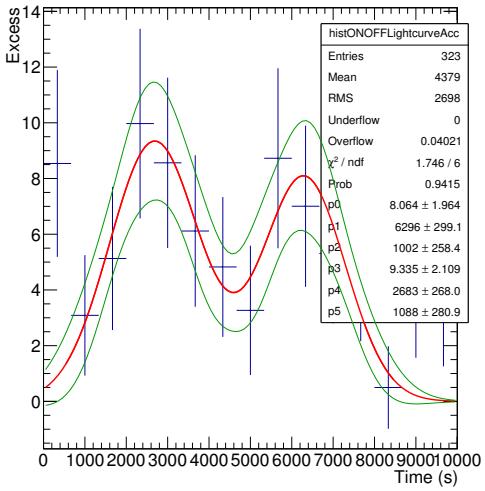

Figure 7.8: Template light curve used in the model, obtained from a fit to the events with $E < E_{cut}$. The vertical bars correspond to 1σ statistical errors; the horizontal bars correspond to the bin width in time. The best fit is plotted in red; the $\pm 1\sigma$ error envelope is shown in green.

7.2.4 Tests of the method on the simulated sets corresponding to the Flare

7.2.4.1 Linearity curve – Coverage

For a given injected dispersion, the maximum likelihood method was applied to each MC-simulated set. The light curve and spectrum templates were not reprocessed for each set: the initial template light curve and energy spectrum were used instead.

The coverage is not necessarily proper, *i.e.* the number of sets for which the injected dispersion value τ_{inj} lies between individual lower limit (LL) and upper limit (UL) does not match the required 95% 1-sided confidence level. In general, the improper coverage is due to poorly controlled systematic effects:

— complex light curve representation (2-Gaussian in this case) and systematic biases in its parameterization;

— asymmetric (non-parabolic) log-likelihood curves;

The common cut used on $-2\Delta \ln \mathcal{L}$ to get the LLs/ULs was iteratively adjusted to ensure a correct statistical coverage: using this new cut, 95 % of realizations provide CIs that include the injected dispersion τ_{inj}. The initial coverage was about 85 % for a cut on $-2\Delta \ln \mathcal{L}$ of 2.71. The new common cut, found iteratively at 3.5, ensures the desired CL.

Figure 7.9 shows the distributions of the best estimates, the 95% 1-sided LLs and ULs for $\tau_{1,\text{injected}} = 0$ s/TeV (linear case) and $\tau_{2,\text{injected}} = 0$ s TeV^{-2} (quadratic case); the means of the lower and upper limit distributions, shown with a blue vertical line, will be used to construct the "calibrated confidence interval", see section 7.2.5. The three distributions are all well described with a Gaussian parameterization. The distributions of the best fitted value present a systematic shift: ~ 100 s TeV^{-1} for the linear case, ~ 200 s TeV^{-2} for the quadratic case.

Figure 7.10 shows the means of the reconstructed dispersion *versus* the real (injected) dispersion for n = 1. For a given injected dispersion, errors bars correspond to the RMS of the distribution of the best estimates $\hat{\tau_n}$. A linear fit is done on the graph (blue line). The slope roughly corresponds to the percentage of signal in the total ON dataset. It is due to the loss of sensitivity resulting from the part of the datasets with no dispersion. In the case of no back-

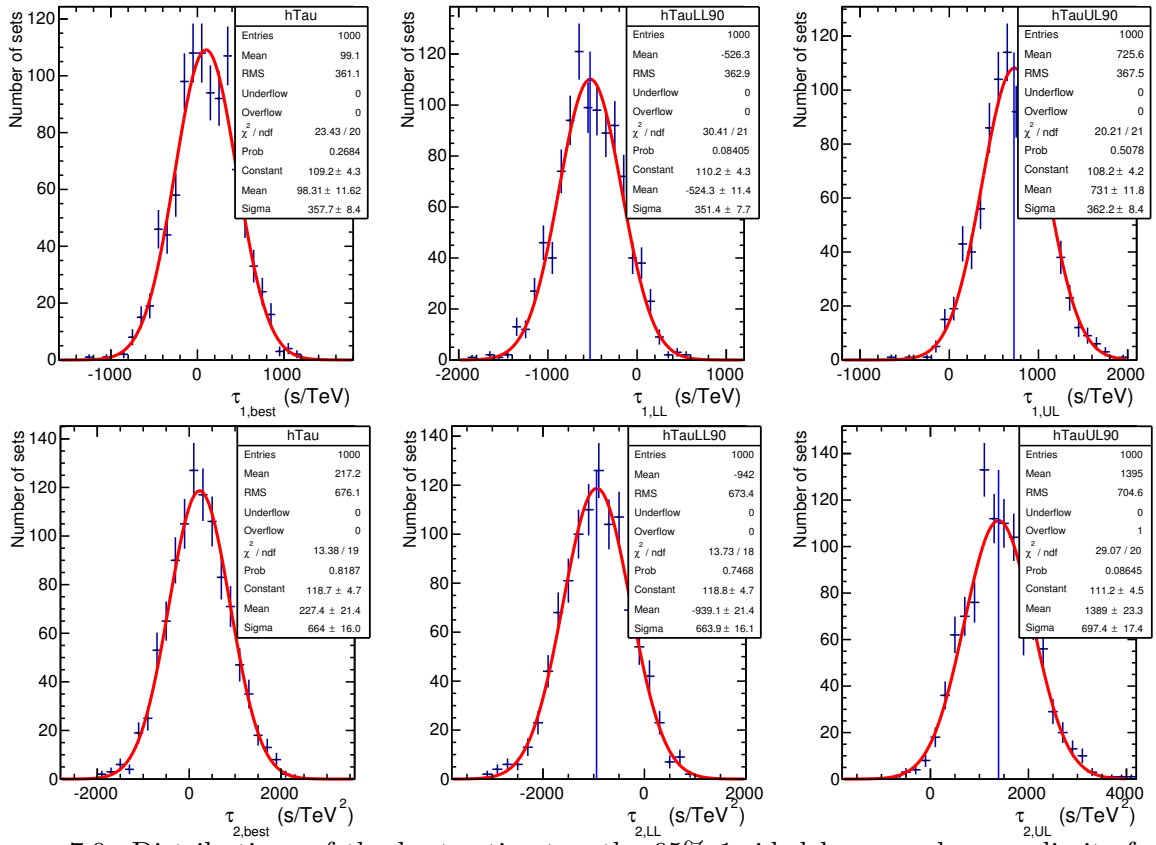

Figure 7.9: Distributions of the best estimates, the 95% 1-sided lower and upper limits from simulations in case of no injected dispersion ($\tau_{\text{injected}} = 0$ s/TeV^n), for n = 1 (top) and n = 2 (bottom); dispersion values are in s/TeV^n. The blue vertical line on the LL (resp. UL) distribution shows LL_{MC} (resp. UL_{MC}), defined as the mean of the distribution.

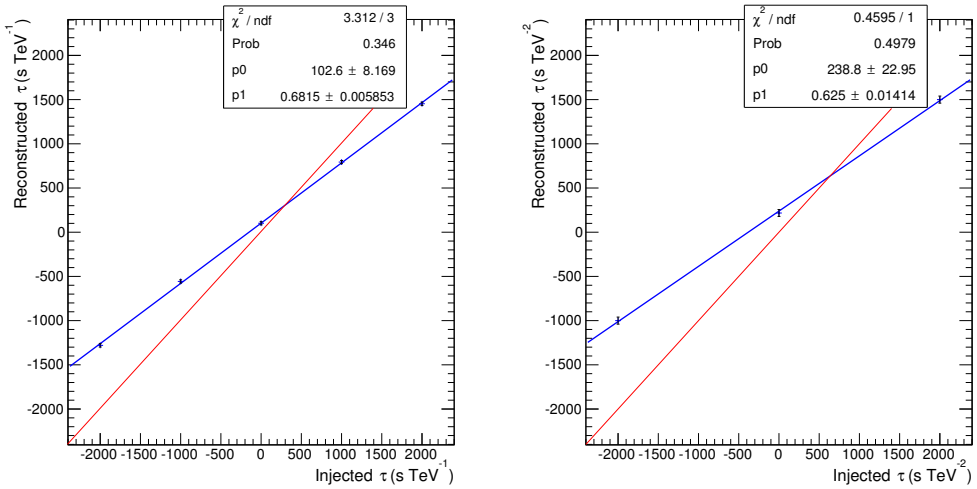

Figure 7.10: Means of the reconstructed dispersion *versus* the real (injected) dispersion for the linear case (n = 1, left); and the quadratic case (n = 2, right); for a given injected dispersion, errors bars correspond to the means of the distribution of the upper and lower limits (90 % 2-sided $\simeq$ 95 % 1-sided). The blue line is a linear fit to the points. The red line shows the ideal curve $\tau_{\text{reconstructed}} = \tau_{\text{injected}}$ obtained in the case S/B $\to \infty$.

ground contamination (*i.e.* ON dataset composed of signal events only), it has been checked that the curve is linear and follows $\tau_{\text{recontructed}} = \tau_{\text{injected}}$ (red line). Also, a systematic shift is observed of about 100 s/TeV, well below 1σ value – the RMS of the best estimate distribution is of ~ 360 s/TeV. The results which will be shown were not corrected for this bias. A way of accounting for this would be to subtract the value of the shift in the best estimate obtained on data. Instead, this shift was included as a systematic uncertainty (see Table 7.3).

7.2.4.2 Impact of the maximum energy cut

The likelihood method was applied on the sets with different maximum energy cut E_{max}. Figure 7.11 shows the means of the best reconstructed dispersion parameter τ_1 as a function of the maximum energy of the simulated events. The error bars correspond to the mean of the per-set 90% 2-sided confidence intervals. To obtain the results for each E_{max}, 1000 sets were simulated through the toy Monte Carlo procedure described in Section 7.2.3.

For a cut energy E_{max} above a few TeV, the sensitivity is somehow stable. However, for a cut below 10 TeV, the confidence intervals start broadening, up to 8 times larger for $E_{max} = 500$ GeV.

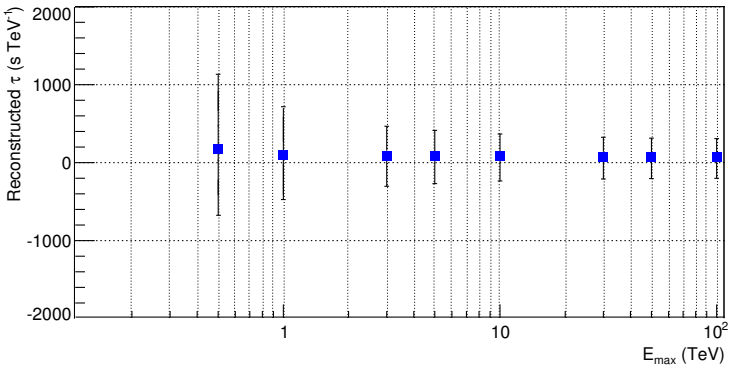

Figure 7.11: Means of the best reconstructed dispersion parameter τ_1 versus the maximum energy of the simulated events. The error bars correspond to the mean of the per-set 90% 2-sided confidence intervals. 1000 sets were simulated through a toy Monte Carlo procedure to obtain the results. This is compatible with the results from the data sample ($E_{max} \sim 800$ GeV).

7.2.5 Results: confidence intervals on the dispersion parameter τ_n

The modified maximum likelihood method was applied on the original dataset and gives a best estimate τ_{best}^{data}. The corresponding likelihood profiles are shown in fig. 7.12. The cut value determined from the simulations to ensure proper coverage was applied on the original dataset to obtain LL^{data} and UL^{data}.

"Calibrated" confidence intervals were also obtained from a combination of data and MC results. The "calibrated" limits LL^{calib} and UL^{calib}, combining τ_{best}^{data} from data together with MC results, were taken as

$$\begin{aligned} LL^{calib} &= LL^{MC} + (\tau_{best}^{data} - \tau_{best}^{MC}) \\ UL^{calib} &= UL^{MC} + (\tau_{best}^{data} - \tau_{best}^{MC}) \end{aligned} \tag{7.2}$$

with τ_{best}^{MC}, LL_{MC} and UL_{MC} defined as the mean of the per-set best-estimate distribution, LL distribution, UL distribution respectively.

The intervals $|\tau_{best}^{MC} - LL^{MC}|$ and $|\tau_{best}^{MC} - UL^{MC}|$ are strongly related to the data as all modeling in the MC simulations comes from the data: light curve, spectrum, numbers of signal and background events. The calibrated CIs are even more strongly connected to the actual measurement as they are shifted to be centered around the best estimate from the data τ_{best}^{data}.

Table 7.2 presents CIs (LLs and ULs) determined from data-only and from calibrated sets: LL_n^{data} and LL_n^{calib} (resp. UL_n^{data} and UL_n^{calib}) are compatible within 10 %, well below the systematic effects related to this measurement (see Table 7.3).

The calibrated CIs were used to derive the final lower limits on E_{QG}. They were preferred over data-only CIs as they take into account the statistical probability to obtain a given result. Moreover, the way the results were extracted ensures coherent comparison with previous published results, e.g. with PKS 2155–304 [14] and GRB studies [71].

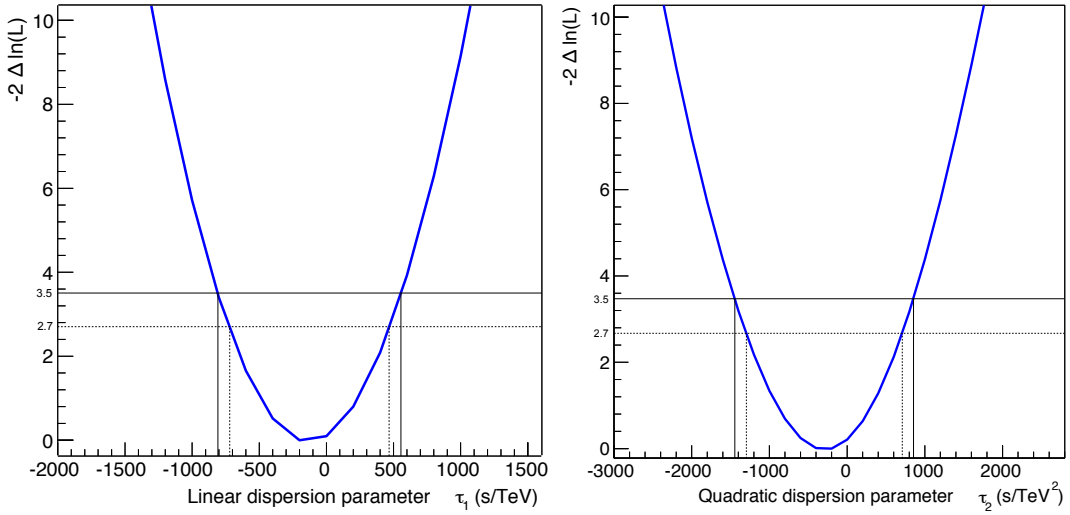

Figure 7.12: $-2\Delta\ln(L)$ as a function of τ_n for a linear (left) and quadratic (right) dependence of the speed of light on energy. The CIs obtained from cuts on $-2\Delta\ln\mathcal{L}$ are shown with the black lines: dashed lines correspond to a cut at 2.7 on the log-likelihood curve; full lines correspond to the new cut at 3.5, determined from MC simulations to ensure a proper coverage for a 90% 1-sided CL.

n	$\tau_{n,best}^{data}$	LL_n^{data}	UL_n^{data}	$\tau_{n,best}^{MC}$	LL_n^{MC}	UL_n^{MC}	LL_n^{calib}	UL_n^{calib}	$LL_n^{calib+syst}$	$UL_n^{calib+syst}$
1	-131.7	-806.7	554.7	99.1	-526.3	725.6	-757.1	494.8	-799.8	537.4
2	-287.5	-1449.9	853.6	217.2	-942.0	1395.0	-1446.7	890.3	-1530.9	973.4

Table 7.2: Linear (top) and quadratic (bottom) dispersion parameter; from left to right: best estimate, LL and UL from data (cut on likelihood curve), LL and UL from MC simulations (means of per-set LL and UL distributions), calibrated LL and UL (combination of data and MC), calibrated LL and UL including systematic errors. Dispersion parameters $\tau_{n,best}$, LLs and ULs are in $\mathrm{s\,TeV}^{-n}$.

7.2.6 Systematics

Estimations of the systematic effects on the dispersion measurement were performed. It was found that the main systematic errors are due to the uncertainties on the light curve parameterization. Other sources of systematic errors include the contribution of the background, the dependence on photon index of the signal spectrum, the energy resolution and the determination of the effective area.

To study the following four contributions, new simulated sets have been built, each one with different input parameters:

— background contribution: photons and background events have been reallocated within the ON dataset in the fit range $[E_{cut}; E_{max}]$, introducing a 1σ fluctuation in the number of signal event n_S in the ON dataset;

— effective area: set to a constant, equal to 120000 m^2 for all energies and all times, which corresponds to a maximum shift of 10 %; the actual effective area increases with energy;

— energy resolution: reconstructed energies have been replaced by the true energies; this corresponds to a shift of about 10 % on the reconstructed energy values;

— photon index: changed by one standard deviation (± 0.25).

For the determination of systematic errors arising from the light curve parameterization, the calibration of the confidence intervals has been redone using successively the upper 1σ and the lower 1σ contours of the template.

The change in mean lower and upper limits on the dispersion parameter τ_n gives an estimation of the systematic error associated to each contribution. An additional systematic contribution comes from the shift arising from the method found with simulation (see 7.2.4.1). Table 7.3 summarizes all studied systematic contributions. The overall estimated systematic error on τ_n is 235 $s\,TeV^{-1}$ for the linear case (n = 1) and 450 $s\,TeV^{-2}$ for the quadratic case (n = 2); they were included in the calculation of the limits on E_{QG} by adding the statistical and the systematic errors in quadrature.

	Estimated error on input parameters	τ_1 ($s\,TeV^{-1}$)	τ_2 ($s\,TeV^{-2}$)
Background contribution	NA	< 45	< 80
Acceptance factors	10%	< 1	< 1
Energy resolution	10%	< 55	< 85
Photon index	5%	< 55	< 50
Lightcurve parameterization	NA	< 200	< 380
Systematic bias	NA	~ 100	~ 200
Total: $\sqrt{\sum_i \text{syst}_i^2}$		< 235	< 450

Table 7.3: Systematic uncertainties.

7.2.7 Results: limits on E_{QG}

Limits on the dispersion τ_n using the quadratic sum of statistical errors from simulations and the systematic errors determined from data and simulations were computed, leading to limits on the energy scale E_{QG} by using Eq. 7.3:

$$\tau_n = \frac{\Delta t}{\Delta(E^n)} \simeq s_{\pm}\frac{(1+n)}{E^n_{QG}2H_0}\kappa_n \tag{7.3}$$

The normalized distance κ_n is calculated from the redshift of the source z, and the cosmological parameters Ω_m, Ω_Λ:

$$\kappa_n = \int_0^z \frac{(1+z')^n\, dz'}{\sqrt{\Omega_m(1+z')^3+\Omega_\Lambda}} \tag{7.4}$$

Choosing the value of $z = 0.48$ determined in [73] and assuming a ΛCDM cosmological model with $H_0 = 70.4 \pm 1.4$ km.s^{-1}.Mpc^{-1}, $\Omega_m = 0.24 \pm 0.02$, $\Omega_\Lambda = 0.73 \pm 0.03$ from WMAP [78], the distance κ_n for n = 1 and 2 is $\kappa_1 = 0.529$ and $\kappa_2 = 0.659$.

The 95% 1-sided lower limits for the subluminal case (s = +1) are: $E_{QG,1} > 4.32 \times 10^{17}$ GeV and $E_{QG,2} > 2.11 \times 10^{10}$ GeV for linear and quadratic LIV effects, respectively. For the superluminal case (s = –1) similar limits are: $E_{QG,1} > 2.90 \times 10^{17}$ GeV and $E_{QG,2} > 1.68 \times 10^{10}$ GeV for the two cases. The symmetry of the results between sub- and superluminal cases can be related to the symmetry of the light curve and to the regularity of the log-likelihood curve, which is almost a quadratic function of τ_n.

7.3 Conclusion

Compared to previous flares from AGNs, the PG 1553+113 flare provided a statistically modest sample of events in the ON region, with an important background contribution. However, it is one of the farthest blazar detected in the VHE range, and allows to probe LIV effects in a redshift region so far uncovered.

Fig. 7.13 shows a comparison of the different lower limits on $E_{QG,1}$ and $E_{QG,2}$ for the subluminal case (s = +1) obtained with AGNs at different redshifts studied at very high energy. All these limits, including the present work, were obtained under the assumption that no intrinsic delays depending on the energy occur at the source [3]. The most constraining limits on E_{QG} with AGNs so far have been obtained by [14] with a likelihood method on PKS 2155-304 data observed with H.E.S.S.: $E_{QG,1} > 2.1 \times 10^{18}$ GeV and $E_{QG,2} > 6.4 \times 10^{10}$ GeV for linear and quadratic LIV effects, respectively (95% CL, 1-sided). Compared to the limits on PKS 2155-304, the limits on the linear dispersion for PG 1553+113 are one order of magnitude less constraining but the limits on the quadratic dispersion are of the same order of magnitude.

The presented analysis, subject to such a high background level and statistical limitations, opens a new window for future LIV studies in a new redshift range, in particular for upcoming population studies, with the updated H.E.S.S. array, completed by a fifth telescope (28m) in its center ("H.E.S.S.-2") and with the future array of Cherenkov telescopes, CTA.

3. A spectral variability at the source could indeed mimic a dispersion and could thus enhance or counterbalance dispersion arising from the possible LIV effects probed in this work.

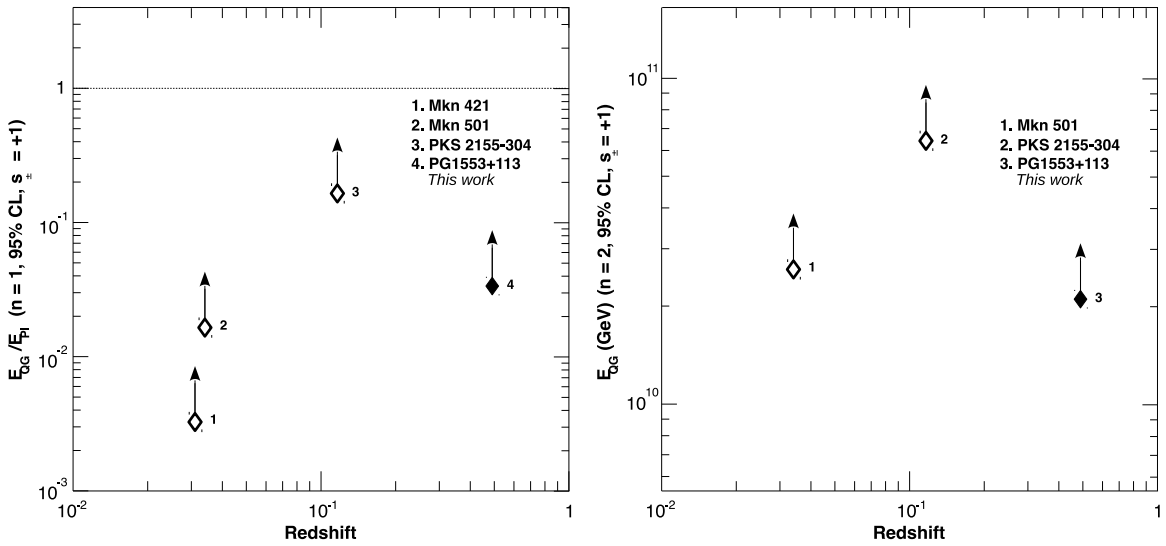

Figure 7.13: Lower limits on $E_{QG,1}$ (left) from linear dispersion and on $E_{QG,2}$ (right) from quadratic dispersion for the subluminal case (s = +1) obtained with AGNs as a function of the redshift. The limits are given in terms of Planck energy E_{Pl}. The constraints from Mkn 421 have been obtained in [79], from Mkn 501 in [69], and from PKS 2155-304 in [14].

Chapter 8

Constraints on Lorentz Invariance Violation from the data of four Gamma-Ray Bursts observed with *Fermi*-LAT

Contents

Introduction

As explained in Chapter 2, GRBs are short and bright astrophysical events observed at a redshift of up to 8: these are the brightest events observed in the HE range (< 100 GeV). Their light curves show one or more peaks, followed by an afterglow. These bursts last from a few milliseconds to a few minutes.

In the first three years of operation, *Fermi* has detected 21 GRBs emitting above 1 GeV and 10 GRBs for which the redshift has been measured (z between 0.74 and 4.35). We have selected four of the 21 GRBs for their remarkable characteristics: the short duration of the main peak, their distance, and their emission in the GeV range. Contrary to the data of PG 1553+113, detected with H.E.S.S., the GRB samples from *Fermi*-LAT are pure (almost no background contribution [1]) and present a fast variability. They have however a lower energy range (tens of MeV to tens of GeV) compared to AGNs observed with a ground-based telescope (above 100 GeV).

In this chapter, the results obtained with the likelihood method applied to the data of these four bright *Fermi*-LAT GBRs will be detailed; the results obtained with two other methods will be presented as well. These results have led to a *Fermi* (type 2) publication [71].

8.1 Data samples – selections

Only the LAT events were considered in the analysis for we wanted to focus on a unique spectral component. The event selection P7_TRANSIENT_V6 was used; it is a less restrictive selection of LAT events optimized for signal-limited analyses such as this one.

Four bursts were analyzed; their main characteristics are summarized in Table 8.1. Corresponding times and energies are provided in the scatter plots of Figure 8.1. These plots allow to see the main features of the studied GRBs. Most of the four bursts present a rather sharp peak, followed by a tail. Two bursts, GRB 090902B and GRB 090926A seem to have secondary peaks. One burst, GRB 090510 is particularly short (peak duration $\lesssim 1$ s); the three other last longer. With its sharp peak and its shorter duration, we can expect tighter constraints on the dispersion parameter from GRB 090510.

Three bursts have photons with energies above 10 GeV: GRB 080916C (13.3 GeV at 16.5 s), GRB 090510 (30.9 GeV at 0.8 s) and GRB 090902B (11.2 GeV at 11.7 s, 10.1 GeV at 42.4 s, 13.2 GeV at 45.6 s, and 33.1 GeV at 81.7 s). For the latter, only the first 10+ GeV photon is actually shown on the plot as it is included in the time range for the analysis, determined as explained in subsection 8.1.3. The knowledge of the maximum energies gives a clue of the precision of the expected results: the higher the maximum energy, the more precise the results.

GRB name	z	Total stat in LAT above 20 MeV	E_{max} (GeV)	Burst duration (s)
GRB 080916C	4.35	256	13.3	~ 30
GRB 090510	0.903	433	30.9	~ 10
GRB 090902B	1.822	403	33.1	~ 80
GRB 090926A	2.1071	384	3.2	~ 25

Table 8.1: Characteristics of the studied GRBs samples.

1. contamination of the order of 10^{-1} Hz above 0.1 GeV and 10^{-3} Hz above 1 GeV

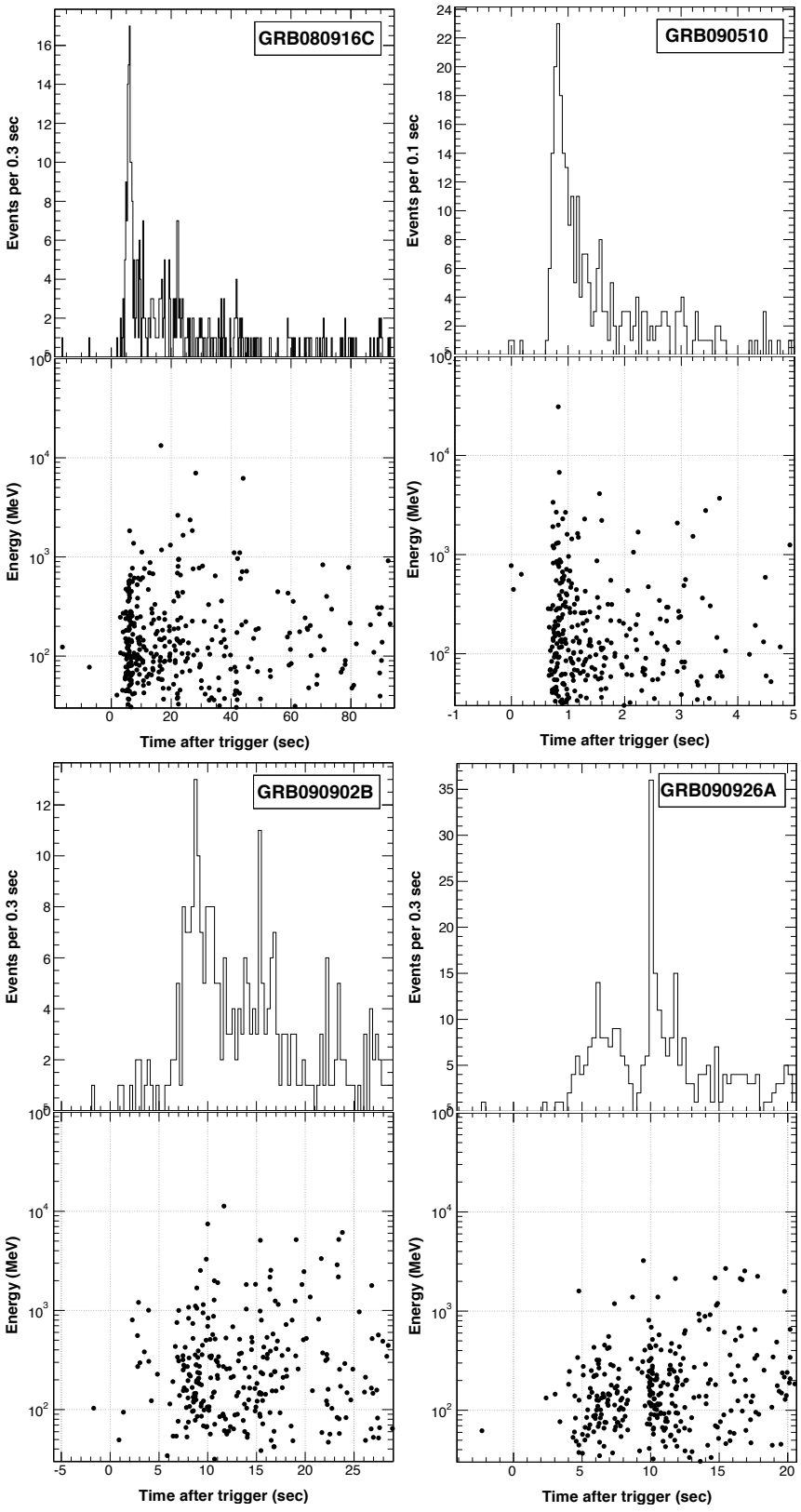

Figure 8.1: Time and energy profiles of the detected events from the four GRB samples. Each pair shows a light curve (top) and an event energy versus time scatter plot (bottom). Note that these plots do not show the full time ranges of the bursts, but focus instead around the interval used for the current analysis.

8.1.1 Energy selection

Events with energy below 30 MeV were rejected because of their low angular resolution. No maximum cut was applied, except for GRB 080916C for which an event of energy 106 GeV was removed: it had been shown by the *Fermi* collaboration that this event is a mis-reconstructed hadron [80]. It would anyway not be included in the analysis as it is outside the time interval determined in subsection 8.1.3.

8.1.2 Angular selection

An angular cut was chosen for each sample so as to include 95% of the events detected by the LAT. As the PSF depends on the energy of the event and on the off-axis angle, the angular cut is different for each event: an event is kept if its reconstructed position is included in the 95% containment radius. The PSF worsens (*i.e.* gets wider and wider) at low energies, so the containment radius increases as well: in order not to include all the events in the field of view at low energies, a maximum angular cut of 12° was set.

8.1.3 Time interval

To minimize systematic effects due to GRB spectral evolution (a known property of the GRB emission, cf. Chapter 2), the time intervals were chosen around the main peaks of emission. They were then extended to prevent photons initially in the peak to be found outside after propagation, due to LIV effects. For the calculation of individual photon delays, we assumed $E_{QG} = 0.5\ E_{Planck}$ for the linear case, and $E_{QG} = 1.5 \times 10^{10}$ GeV for the quadratic case; these values are about half of the E_{QG} limits previously obtained by *Fermi* [81].

Additional cuts were made for the PV and SMM methods and are discussed thereafter.

GRB	Time Range (s)		E_{cut} (MeV)	Γ	n_{fit}	
	$n=1$	$n=2$	$n=\{1,2\}$	$n=\{1,2\}$	n = 1	n = 2
080916C	3.53–7.89	3.53–7.80	100	2.2	59	59
090510	-0.01–3.11	-0.01–4.82	150	1.5	118	125
090902B	5.79–14.22	5.79–14.21	150	1.9	87	87
090926A	8.92–10.77	9.3–10.76	120	2.2	48	46

Table 8.2: Configuration details for ML-Gaus and ML-KDE. Γ is the photon index of the spectrum of detected events assuming the energy distribution follows a power-law ($\propto E^{-\Gamma}$). E_{cut} is the separating energy between the low-energy events used for building the light curve template and the n_{fit} high-energy events used in the calculation of the likelihood.

8.2 Maximum likelihood analysis

The modified maximum likelihood method developed in chapter 6 was applied to the data of the four GRBs to calculate the dispersion parameter τ_n for each of them.

8.2.1 Maximum likelihood methods: Formalism and assumptions

The identification power of *Fermi*-LAT allowed to consider the datasets free of any background contribution. Thus the maximum likelihood method *in case of no background contamination* presented in chapter 6 (Eq. 6.3) was applied to the data of the four GRBs to calculate the dispersion parameter τ_n. The energy resolution $D(E, E_{true})$ was assumed to be perfect in the range $[E_{\rm cut}; E_{\rm max}]$. The dependence of the effective area on the energy has been neglected: the fit was indeed performed in a range where the acceptance is almost constant (maximum variation of 5 %).

The likelihood function is as follows:

$$\mathcal{L}(\tau_n) = \prod_{i=1}^{n_{\rm fit}} \frac{1}{N(\tau_n)} \cdot \Lambda(E_i) F(t_i - \tau_n \cdot E_i^n) \tag{8.1}$$

where $n_{\rm fit} = n_{\rm ON}$ is the number of high energy events processed in the fit [2].

The emission time distribution of the photons F is determined from a parametrization of the observed light curve at low energies and is evaluated on $t - \tau_n \cdot E^n$ to take into account the delay due to possible LIV effect. Λ is the measured signal spectrum. $N(\tau_n)$ is a normalization factor in the (E, t) range of the likelihood fit.

A separation energy $\rm E_{cut}$ was chosen for each dataset to approximately correspond to the median energy of the sample. While the template light curves used within the likelihood model were built with the low energy events (with $E < E_{\rm cut}$), the high energy events ($E > E_{\rm cut}$) were processed in the calculation of the likelihood to search for potential dispersion. Table 8.2 summarizes the configuration parameters for each GRB dataset, including the separating energies $\rm E_{cut}$, and the number of events $n_{\rm fit}$ processed in the likelihood fit. The derivation of two different light curve templates (parameterization and kernel estimation) are detailed in the next paragraph.

We assumed that the data of the studied GRBs show no spectral variability, *i.e.* the energy spectra do not evolve with time. It was fitted by a power-law function to get the spectrum templates in the likelihood model. Spectrum templates are shown in Figure 8.2 for each GRB. Table 8.2 also shows the photon index of the fitted power law spectra, assuming the energy distribution follows a power-law ($\propto E^{-\Gamma}$). The energy spectrum of GRB 090510 is remarkably hard, with a photon index of 1.5.

2. There was no reason to keep the notations $\rm n_{ON}$ and $\rm n_{OFF}$ as no subtraction method is used here.

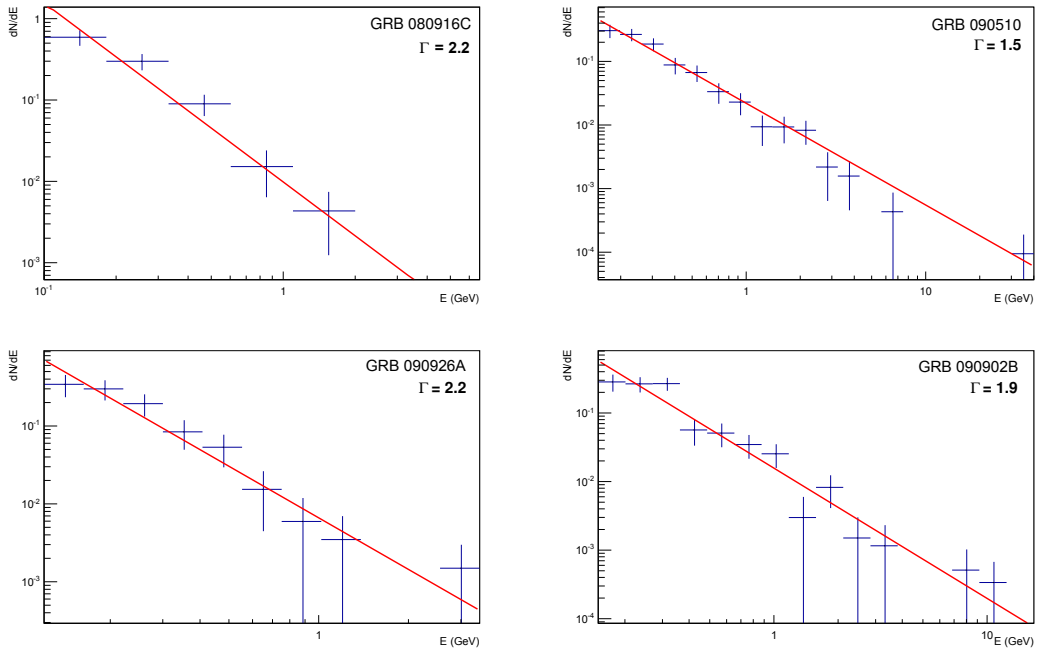

Figure 8.2: Spectrum template, parameterized with a power-law function. Γ denotes the photon index of the assumed power-law spectrum.

8.2.2 Template light curves

The templates were determined from the low energy events included in the time range defined in previous section. Two templates were studied: parameterization with a sum of Gaussian functions and kernel estimation with a Gaussian kernel. The application of the ML method with a Gaussian (resp. kernel estimated) template will be referred to as ML-Gaus (resp. ML-KDE).

8.2.2.1 ML-Gaus

For each burst, a reasonable binning was chosen so as to keep the features such as the peak and the more diffuse component (tail). Other choices of binning were tested and did not introduce serious changes in the fit. To describe the sharp emission *and* the tail, a sum of two Gaussians (three Gaussians for GRB 090510) was used for the fit of the time distribution at low energies.

Figure 8.3 shows the binned distribution (with chosen binning) and the best fit along with the $\pm 1\sigma$ contour for each GRB dataset.

8.2.2.2 ML-KDE

Unlike the data of PG 1553+113, the data of the GRBs is quasi free from background events; besides, the lightcurves are well defined in the sense that they show negligible fluxes at the beginning and at the end of the data-taking: the use of a kernel estimation is suitable. The data is represented by the sum of normalized Gaussians centered on each event time t_i, with a fixed width h^* or different individual widths h_i.

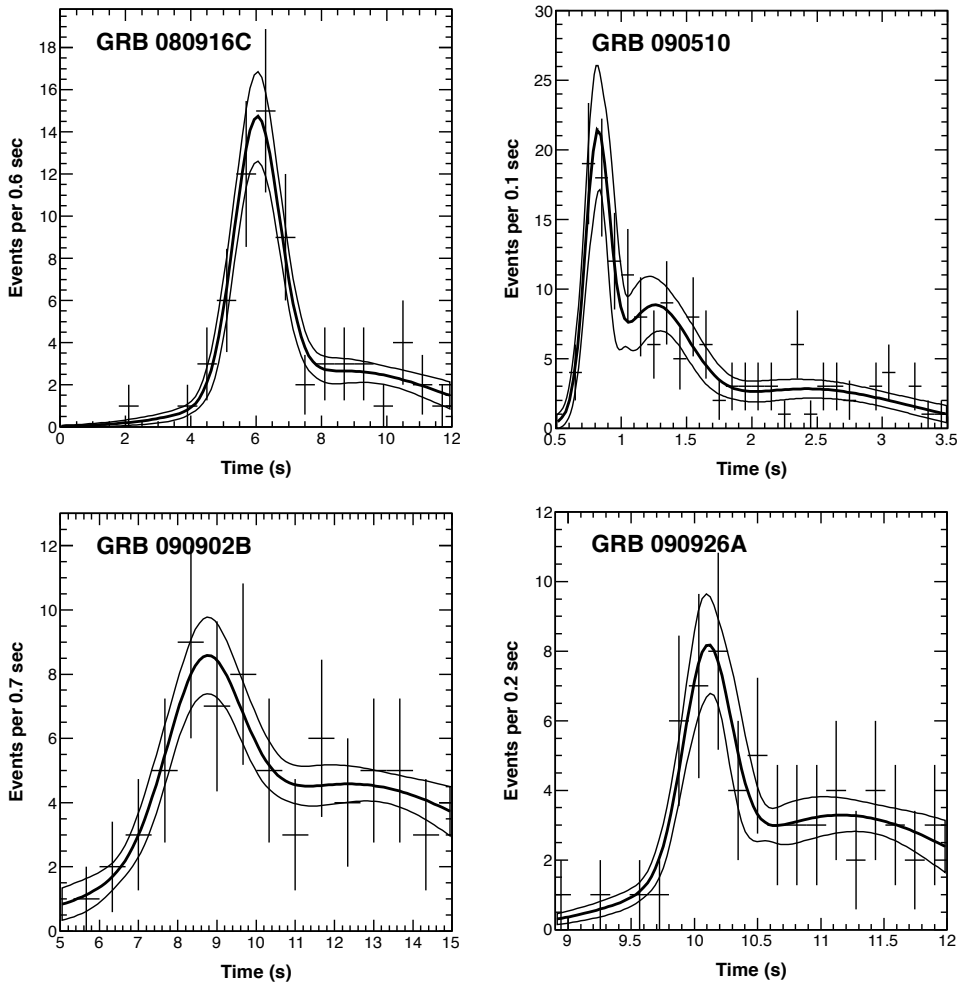

Figure 8.3: Light curve templates: parameterization with a sum of 2 or 3 Gaussians. The thick curve shows the best fit; the thinner curves show the $\pm 1\sigma$ error envelope. The time ranges do not necessarily correspond to the analysis time intervals.

Determining the width of the kernels

Examples of kernel-estimated light curves in these two extreme cases – h^* particularly small or large – are given in Figure 8.4 for GRB 090510. If the kernel is too wide, the variability features of the distribution will be lost. If too tight, tiny fluctuations can get overemphasized and lead to wrong likelihood profiles. Thus the determination of the width h^* of the kernels is crucial for a proper shape of the light curve template.

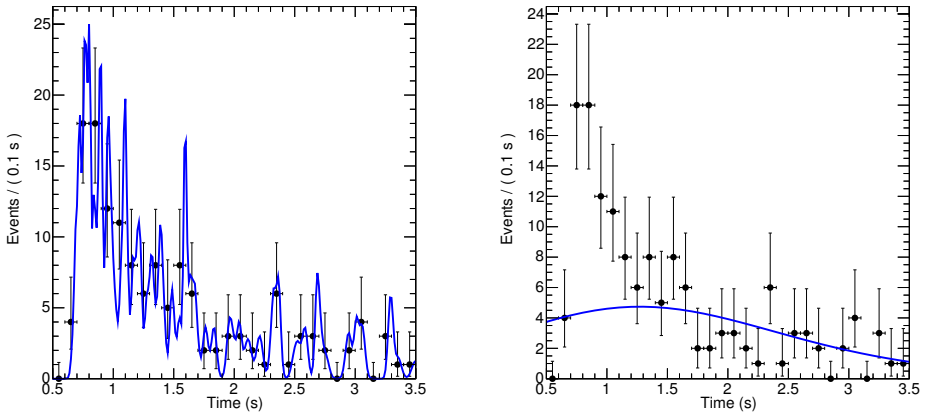

Figure 8.4: Examples of kernel-estimated light curves in two extreme cases – h^* particularly small (left) or large (right) – for GRB 090510.

The width could be optimized on simulated datasets so as to maximize the sensitivity of the method. However, as we used the MC simulations to get CIs (see section 8.2.4), optimizing the width on similar MC dataset did not seem safe. We instead chose automated procedures to calculate h^* (see Appendix B). Ultimately the initial width h^* was taken as

$$h^* = \left(\frac{4\hat{\sigma}^5}{3n}\right)^{\frac{1}{5}} \approx 1.06\hat{\sigma}n^{-1/5}$$

with $\hat{\sigma}$ the standard deviation of the distribution and n the number of low energy events events. This initial width h^* was adaptively reprocessed ("adaptive kernels"), allowing to get wider width in low-density regions. It was a good balance between having a fast code (the template light curve is built from every simulated dataset) and an acceptable calculation of the width of the kernel.

KDE templates are shown in Figure 8.5. It reproduces well the features of the data, the peak and the tail. *One* possible Gaussian template is superimposed: the two methods, fit and kernels, lead to similar light curve templates; the kernel template has however a wider peak for two bursts (GRB 090510 and GRB 090926A).

Notice that the time interval for the determination of the template was slightly different from the time ranges determined in section 8.1.3:

— we wanted to get the same template for n = 1 and n = 2; we thus took the union of the two time ranges;

— also, for the kernel-estimated templates, the time intervals were extended a bit so as not to underestimate the edges of the distribution.

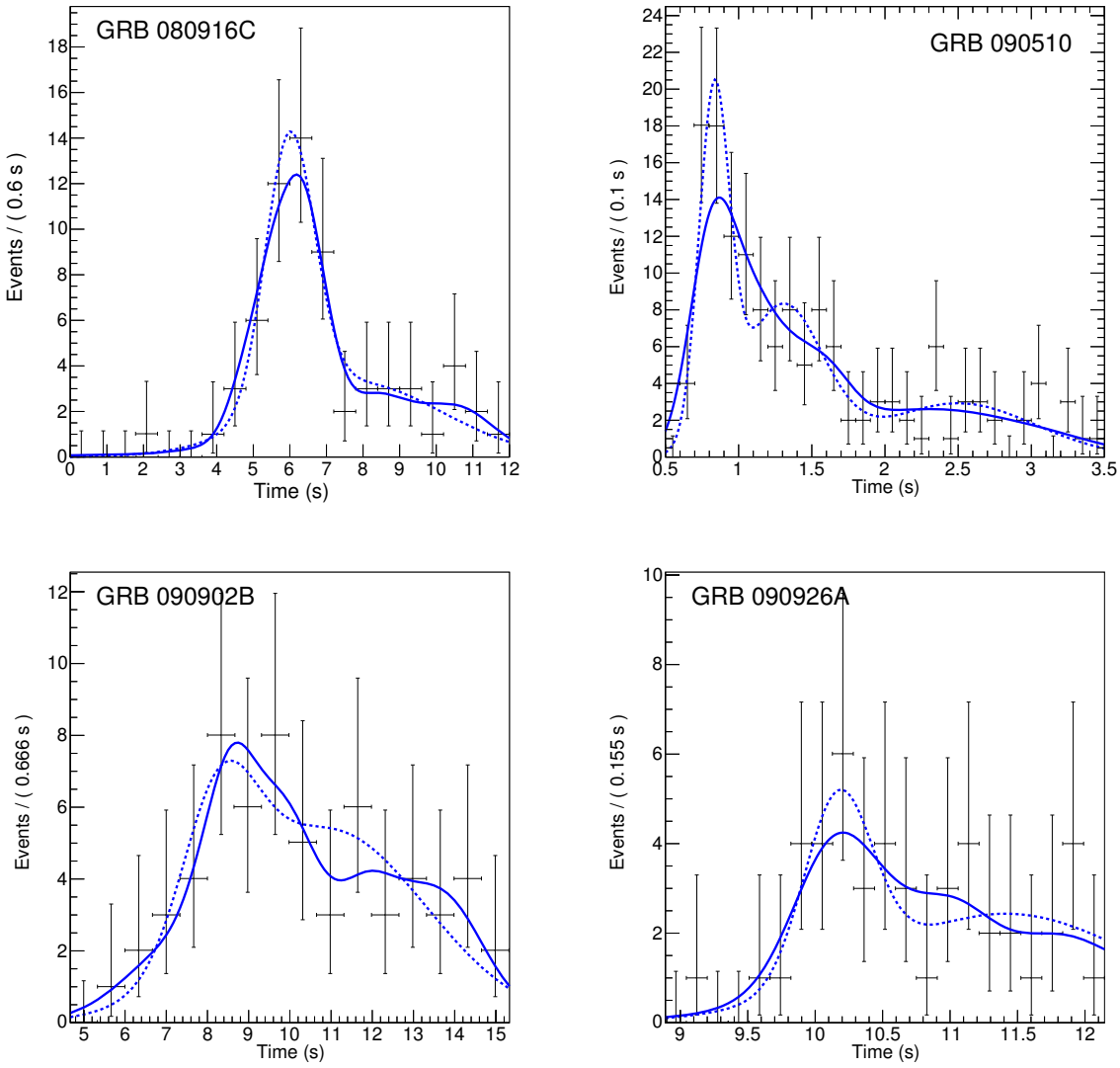

Figure 8.5: Light curve templates: kernel estimation (full line) and *one* possible Gaussian template (dotted line, for comparison). The time ranges, the same as the previous Gaussian templates plots, do not necessarily correspond to the time intervals of the analysis. The binning is not used to get the kernel estimate and is shown here for comparison (binning used to fit the Gaussian functions).

8.2.3 Linearity curves

The following test was performed in order to evaluate the robustness of the method. A few thousand of sets were simulated with artificial injection of a dispersion parameter. These sets have the same statistics, light curve model and spectrum as the original data. For a given injected dispersion, the maximum likelihood method was applied to each MC-simulated set to get a best estimate [3], a lower and an upper limit.

Figure 8.6 shows the linearity curves, *i.e.* the plot of the means of the reconstructed dispersion *vs.* the real (injected) dispersion for the linear case (n = 1), for both sub-methods applied on GRB 090510-like simulated datasets. For a given injected dispersion, errors bars correspond to the means of the distribution of the upper and lower limits (∼95 % 1-sided). The line is a linear fit to the points. For 0 s/GeV, the cuts on the likelihood profiles were set to ensure a proper coverage, *i.e.* the cut on the likelihood profiles is set iteratively so that exactly 90 % of the per-set CIs include the injected dispersion $\tau_{\rm inj}$ [4]. The values of the cuts for the 0 s/GeV case were kept for other injected dispersions.

No significant shift (fit parameter "p0" on the graphs) is observed is either method. The slope (fit parameter "p1") is close to 1 for both methods: this verifies that each method actually reconstructs the injected dispersion. The error bars correspond to the CIs for each given $\tau_{\rm inj}$, *i.e.* the means of the distributions of the lower/upper limits: they tell how precise the method is depending on the actual dispersion within the data. It is related to *this particular analysis* as it takes into account the characteristic features of the current data (shape of the lightcurve, steepness of the energy spectrum, statistics), and the different assumptions made (energy resolution, effective area). Note that for ML-Gaus, the template has not been reprocessed for each realization; refitting the light curve for each realization would entail slightly more spread distributions of the best estimates and lower/upper limits. As it is here, the slope for ML-Gaus (without refit) is closer to 1 and CIs for individual $\tau_{\rm inj}$ are tighter.

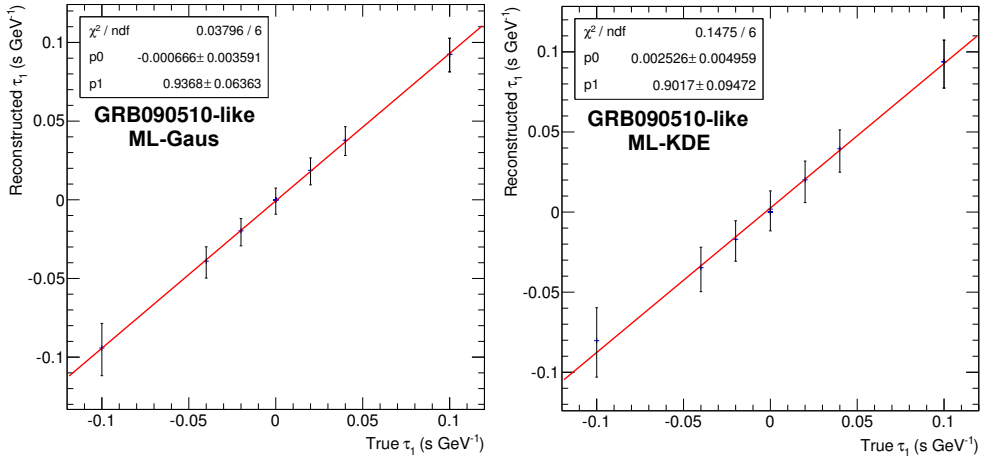

Figure 8.6: Linearity curves, *i.e.* means of the reconstructed dispersion *vs.* the true dispersion for the linear case (n = 1), for ML-Gaus (left) and ML-KDE (right) applied on GRB 090510-like simulated datasets. For a given injected dispersion, errors bars correspond to the means of the distribution of the upper and lower limits (90 % 2-sided). The line is a linear fit to the points.

3. Note: the likelihood profile sometimes presents several minima (1 global minimum + local ones), due to the complex parameterization of the light curve (several Gaussians for ML-Gaus, or fluctuations for ML-KDE). We chose to consider only the global minima as the best estimate.

4. as explained in chapter 6 and as in the analysis of PG 1553+113 in Chapter 7

8.2.4 Results: dispersion parameter

8.2.4.1 Confidence intervals "from data"

The maximum likelihood method was applied on the original dataset with the two different templates, Gaussian parameterization (ML-Gaus) and kernel estimate (ML-KDE). The corresponding likelihood profiles are shown in Figures 8.7 and 8.8. The log-likelihood profiles obtained from the GRB 090510 dataset are much narrower than those obtained from the three other GRB datasets. It is simply explained by the shape of the light curve used in the model: GRB 090510 has the shortest duration and the sharpest peak among the four GRBs.

The minima of the log-likelihood curves give the best estimates τ_{best}^{data}. A cut on $-2\Delta\ln\mathcal{L}$ at 2.7 – corresponding to the 90 % CL quantile of a χ^2 distribution – was applied on the log-likelihood profiles to obtain LL^{data} and UL^{data}. with 95% CL (one-sided).

One can note that the log-likelihood curves do not always follow a proper χ^2 distribution: the irregularities observed in the light curve are transfered to the log-likelihood curve. Thus, the naive cut on the likelihood curve at 2.7 may not give the required 90% 2-sided CL.

Note: the profile likelihood obtained from the application of the ML methods on GRB 090926A data are shifted toward negative values of τ_n: at 90% CL (2-sided), they exclude the value $\tau_n = 0\,\mathrm{s/GeV}^n$. This does not mean that this result is significant. It simply shows that for this GRB, there are extra systematic uncertainties that are above the level of the statistical uncertainties. This could be due to the intrinsic spectral evolution, addressed in section 8.2.5.

8.2.4.2 Calibrated confidence intervals

Confidence intervals were also obtained using Monte Carlo sets simulated as explained in previous paragraph, with zero injected dispersion. Each simulated data set produces:

— a best estimate $\hat{\tau}_n$: as an example, the distributions of the best estimates obtained from the application of ML-Gaus and ML-KDE on the data of GRB 090510, for the linear case, are plotted in Figure 8.9 (plots on the left). The distributions are well described by a Gaussian. Table 8.3 shows these mean values along with the RMS of the best-value distributions for the four GRB datasets. The non zero mean values are smaller than the width of the distributions. The distribution of the best estimates obtained with ML-Gaus and ML-KDE are in remarkable agreement for most of the GRB datasets; they are slightly more spread with ML-KDE. They only differ frankly for GRB 090510, quadratic case: the distribution of $\hat{\tau}_2$ is 7 times larger for ML-KDE. This difference could be explained by the different lightcurve templates used (see Figure 8.5): the main peak of GRB 090510 as determined by the kernel estimation is wider than the one got from a Gaussian fit.

— a lower limit and an upper limit on τ_n from cuts on the likelihood profile. The value of the cut was iteratively set so as to get proper coverage. The middle and left plots of Figure 8.9 shows the distributions of the 90 % two-sided lower and upper limits for GRB 090510-like simulated sets. The distributions are not perfectly Gaussian. This is due to the shape of the light curve templates: the tail start with the main peak but last longer. The blue vertical line on the LL (resp. UL) distribution shows the calibrated lower limit LL_{MC} (resp. upper limit UL_{MC}), defined as the mean of the distribution.

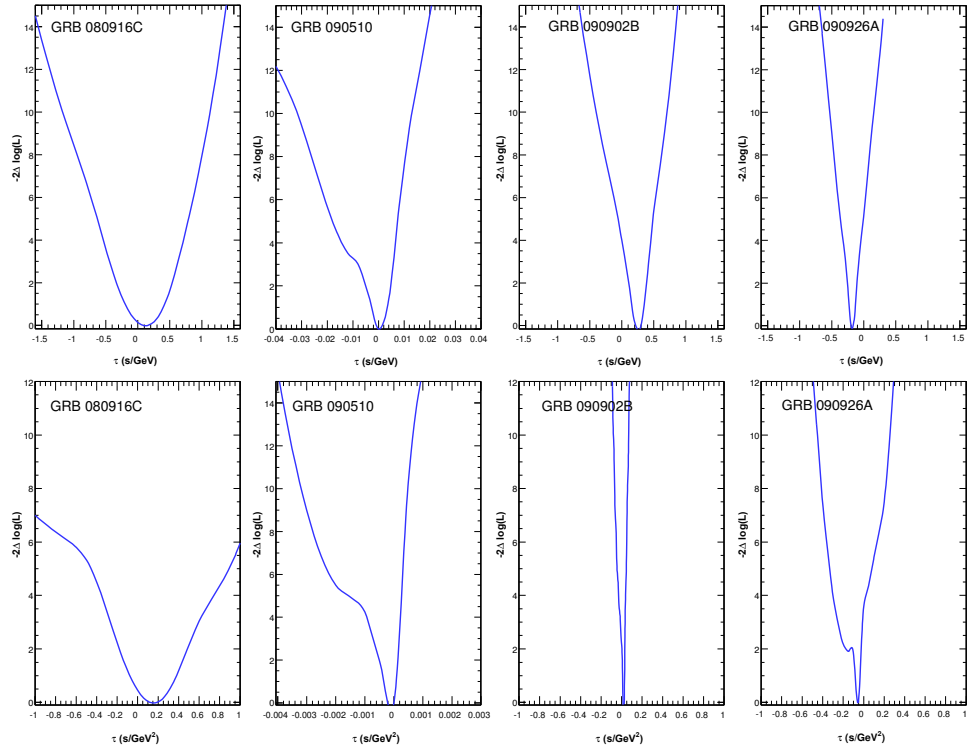

Figure 8.7: Log-likelihood curves from Gaussian functions templates: $-2\Delta\ln(L)$ as a function of τ_n for a linear (top) and quadratic (bottom) dependence of the speed of light on energy.

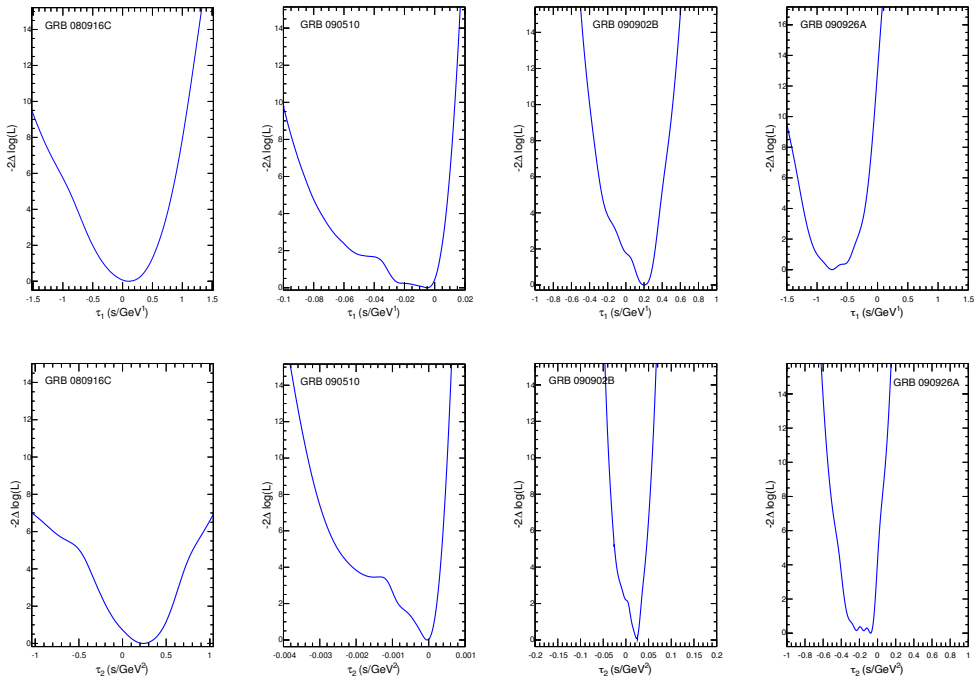

Figure 8.8: Log-likelihood curves from KDE templates: $-2\Delta\ln(L)$ as a function of τ_n for a linear (top) and a quadratic (bottom) dependence of the speed of light on energy.

	ML-Gaus		ML-KDE	
GRB	$< \hat{\tau}_1 >$	$\sigma(\hat{\tau}_1)$	$< \hat{\tau}_1 >$	$\sigma(\hat{\tau}_1)$
080916C	-0.053	0.236	-0.186	0.318
090510	0.00086	0.00357	0.000832	0.00815
090902B	-0.00777	0.141	-0.0687	0.153
090926A	-0.0075	0.161	-0.202	0.238
GRB	$< \hat{\tau}_2 >$	$\sigma(\hat{\tau}_2)$	$< \hat{\tau}_2 >$	$\sigma(\hat{\tau}_2)$
080916C	-0.031	0.21	-0.0648	0.218
090510	0.0000248	0.000109	0.000296	0.000721
090902B	0.00232	0.0176	-0.00682	0.0306
090926A	0.0075	0.134	-0.0612	0.0995

Table 8.3: Mean values and R.M.S. of the distributions of the best estimates of the LIV parameters $\hat{\tau}_n$ obtained from the application of ML-Gaus and ML-KDE on the MC simulations. Values are in s/GeV^n.

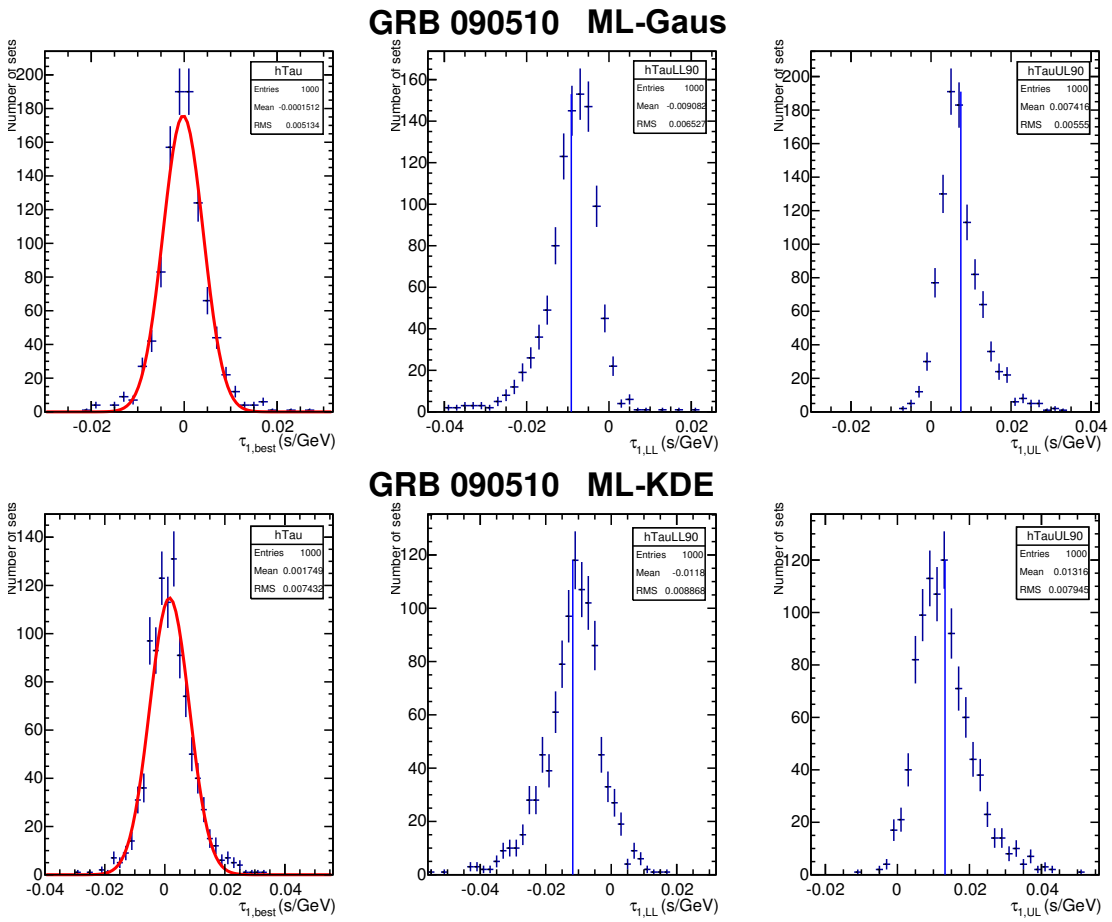

Figure 8.9: Distributions of the best estimates (left), 95 % 1-sided lower limits (center) and upper limits (right) for GRB 090510-like simulated sets, processed with ML-Gaus (top) and ML-KDE (bottom), in case of no injected linear dispersion ($\tau_{\rm inj} = 0\,{\rm s/GeV}^1$). The blue vertical line on the LL (resp. UL) distribution shows LL_{MC} (resp. UL_{MC}), taken as the mean of the distribution.

We shifted the mean lower limit LL^{MC} and the mean upper limit UL^{MC} by the value of τ_{best}^{data} [5] as measured from the actually detected data set, to finally produce the calibrated lower and upper limits:

$$LL^{calib} = LL^{MC} + \tau_{best}^{data} \qquad (8.2)$$
$$UL^{calib} = UL^{MC} + \tau_{best}^{data}.$$

The calibrated CIs were used to derive the final lower limits on E_{QG}. They are preferred over data-retrieved CIs as they take into account the statistical probability to obtain a given result.

Best estimates (from data) and CIs (from data and calibrated CIs) are given in Table 8.4: LL_n^{data} and LL_n^{calib} (resp. UL_n^{data} and UL_n^{calib}) are compatible within 10 %. As noticed before on the distributions of the best estimates $\hat{\tau}_n$, the results from both sub-methods ML-Gaus and ML-KDE agree remarkably well. The differences observed, mainly for GRB 090902B, can be explained by the different shapes of the light curve templates.

Because of the shift of the likelihood profile, the non-calibrated upper limits from GRB 090926A exclude zero; also, the lower limits (linear case) from GRB 090902B exclude or are too close to zero (emphasized). These limits should not be used to constrain E_{QG} as they would lead to either incongruous or suspiciously good limits. However, the corresponding calibrated limits do not exclude zero and are more symmetrical; they will still be used to constrain E_{QG}.

GRB Name	ML-Gaus (data)			ML-Gaus (calibrated)			ML-KDE (data)			ML-KDE (calibrated)		
	(Lower Limit, Best Value, Upper Limit) (s GeV^{-1}) $n=1$											
080916C	-0.41	0.1	0.61	-0.76	–	0.69	-0.60	0.094	0.66	0.63	–	0.56
090510 ($\times 10^3$)	-6.8	1	5.2	-3.2	–	6.8	-64	-4.9	5.6	-13	–	11
090902B	*0.083*	0.25	0.41	-0.19	–	0.59	*-0.086*	0.20	0.34	-0.34	–	0.33
090926A	-0.25	-0.18	*-0.13*	-0.48	–	0.068	-1.2	-0.75	*-0.28*	-0.60	–	0.35
	(Lower Limit, Best Value, Upper Limit) (s GeV^{-2}) $n=2$											
080916C	-0.24	0.12	0.56	-0.73	–	0.69	-0.26	0.24	0.62	-0.32	–	0.27
090510 ($\times 10^3$)	-0.63	-0.1	0.15	-0.11	–	0.13	-1.0	-0.040	0.26	-0.89	–	0.70
090902B ($\times 10^3$)	-5.1	10	33	-61	–	61	-8.5	24	37	-38	–	36
090926A	-0.23	-0.06	*-0.015*	-0.32	–	0.13	-0.39	-0.15	*-0.015*	-0.24	–	0.13

Table 8.4: Results on the linear dispersion parameter τ_1 (in s.GeV^{-1}) and on the quadratic dispersion parameter τ_2 (in s.GeV^{-2}) with the maximum likelihood methods. The limits are for a two-sided 90% CL. The upper limits ("data") from GRB 090926A and one lower limit ("data") from GRB 090902B are emphasized: they should not be used to constrain E_{QG}, as they exclude or are too close to zero, and would lead to either incongruous or suspiciously good limits.

8.2.5 Taking into account possible GRB-intrinsic effects

Previous analyses of *Fermi* GRB data have shown that the emission falls into different spectral components: a Band component at MeV energies, and a power-law component at higher energies (see *e.g.* [32]). The difference in time emission between the two components could be misidentified as a LIV effect. The cuts (E > 100 MeV) used for PV and SMM limit the contribution of Band-originated events. The cuts at a rather low energy (E > 30 MeV) used for the ML method makes it possibly sensitive to this effect. However, a dedicated analysis of the data did not show any sign of time lag between the two spectral components. Also, spectral evolution has been detected in many *Fermi*-LAT GRBs and can be misinterpreted as LIV effect.

5. while for PG 1553+113 we chose to shift it by the amount $(\tau_{best}^{data} - \tau_{best}^{MC})$

Focusing on the time windows with higher variability (namely the peaks of the light curve) allow to reduce the influence of this effect in present analysis.

The measurement of the dispersion τ_n (directly in the data) did not distinguish between dispersion arising from LIV effect itself (we call it $\tau_{\rm LIV}$) and spectral variability at the source, that could mimic a dispersion factor ($\tau_{\rm int}$). Hence we have

$$\tau_n = \tau_{\rm LIV} + \tau_{\rm int} \tag{8.3}$$

In previous chapters and sections, we have ignored the term $\tau_{\rm int}$, assuming $\tau_n = \tau_{\rm LIV}$. After having calculated a first confidence interval (CI) on the total degree of dispersion τ_n (section 8.2.4), we aimed at giving a CI for the dispersion $\tau_{\rm LIV}$ possibly arising because of LIV effects.

Some previous works addressed a possible GRB-intrinsic effect by modeling the jet emission of the GRBs (*e.g.* [82]). Here, we did not select a specific model of GRB emission at LAT energies ($E > 100$ MeV). Instead, a conservative estimation of the impact of $\tau_{\rm int}$ was chosen. We assumed that the measurements of τ_n are dominated by GRB intrinsic effects, so the PDF of $\tau_{\rm int}$ is to match the dispersion allowed by the data: $\langle \tau_{\rm int} \rangle = 0$, since all the measures on τ_n do not exclude a zero dispersion; and the width has to match the width of τ_n. Since the intrinsic effect is set to perfectly match any observed dispersion, the CIs on $\tau_{\rm LIV}$ were built so that they have the largest possible width.

The 1-Gaussian fits of the distributions of the best estimates $\hat{\tau}_n$ obtained as explained in 8.2.4.2 were taken as PDFs of $\tau_{\rm int}$. The fit is plotted on the distribution of the best estimates for GRB 090510 (linear case) in Figure 8.9. The Gaussian fit functions were centered on $0\,{\rm s\,TeV^{-1}}$ in order not to bias the choice of the sign of $\tau_{\rm int}$.

The model of emission in equation 8.1 was changed:

$$P(E,t|\tau_{\rm LIV};\tilde{\tau}_{\rm int}) = \frac{1}{N_{pred}} \Lambda(E) f(t - \tau_{\rm LIV} E^n - \tilde{\tau}_{\rm int} E^n) \tag{8.4}$$

For each simulated set, a random value of $\tilde{\tau}_{\rm int}$ was drawn. The calculation of $\tau_{\rm LIV}$ was then done with the ML methods; the means of the LL and UL distribution provide the CI for $\tau_{\rm LIV}$.

We ended up with CIs on $\tau_{\rm LIV}$, that correspond to a worst case (yet reasonable) scenario for GRB-intrinsic effects. These CIs on $\tau_{\rm LIV}$ are given in table 8.5 for ML-Gaus. They are less stringent (up to a factor 3 less constraining), though far more robust with respect to the presence of GRB-intrinsic effects.

8.2.6 Other systematics

The final results on $\rm E_{QG}$ will take into account two main systematic errors: the possible GRB-intrinsic effect and the parameterization of the templates:

— The evaluation of systematic uncertainty arising from the GRB-intrinsic effect was done in previous section.

— The systematic errors arising from the parameterization of the template light curve is included in the "calibrated" confidence intervals.

Studies of the other systematic uncertainties were performed with ML-Gaus method. The way they have been checked is described here. Table 8.6 summarizes these studies for GRB 090510. These secondary systematics were not considered when deriving the limits on $\rm E_{QG}$.

	Limits on τ_n		Limits on $\tau_{\rm LIV}$	
GRB	LL (n = 1)	UL (n = 1)	LL (n = 1)	UL (n = 1)
080916C	-0.76	0.69	-1.1	0.88
090510	-0.0032	0.0068	-0.0041	0.0087
090902B	-0.19	0.59	-0.36	0.79
090926A	-0.48	0.068	-0.59	0.19
GRB	LL (n = 2)	UL (n = 2)	LL (n = 2)	UL (n = 2)
080916C	-0.73	0.69	-0.85	0.78
090510	-0.00011	0.00013	-0.00036	0.00023
090902B	-0.061	0.061	-0.14	0.14
090926A	-0.32	0.13	-0.37	0.19

Table 8.5: Limits on $\tau_{\rm LIV}$ (right), taking into account possible GRB-intrinsic effects. Limits on τ_n, without considering these effects, are recalled on the left. These limits, obtained with ML-Gaus, are for a 90 % 2-sided confidence level. They are expressed in s/GeV^n.

8.2.6.1 Time intervals

The influence of the selection of the time intervals was evaluated by redoing the analysis on extended intervals: 0–20 s for GRB 080916C, -0.01–10 s for GRB 090510, 0–60 s for GRB 090902B, and 0–40 s for GRB 090926A. Though we can expect more precise results due to increased numbers of events, there also may be a larger degree of GRB-intrinsic spectral evolution that could mimic LIV dispersion. Confidence intervals are stable, except for GRB 090510, where the upper limit is multiplied by 2 for the linear case.

8.2.6.2 Impact of the photons with highest energies

We removed the most energetic photon in each dataset, *i.e.*:

— 2 photons above 1 GeV for GRB 080916C,

— 1 photon above 30 GeV for GRB 090510,

— several photons above 1 GeV for GRB 090902B,

— 2 photons above 1 GeV for GRB 090926A.

No significant change could be seen for GRB 080916C and GRB 090902B (multiplication by a factor 3 at maximum). For GRB 090926A, the upper limit is multiplied by 8 for the case n = 1. The loss of sensitivity is more crucial for 090510: up to a factor 17 for the upper limit in the quadratic case.

8.2.6.3 Instrument

The energy reconstruction uncertainty due to high off-axis angles is negligible. Difference between true and reconstructed energies leads to systematics of $\sim 10\%$ (n = 1) and $\sim 15\%$ (n = 2). The dependence of the effective area on the energy has been neglected: this systematic uncertainty is dominated by statistical uncertainty on the spectrum.

8.2.6.4 Other effects

Background contamination is negligible (very low rate, of the order of 10^{-1} Hz above 0.1 GeV and 10^{-3} Hz above 1 GeV). Uncertainty on the redshift is $\sim 1\%$ (GRB 080916C) and $\sim 0.1\%$ (other).

	Estimated error on input parameters	τ_1 (10^{-3} s GeV^{-1})	τ_2 (10^{-3} s GeV^{-2})
GRB intrinsic effects	–	$\lesssim 2$	$\lesssim 0.3$
Time intervals	–	$\lesssim 20$	$\lesssim 5$
E_{max}	–	$\lesssim 10$	$\lesssim 4$
Background contribution	1%	< 1	< 1
Acceptance factors	<5%	< 1	< 1
Energy resolution	15%	$\lesssim 5$	$\lesssim 0.5$

Table 8.6: Summary of systematic uncertainties for GRB 090510.

GRB	Redshift	κ_1	κ_2
080916C	4.35 ± 0.15	4.44	13.50
090510	0.903 ± 0.003	1.03	1.50
090902B	1.822 ± 0.001	2.07	3.96
090926A	2.1071 ± 0.0001	2.37	4.85

Table 8.7: Distances of analyzed GRBs. k_1 and k_2 are calculated from Eq. 8.6.

8.2.7 Results: E_{QG}

It is possible to use the limits on the total dispersion τ_n to set limits on the energy scale E_{QG} by using Eq. 8.5:

$$\tau_n = \frac{\Delta t}{\Delta(E^n)} \simeq s_{\pm} \frac{(1+n)}{E_{QG}^n 2H_0} \kappa_n \tag{8.5}$$

The normalized distance κ_n is calculated from the redshift of the source z, and the cosmological parameters $\Omega_m = 0.24 \pm 0.02$, $\Omega_\Lambda = 0.73 \pm 0.03$ (from WMAP [78], assuming a ΛCDM cosmological model):

$$\kappa_n = \int_0^z \frac{(1+z')^n \, dz'}{\sqrt{\Omega_m (1+z')^3 + \Omega_\Lambda}} \tag{8.6}$$

κ_1 and κ_2 are given for each GRB in table 8.7.

Table 8.8 presents lower limits on E_{QG} calculated using our constraints on τ_n. The best limit for subluminal case is obtained from GRB 090510 with ML-Gaus and corresponds to $E_{QG,1} > 3.3\ E_{Planck}$ and $E_{QG,2} > 8.6 \times 10^{10}$ GeV for a linear and a quadratic LIV effect, respectively.

8.2.8 Comparison with PG 1553+113 analysis

As mentioned before, the datasets from the four GRBs are free from any background events, and thus allowed:

— the use of a simpler PDF, without a second term for the background;

— the use of a kernel estimation of the template light curve.

Besides, the very short durations of the bursts – a few dozens of seconds at most compared to a few hours for PG 1553+113 flare – allow to get limits on the dispersion parameter of the same order ($\sim$ 10-500 s/TeV for the linear case), in spite of a maximum energy about 20 times smaller. And since the studied GRBs are detected at a higher redshift (z = 1 to 4 *vs.* z $\simeq$ 0.4 for PG 1553+113), the final limits on E_{QG} are much more constraining.

GRB Name	ML-Gaus		ML-KDE	
	n=1 (E_{Pl} units)			
	$s_{\pm}$=-1	$s_{\pm}$=+1	$s_{\pm}$=-1	$s_{\pm}$=+1
080916C	0.20	0.22	0.24	0.27
090510	11	5.2	2.8	3.3
090902B	0.37	0.12	0.21	0.21
090926A	0.17	1.2	0.14	0.23
	n=2 (10^{10} GeV units)			
080916C	0.34	0.35	0.52	0.56
090510	9.4	8.6	3.2	3.7
090902B	0.64	0.64	0.81	0.83
090926A	0.31	0.48	0.36	0.48

Table 8.8: Lower Limits on E_{QG} for linear (n=1) and quadratic (n=2) LIV for the subluminal ($s_{\pm}$=+1) and superluminal ($s_{\pm}$=-1) cases obtained from calibrated limits on τ_n as determined with ML-Gaus and ML-KDE. The CL values are 95% CL one-sided. These limits were produced using the total degree of dispersion in the data, τ_n.

8.3 Other methods of analysis and comparison of the results

Two other methods, complementary in terms of sensitivity and probing different aspects of the light curves, were used: PairView (PV) and Sharpness Maximization Method (SMM). We will explain their principle shortly, compare them with ML-Gaus [6] and give the limits on the dispersion parameter τ_n and on E_{QG} obtained with their application on the data from the same four GRBs.

8.3.1 PairView (PV)

The principle is to calculate the following ratios between all the pairs of photons (i, j) with $i \neq j$:

$$L_{i,j}(n) = \frac{t_i - t_j}{E_i^n - E_j^n} \tag{8.7}$$

with $t_{\{i,j\}}$ and $E_{\{i,j\}}$ the arrival time and the reconstructed energy of the photon $\{i, j\}$, n the order of LIV effect (linear for n = 1 and quad. for n = 2). The most probable value is kept as the best estimate of the parameter τ_n. This is done by using a Kernel Density estimation [83] of the distribution of $L_{i,j}$ values.

Energies below 100 MeV were discarded to minimize possible contamination by the Band component. There are N_{100} events left for the calculation of the $L_{i,jn}(n)$; values of N_{100} for each GRB are given in table 8.9.

Confidence intervals for PV were obtained the following way. Sets were created by randomizing the associations of time and energy from the original dataset. By definition, the time and energy distributions remain the same; yet the mixing of times and energies is expected to remove any possible dispersion in the data. A hundred thousand of these sets were produced; the PV method was applied to get the best estimate $\hat{\tau}_n$ of the dispersion parameter τ_n for each set. The resulting distribution, f_r, was used to approximate the PDF of the measurement error on τ_n (general case of any τ_n): $\epsilon = \hat{\tau}_n - \tau_n$. The CI for τ_n was then calculated from the quantiles of f_r.

6. ML-Gaus and ML-KDE giving similar results, we do not compare PV and SMM with ML-KDE here.

8.3.2 Sharpness Maximization Method (SMM)

Due to LIV-induced dispersion, the time distribution of the photons is spread or equivalently the sharpness of the light curve is reduced. The method consists in finding the value of the parameter τ_n that, when inversely applied on the data, will recover the sharpness of the light curve (assumed as initially maximal).

For each tested parameter τ_n: the arrival times are shifted by a factor $-\tau_n \mathrm{E}^n$; the resulting modified times t' are then sorted from smallest to largest; the sharpness of the resulting set of times t'_i is calculated. This method is similar to DisCan by Scargle *et al.* [70]: in their work, different definitions of the "sharpness" of the time distribution have been used. Here, a modification of Shannon function was used, given by the following sum over the photons i:

$$S(\tau_n) = \sum_{i=1}^{N-\rho} \log\left(\frac{\rho}{t'_{i+\rho} - t'_i}\right) \tag{8.8}$$

where ρ is a parameter defined *a priori* for each GRB from simulated datasets so as to maximize the sensitivity of the method. Small (resp. large) values of ρ will result in the method focusing on small (large) timescales. These values are given for each GRB in table 8.9. As for PV, energies below 100 MeV were discarded.

Confidence intervals were obtained in a similar fashion as PV.

	Time Range (s) All Methods		ρ SMM		N_{100} PV & SMM	
GRB	$n=1$	$n=2$	$n=1$	$n=2$	$n=1$	$n=2$
080916C	3.53–7.89	3.53–7.80	50	30	59	59
090510	-0.01–3.11	-0.01–4.82	50	70	157	168
090902B	5.79–14.22	5.79–14.21	80	80	111	111
090926A	8.92–10.77	9.3–10.76	25	30	60	58

Table 8.9: Configuration details for PV and SMM. ρ is the tuning parameter used in the SMM's sharpness measure; N_{100}, the number of events above 100 MeV used with PV and SMM.

8.3.3 Comparison with ML on simulated datasets

100,000 sets were simulated with no delay; the following methods were applied to each set: SMM, PV and ML-Gaus.

Figure 8.10 shows the lower and upper limits (left and right columns) and best estimate τ_1 (middle) for each method. The three methods give very similar distributions. However it seems that the distribution of the lower limits on τ_n got from the ML-Gaus method is less spread than the two other LL distributions. This tends to show that the ML-Gaus method is more precise.

Figure 8.11 shows the one-to-one comparison distribution of the lower and upper limits (left and right columns) and best estimate τ_1 (middle). The three methods all agree fairly well: most of the sets give the same best estimates, centered in 0 s/GeV. The PV and SMM methods are noticeably more in agreement with each other: they probably probe similar aspects of the datasets. Using PV/SMM and ML methods is beneficial as they probe different aspects of the GRB datasets, making them complementary.

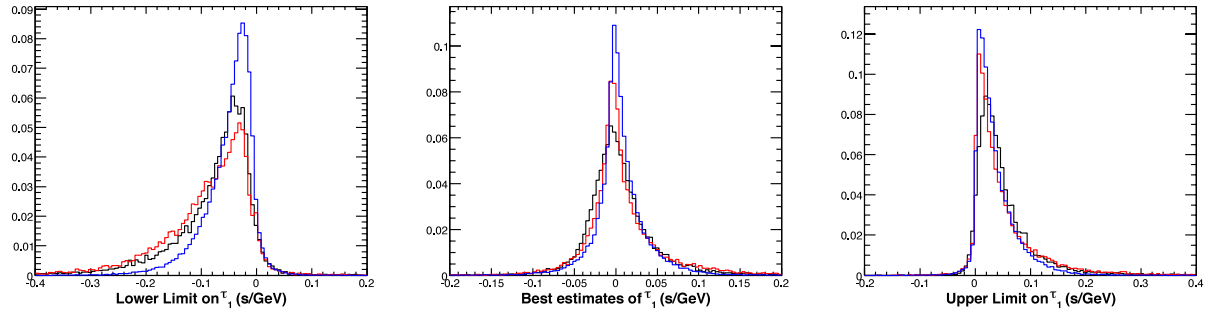

Figure 8.10: Distribution of the lower and upper limits (left and right columns) and best estimate τ_1 (middle). ML-Gaus (blue) has sharper distributions than PV (black) and SMM (red).

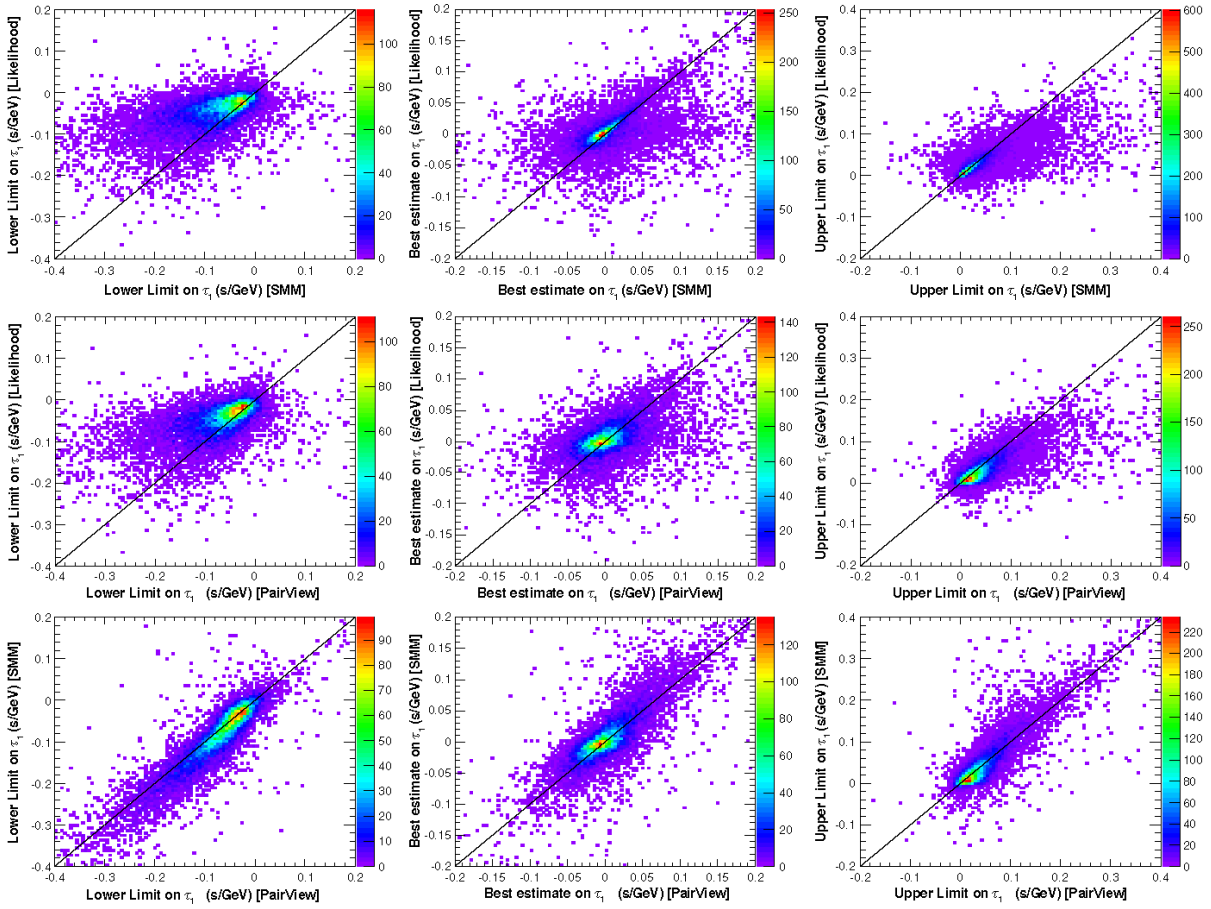

Figure 8.11: Comparison between the methods: lower and upper limits (left and right columns) and best estimate τ_1 (middle). ML vs SMM on top, ML vs PV in the middle, SMM vs PV at the bottom.

8.3.4 Results: dispersion parameter

Figures 8.12 demonstrate the application of the PV, SMM and ML-Gaus methods on GRB 090510 for the linear case (n=1).

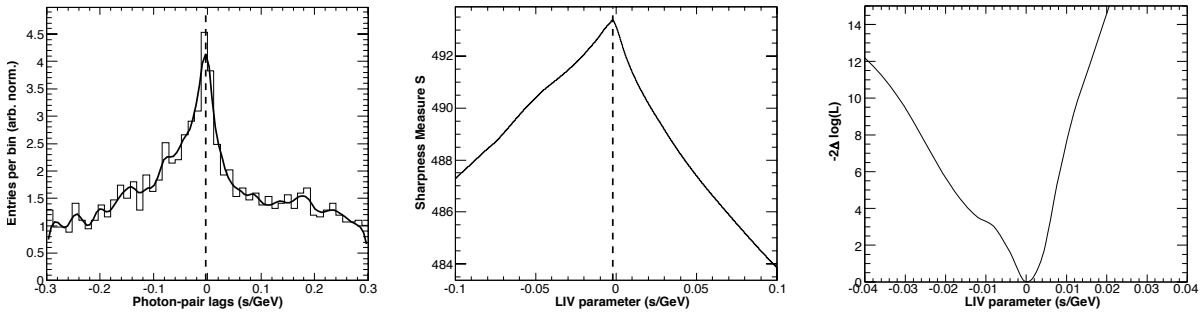

Figure 8.12: Application of the PV, SMM and ML-Gaus methods on GRB 090510 for the linear case (n = 1).

The measurements of τ_n parameter for PV and SMM are plotted in Figure 8.13 for both linear (left) and quadratic (right) cases. The results for ML-Gaus are shown for comparison. The limits obtained on the four bursts with the three different methods are compatible with zero dispersion. The likelihood method gives the more stringent constraints. PV and SMM method might be less sensitive to constrain the dispersion parameter τ_n when tail of the light curve last longer.

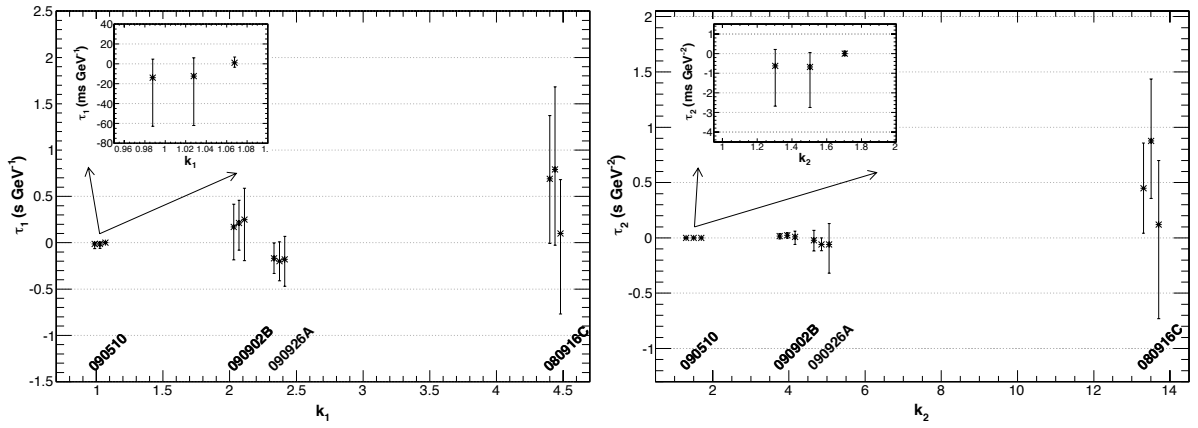

Figure 8.13: Measurements of the total degree of dispersion τ_n for each method, for a linear (n = 1, left) and a quadratic (n = 2, right) dispersion. Each triplet corresponds to the limits on τ_n obtained with PV (left point), SMM (middle) and ML-Gaus (right) on the data of *one* GRB. PV and ML points are shifted to visualize them better. The bars gives the CIs for a 90% double-sided confidence level.

8.3.5 Results: E_{QG}

Figure 8.14 shows E_{QG} lower limits derived from PV and SMM, along with ML-Gaus. As can be seen, results with the three different methods are compatible.

The best limit for subluminal case is obtained with GRB 090510 and corresponds to $E_{QG,1} > 7.6\, E_{Planck}$ (with PV) and $E_{QG,2} > 1.3 \times 10^{11}$ GeV (with SMM) for a linear and a quadratic LIV effect, respectively.

Horizontal lines show current most constraining limits (not accounting for intrinsic effects) obtained with GRB 090510 (*Fermi* LAT/GBM [81]) and PKS 2155-304 (H.E.S.S. [14]). These limits are improved by a factor 2 to 4.

New CIs on the LIV-induced dispersion parameter $\tau_{\rm LIV}$ were produced, as explained in section 8.2.5. We do not provide here their values for each GRB; limits on E_{QG} using these specific CIs were produced.Figure 8.14 also shows E_{QG} limits derived with data from the LIV-induced dispersion parameter $\tau_{\rm LIV}$, after accounting for intrinsic effects for each GRB (horizontal bars). One value, averaged over the three methods shown (PV, SMM, ML-Gaus), is given for each GRB [7]. These limits are less stringent, yet they are much more robust with respect to the presence of GRB-intrinsic dispersion than can masquerade as dispersion induced by LIV. The best limit for linear/subluminal case is obtained with GRB 090510: $E_{QG,1} \gtrsim 2\ E_{\rm Planck}$.

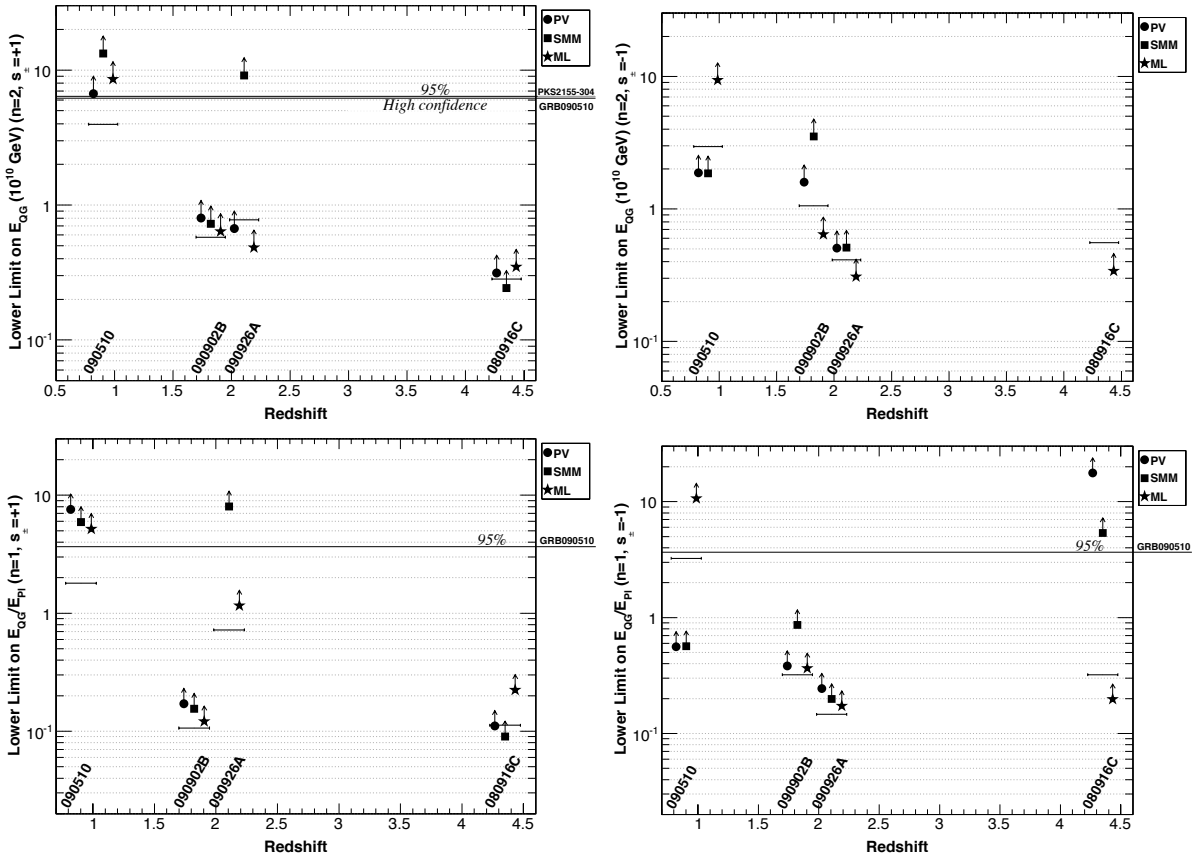

Figure 8.14: 95% one-sided CL limits on E_{QG} for superluminal (s = -1, left) and subluminal (s = +1, right) cases, for a linear (n = 1, top) and quadratic (n = 2, bottom) LIV effect. Each triplet of points corresponds to one GRB and shows, left to right, the limits obtained with PV, SMM and ML-Gaus (from τ_n). The horizontal bars correspond to a limit for the intrinsic-corrected case (from $\tau_{\rm LIV}$), averaged over the three methods.

7. The derivation of the LIV-induced dispersion parameter $\tau_{\rm LIV}$ was done differently for PV and SMM (see [71]). For GRB 090510, limits on $\tau_{\rm LIV}$ obtained with PV/SMM are up to an order of magnitude lower than limits on τ_n.

8.4 Conclusions

In this chapter, the maximum likelihood method with two different template determinations was used on the data of four bright and distant GRBs observed by the LAT. They both gave measures of the dispersion parameters which are compatible with zero dispersion. These sub-methods have similar precisions and allowed to put tight constraints on the linear and quadratic dispersion parameters τ_1 and τ_2. The tightest constraints on τ_n come from GRB 090510: its sharp peak and its shorter duration give limits of the order of the best obtained with AGNs at very high energy, of the order of 10 s/TeV.

From the limit on the dispersion parameter, it was possible to place robust constraints on the E_{QG} scale. The best limits were obtained for GRB 090510, in spite of the fact it is also the closest one: for the linear/subluminal case, $E_{QG,1} > 5.2\ E_{Planck}$ with ML-Gaus and $E_{QG,1} > 6.0\ E_{Planck}$ with ML-KDE using the total degree of dispersion τ_n (limits at 95% CL). Observing short GRBs at high redshift would possibly improve this limit. A discussion of the systematics, including taking into account possible source effects, was also conducted.

Two other methods, developed and applied by Vasileiou *et al.* [71], were also discussed and compared with the ML-Gaus method. The most stringent limit was obtained from GRB 090510 with the PV method: for the linear/subluminal case, $E_{QG,1} > 7.6\ E_{Planck}$ (at 95% CL) using the total degree of dispersion τ_n. This disfavors any class of Quantum Gravity model predicting $E_{QG} < E_{Planck}$.

With conservative hypotheses concerning the intrinsic dispersion τ_{int} possibly arising from astrophysical processes at the source, we placed limits on the LIV-induced degree of dispersion τ_{LIV}. The average of the three methods (PV/SMM/ML-Gaus) gives the following lower limit with GRB 090510 data: $E_{QG,1} \gtrsim 2\ E_{Planck}$ (at 95% CL). This confirms the above statement, *i.e.* strongly disfavors models requiring $E_{QG} < E_{Planck}$.

Summary & Conclusions

The dispersion relation of light in vacuum as we know it, $E^2 = c^2p^2$, might only be an approximation at energies reached on Earth and in collider experiments. Testing a modified dispersion relation is interesting for probing the application domain of Special relativity as well as discriminating between viable and non viable models of Quantum Gravity. A modified dispersion relation would result in diverse manifestations such as modifications in the spectrum of distant sources at TeV energies or different time of flight of photons from distant sources.

This latter manifestation has been investigated in this work, by looking at a flare of a blazar seen by H.E.S.S. and at four gamma-ray bursts detected by *Fermi*. Even though the exact emission mechanisms of these sources are still looked over – especially the origin of the GRB emission – they present excellent characteristics to conduct such analyses: they are indeed distant ($z > 0.4$ in this work), transient ($\Delta t \lesssim$ hour) events at high energies ($E > 20\,MeV$).

A modified likelihood method was proposed, adapted to flares with a large amount of background and modest statistics. It was applied on the H.E.S.S. data of this flare of PG 1553+113. No significant dispersion was measured, and limits on the E_{QG} scale at which QG effects causing LIV may arise were derived, in a region of redshift unexplored until now. Limits on the energy scale derived in this work, are $E_{QG,1} > 2.1 \times 10^{18}$ GeV and $E_{QG,2} > 6.4 \times 10^{10}$ GeV for the subluminal case. Compared with previous limits obtained with the PKS 2155–304 flare of 2006 July, the limits for PG 1553+113 for a linear dispersion are one order of magnitude less constraining while limits for a quadratic dispersion are of the same order of magnitude.

The likelihood method in case of no background was applied on four bright *Fermi* GRBs. Again, no significant energy dependence of the speed of light in vacuum was observed. The subsequent limits on the E_{QG} scale for the linear/subluminal case with the shortest – and closest – GRB, GRB 090510, are: $E_{QG,1} > 7.6\ E_{Planck}$ using the total degree of dispersion τ_n; and $E_{QG,1} \gtrsim 2\ E_{Planck}$ using the LIV-induced degree of dispersion τ_{LIV} (limits at 95% CL). The latter limits are more robust as they take into consideration the intrinsic effects possibly occurring at the source, described here in a model-independent way.

Besides blazars and GRBs, an additional type of source is being used to look for energy-dependent time delay in gamma photons: pulsars. Though most studied pulsars are located in our galaxy, and are thus quite close, they provide a stable source of data: the data taken does not depend on the fortuity of an event, like AGN flares and GRBs, but only on the duration of data-taking. VERITAS and MAGIC Collaborations have published limits on vacuum dispersion parameter with the Crab pulsar [84, 85]. Interesting limits using pulsed emission of pulsars are foreseen with the other IACTs, including H.E.S.S.

The *Cherenkov Telescope Array* [86], with two sites – one in each hemisphere [8] – is expected to bring a better sensitivity (up to 10 times increase) compared to current generation of IACTs in the range from 100 GeV to some 10 TeV, as well as extending this range below and above: with a larger effective area, the detection threshold energy of CTA will be lower and will benefit in particular to the detection of extragalactic sources [9]. The numerous telescopes in the array and their different sizes should allow various observation strategies, similar to that of satellite experiments: survey modes, pointing at specific sources (either planned or triggered), or even pointing at different sources at the same time – the full array(s) would then be split in several sub-arrays.

In particular, CTA will increase the number of AGN flare detections [87]. Also, it will hopefully observe GRBs at hundreds of GeV and up to TeV, if they emit at such energies. These bursts could be observed for instance in case a precursor burst is detected by satellite detectors with wide field of view, typically the *Fermi*-GBM. An effort toward the detection of GRBs is currently being made by IACT Collaborations. The study of the calibration charge presented in this work will allow, by assessing the quality of the data, to get proper spectral distributions at with CT5; this is a modest contribution toward getting lower energy spectrum of sources, including AGNs and, hopefully, GRBs.

Combining observations from large ground arrays, including CTA but also HAWK [88], a Cherenkov water tank array experiment, together with satellite experiments, *e.g. Fermi*, will bring an even more extended energy level-arm, leading to better source modeling and stronger measurements of dispersion in the data of these transient astrophysical objects.

8. sites yet to be selected

9. The expected performance actually depends on the number and configuration of the 3 types of telescopes in the array: large (24 m diameter), medium (12 m) and small (4 m - for the most energetic photons). At constant cost, several approaches are considered to get the lowest possible energy threshold: many large telescopes or only 4 large telescopes and a denser network of telescopes of smaller sizes.

Appendix A

Calibrated charge

Contents

A.1 Maker chain

Use of existing code, along with a new maker (`IntensityAccumulator`) built within the official HESS framework SASH, at the end of the following steps:

1. `Calibration::CalibCoefficientsMaker`
2. `ParisCalibration::CalibrationFinder`: get the different calibration coefficients:
   Pedestal from File
   Gain from DB
   Broken Pixels from File
3. `ParisReco::IntensityMaker`: apply the different coefficients to compute the calibrated charge in p.e.
4. `ParisCalibrationMakers::IntensityAccumulator`: store event intensities in individual histograms per pixels, and save them in `.root` file (one file per run)

A.2 Displays of pixels "dead" for more than 95% of the runs

Having sets covering different periods allow to compare and see the aging of the cameras. Two sets of runs were considered:

— **2013_153**: 153 runs taken in 2013, from April to November;

— **LATEST_29**: 29 runs taken in January 2014; the latest available runs at the time the study was performed.

Figures A.1 to A.5 show the displays of CT1 to CT5 with the following information for the two considered period: the pixels which are "Dead" [1] are in **gray**. They are in **black** if they have a hardware problem. The 4×4 gray or black squares correspond to a whole faulty drawer. A colorized 4-pixel columns indicates that an ARS is never locked (only for CT1–4).

1. meaning a missing calibration information or pixel deactivated *during the whole run*

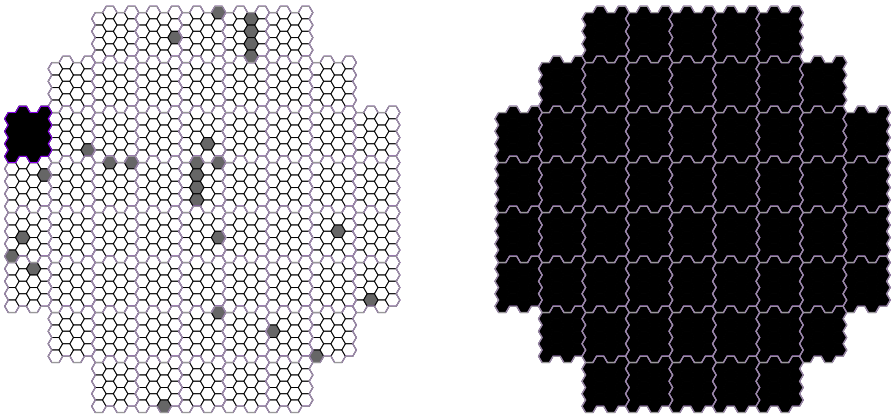

Figure A.1: Dead (gray) and absent (black) pixels of CT1; run set **2013_153** (left) and **LATEST_29** (right).

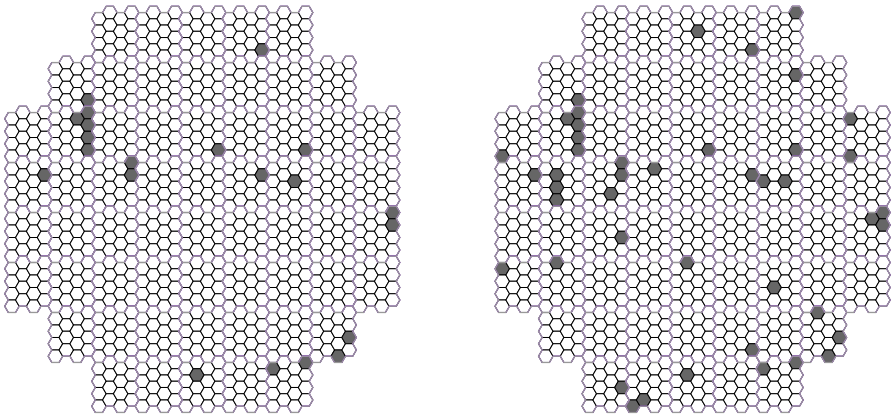

Figure A.2: Dead (gray) pixels of CT2; run set **2013_153** (left) and **LATEST_29** (right).

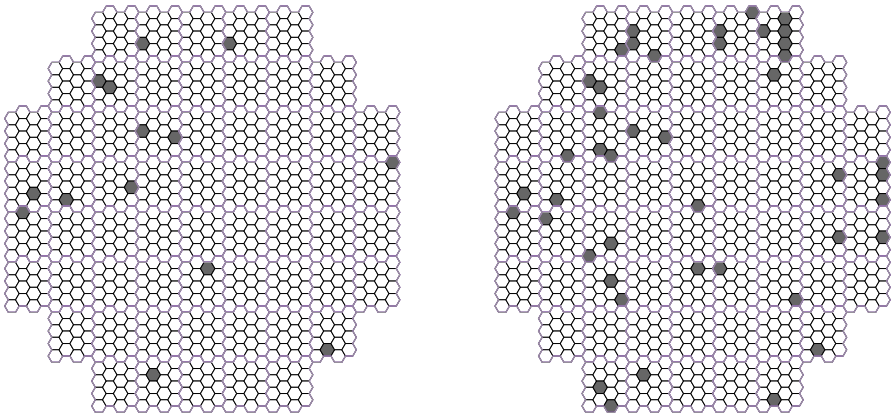

Figure A.3: Dead (gray) pixels of CT3; run set **2013_153** (left) and **LATEST_29** (right).

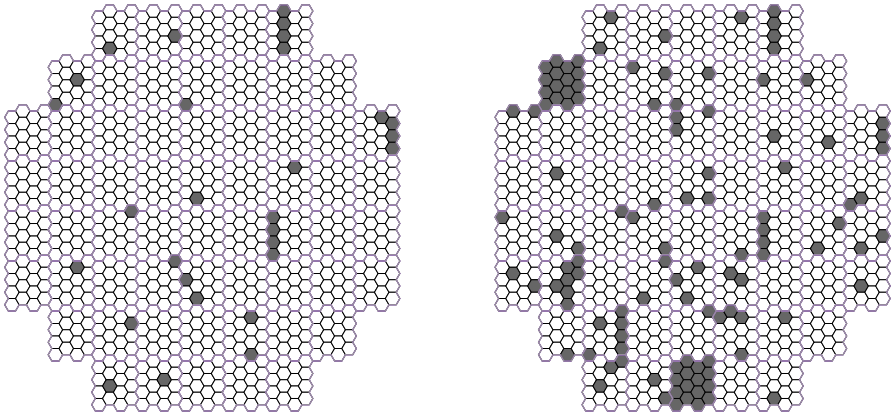

Figure A.4: Dead (gray) pixels of CT4; run set **2013_153** (left) and **LATEST_29** (right).

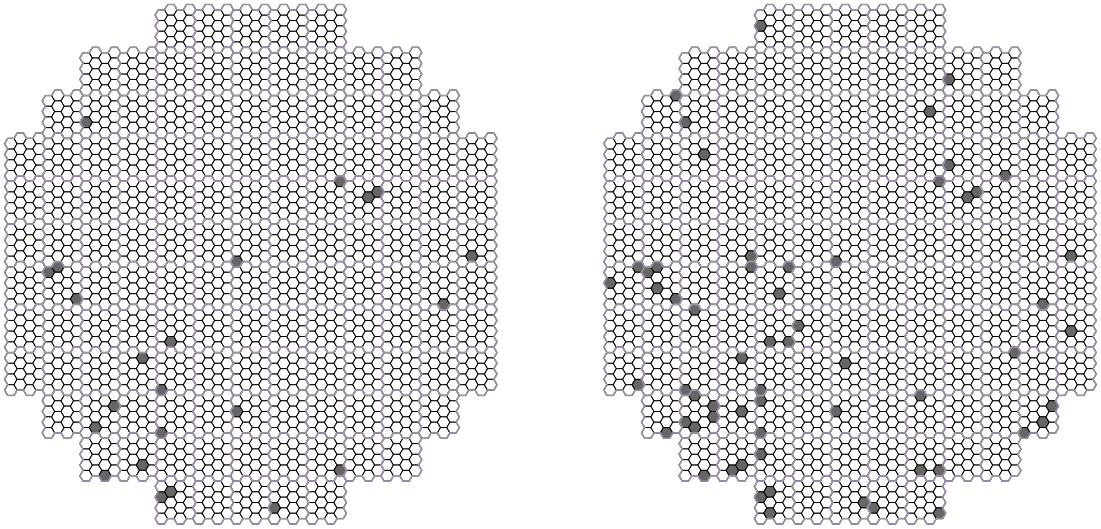

Figure A.5: Dead (gray) pixels of CT5; run set **2013_153** (left) and **LATEST_29** (right).

Appendix B

Maximum likelihood method: use of a Kernel Density Estimate, remarks.

Contents

B.1 Maximum likelihood method using a Kernel Density Estimate for the template lightcurve

These details on the Kernel density estimate are taken from Cranmer [83].

B.1.1 Principle of the Kernel density estimate - fixed case

Considering an initial set t_i, the kernel density estimation of the distribution is given by:

$$f_0(x) = \frac{1}{nh} \sum_{i=1}^{n} K\left(\frac{x - t_i}{h}\right)$$

with K an even, normalized, function, having a maximum at 0 (a "kernel") and h a smoothing parameter (the "bandwidth"). Thus the contribution of each point is spread, represented by the kernel $K\left(\frac{x-t_i}{h}\right)$. A common choice of K is a Gaussian with mean = 0 and width = 1:

$$K(x) = \frac{1}{\sqrt{2\pi}} \exp(-x^2/2)$$

This allows a good definition of the estimate, especially at the edges of the distribution: continuous and differentiable on $\mathbb{R}$.

B.1.2 Criteria for determining the bandwidth h

There is no single best method to determine an optimal bandwidth $h = h^*$ optimal. One should therefore calculate h^* with different criteria, and the compare obtained estimates.

The choice of the bandwidth h can be done using the following methods.

B.1.2.1 Silverman "Rule of thumb"

Here, the bandwidth h is calculated from a Gaussian approximation:

$$h^* = \left(\frac{4\hat{\sigma}^5}{3n}\right)^{\frac{1}{5}} \approx 1.06\hat{\sigma}n^{-1/5}$$

with $\hat{\sigma}$ the standard deviation of the distribution

B.1.2.2 Mean integrated squared error (MISE)

A choice of h is to minimize the mean integrated squared error:

$$MISE(\hat{f}_h) = E\left[\int_{-\infty}^{+\infty} \{\hat{f}_h(x) - f(x)\}^2 dx\right]$$

Problem is: the true density f is not known. One idea would be to approximate it with a finely binned histogram. But this is deferring the choice of the (band)width to the other tool (histogram), which itself has other disadvantages (discrete evolution).

For an asymptotically Gaussian distribution ($n \to \infty$), the MISE is minimal for

$$h^* = \left(\frac{4}{3}\right)^{1/5} \sigma n^{-1/5}$$

However, this h^* is not known in the general case, when the distribution is not asymptotically Gaussian.

B.1.2.3 Cross validation

The cross validation consists in the minimization of

$$CV(h) = \int \hat{f}_h^2(x)dx - \frac{2}{n(n-1)} \sum_{i=1}^{n} \sum_{j=1, i\neq j}^{n} K_h(t_i - t_j)$$

B.1.3 Modification: adaptive kernels

Using fixed kernel, the density estimate depends globally on the data, not locally. To tackle local variations of the data, variables bandwidths h are used:

$$h_i = \frac{h}{\sqrt{f(t_i)}}.$$

In this case, the part of the distribution with few events get a broader kernel, and the fluctuations are smoothed over.

Yet, the true density f is (still) not known. So it is estimated with f_0, previously determined (hence the term "adaptive").

B.1.4 Correction factor

In case local fluctuations σ_{local} are very small compared to the total width of the distribution σ, it is necessary to multiply each h_i^* with a factor:

$$\rho = \sqrt{\frac{\sigma_{local}}{\sigma}}.$$

B.1.5 Conclusion on KDE

Simple criteria exist to determine the kernel width (equivalent to the histogram binning); once this is done, the procedure to derive the template is straightforward (sum of kernels) and pain-free (no need to control the quality of a fit). However the use of such estimator may not be relevant when the flux at $\mathrm{t_{min}}$ and $\mathrm{t_{max}}$ is not negligible: in this case the template lightcurve is less accurately defined outside the range $[t_{\mathrm{min}}; t_{\mathrm{max}}]$.

B.2 Remarks on application on the Maximum likelihood method

— In the case of a single, non-Gaussian peak, the likelihood profile $-2\ln\Delta L$ is not parabolic, thus not equivalent to a χ^2 distribution. In such case, irregularities in the lightcurve are observed in the likelihood profiles.

— What influence the most the precision of the results are: the duration of the peak, the good definition of the peak, the energy of the photons (the highest the maximum energy $\mathrm{E_{max}}$, the most precise the measurement of τ_n) and the statistics (directly impact the likelihood profile/method).

— A template lightcurve has to be defined in all the tested range; especially, it has to be defined outside the range [$\mathrm{t_{min}}$, $\mathrm{t_{max}}$]. It creates boundaries issues if the flux at $\mathrm{t_{min}}$ and $\mathrm{t_{max}}$ is not negligible. There is a need of extending the template model, so that photons that are tested outside this range (e.g. initially $\mathrm{t_{min}} + \epsilon$, tested at $\mathrm{t_{min}} + \epsilon - \tau_n \times E^n$, where $\epsilon << 1$ and large E). It is particularly critical for the quadratic case (n = 2) as the term $\tau_2 \times E^2$ can be very large.

Appendix C

Limits on SME coefficients from the data of four GRBs observed by *Fermi*-LAT

As explained in chapter 1, in the context of the Standard Model Extension (SME) derived by Kostelecký *et al.* [10], dispersion due to LIV effect is described by a series expansion:

$$\tau_n \simeq \frac{1}{H_0}\left(\sum_{jm} {}_0Y_{jm}(\hat{\mathbf{n}})c^{(n+4)}_{(I)jm}\right) \times \kappa_n \tag{C.1}$$

Here, τ_n depends on the direction of the source $\hat{\mathbf{n}}$, on the spin-weighted spherical harmonics ${}_0Y_{jm}(\hat{\mathbf{n}})$ and on coefficients that describe the strength of LIV, $c^{(n+4)}_{(I)jm}$.

Any measurement (or limit) on τ_n can then lead to measurement (or limit) on:

— $\left(\sum_{jm} {}_0Y_{jm}(\hat{\mathbf{n}})c^{(n+4)}_{(I)jm}\right)$ in the case of direction-dependent effect;

— $c^{(n+4)}_{(I)00}$ in the case of direction-independent effect.

Table C.1 shows the 95% CL limits on the SME coefficients calculated from the CIs on τ_n obtained with ML-Gaus. The most stringent limits are from GRB 090510:

$$\sum_{jm} {}_0Y_{jm}(117^\circ, 334^\circ)c^{(6)}_{(I)jm} \in [-0.31; 0.16] \times 10^{-20}\text{GeV}^{-2}$$

for the direction dependent model, and

$$c^{(6)}_{(I)00} \in [-1.1; 0.57] \times 10^{-20}\text{GeV}^{-2}$$

for the vacuum isotropic model.

GRB	Vacuum			Vacuum isotropic		
	Quantity	LL	UL	Quantity	LL	UL
080916C	$\sum_{jm\,0} Y_{jm}(145°, 120°) c^{(6)}_{(I)jm}$	-8.7	20	$c^{(6)}_{(I)00}$	-31	70
090510	$\sum_{jm\,0} Y_{jm}(117°, 334°) c^{(6)}_{(I)jm}$	-0.31	0.16	$c^{(6)}_{(I)00}$	-1.1	0.57
090902B	$\sum_{jm\,0} Y_{jm}(63°, 265°) c^{(6)}_{(I)jm}$	-3.4	5.2	$c^{(6)}_{(I)00}$	-12	18
090926A	$\sum_{jm\,0} Y_{jm}(156°, 353°) c^{(6)}_{(I)jm}$	-11	5.2	$c^{(6)}_{(I)00}$	-37	19

Table C.1: 95% lower (LL) and upper (UL) limits on the SME coefficients, averaged over the three methods and calculated using the CIs on $\tau_{\rm LIV}$; values are given in 10^{-20} GeV^{-2}.

Bibliography

[1] G. Amelino-Camelia, Living Reviews in Relativity **16** (2013).

[2] S. Liberati, Classical and Quantum Gravity **30**, 133001 (2013).

[3] D. Mattingly, Living Rev.Rel. **8**, 5 (2005).

[4] A. Barrau and J. Grain, *Relativité générale cours et exercices corrigés* (Dunod, Paris, 2011).

[5] A. Reimer, Nuclear Physics B - Proceedings Supplements **203-204**, 33 (2010).

[6] T. G. Pavlopoulos, Physics Letters B **625**, 13 (2005).

[7] G. Amelino-Camelia, Int.J.Mod.Phys. **D11**, 35 (2002).

[8] V. A. Kostelecký and R. Potting, Physical Review D **51**, 3923 (1995).

[9] D. Colladay and A. Kostelecky, Phys.Rev.D **55**, 6760 (1997).

[10] V. A. Kostelecký and M. Mewes, Physical Review D **80** (2009).

[11] O. W. Greenberg, Phys.Rev.Lett. **89**, 231602 (2002).

[12] G. Amelino-Camelia, J. R. Ellis, N. E. Mavromatos, D. V. Nanopoulos, and S. Sarkar, Nature **393**, 763 (1998).

[13] U. Jacob and T. Piran, Phys.Rev. **D78**, 124010 (2008).

[14] A. Abramowski *et al.*, Astroparticle Physics **34**, 738 (2011).

[15] M. Schmidt, Nature **197**, 1040 (1963).

[16] W. Benbow *et al.*, Note (2007), arXiv: 0709.4608.

[17] R. Antonucci, Ann.Rev.Astron.Astrophys. **31**, 473 (1993).

[18] C. M. Urry and P. Padovani, Publ.Astron.Soc.Pac. **107**, 803 (1995).

[19] M. H. Cohen *et al.*, The Astrophysical Journal **170**, 207 (1971).

[20] A. R. Whitney *et al.*, Science **173**, 225 (1971).

[21] B. G. Piner, D. Bhattarai, P. G. Edwards, and D. L. Jones, The Astrophysical Journal **640**, 196 (2006).

[22] M. J. Rees, Nature **211**, 468 (1966).

[23] T. S. Stanev, *High Energy Cosmic Rays*, Édition : 2nd ed. 2010 ed. (Springer, Berlin ; New York : Chichester, UK, 2010).

[24] ANTARES Collaboration, Note (1999), arXiv: astro-ph/9907432.

[25] J. Ahrens *et al.*, Astroparticle Physics **20**, 507 (2004).

[26] G. Pelletier, Plasma turbulence and the astrophysical objects, in *Proc. of Congrès de la Société Française de Physique*, p. 353, 1985.

[27] M. Punch *et al.*, Nature **358**, 477 (1992).

[28] M. R. Metzger *et al.*, Nature **387**, 878 (1997).

[29] D. E. Reichart, The Astrophysical Journal **495**, L99 (1998).

[30] N. R. Tanvir *et al.*, Nature **461**, 1254 (2009), arXiv: 0906.1577.

[31] J. P. Norris *et al.*, The Astrophysical Journal **459**, 393 (1996).

[32] B.-B. Zhang *et al.*, The Astrophysical Journal **730**, 141 (2011), arXiv: 1009.3338.

[33] C. A. Meegan *et al.*, Nature **355**, 143 (1992).

[34] D. Band *et al.*, The Astrophysical Journal **413**, 281 (1993).

[35] A. Haungs, H. Rebel, and M. Roth, Reports on Progress in Physics **66**, 1145 (2003).

[36] M. de Naurois, *L'expérience CELESTE: Reconversion d'une centrale solaire pour l'astronomie gamma. Première observation de la Nébuleuse du Crabe et du Blazar Markarian 421 entre 30 et 300 GeV.*, PhD thesis, Université Pierre et Marie Curie - Paris VI, 2000.

[37] T. C. Weekes *et al.*, The Astrophysical Journal **342**, 379 (1989).

[38] A. Barrau *et al.*, Nuclear Instruments and Methods in Physics Research Section A: Accelerators, Spectrometers, Detectors and Associated Equipment **416**, 278 (1998).

[39] A. Daum *et al.*, Astroparticle Physics **8**, 1 (1997).

[40] C. Baixeras *et al.*, Nuclear Instruments and Methods in Physics Research Section A: Accelerators, Spectrometers, Detectors and Associated Equipment **518**, 188 (2004).

[41] T. C. Weekes *et al.*, Astroparticle Physics **17**, 221 (2002).

[42] K. Bernlöhr *et al.*, Astroparticle Physics **20**, 111 (2003).

[43] J. A. Hinton and W. Hofmann, Annual Review of Astronomy and Astrophysics **47**, 523 (2009).

[44] F. Aharonian *et al.*, Astroparticle Physics **22**, 109 (2004).

[45] F. Brun, *Recherche de sources ténues ou transitoires dans les régions centrales de la Galaxie avec H.E.S.S. Application à l'étude de la région du vestige de supernova W49B.*, PhD thesis, Université Pierre et Marie Curie - Paris VI, 2011.

[46] J. Bolmont *et al.*, Nuclear Instruments and Methods in Physics Research Section A: Accelerators, Spectrometers, Detectors and Associated Equipment **761**, 46 (2014).

[47] J. P. Tavernet, Results from the H.E.S.S. drawer test bench (internal note), 2002.

[48] R. Chalme-Calvet, M. de Naurois, J.-P. Tavernet, and H.E.S.S. Collaboration, (2014), arXiv: 1403.4550.

[49] F. Aharonian *et al.*, Astronomy and Astrophysics **457**, 899 (2006), arXiv:astro-ph/0607333.

[50] M. P. Kertzman and G. H. Sembroski, Nuclear Instruments and Methods in Physics Research A **343**, 629 (1994).

[51] J. Guy, *Premiers résultats de l'expérience H.E.S.S. et étude du potentiel de détection de matière noire supersymétrique*, PhD thesis, Université Pierre et Marie Curie - Paris VI, 2003.

[52] A. M. Hillas, International Cosmic Ray Conference **3**, 445 (1985).

[53] S. Le Bohec *et al.*, Nuclear Instruments and Methods in Physics Research A **416**, 425 (1998).

[54] M. de Naurois and L. Rolland, Astroparticle Physics **32**, 231 (2009).

[55] M. de Naurois, *L'astronomie gamma de très haute énergie de H.E.S.S. à CTA. Ouverture d'une nouvelle fenêtre astronomique sur l'Univers non thermique*, HDR thesis, Université Pierre et Marie Curie - Paris VI, 2012.

[56] T.-P. Li and Y.-Q. Ma, The Astrophysical Journal **272**, 317 (1983).

[57] L. Rolland, *Etalonnage des cameras de l'experience d'astronomie gamma H.E.S.S. et observations du Centre Galactique au-dela de 100 GeV*, PhD thesis, Université Pierre et Marie Curie - Paris VI, 2005.

[58] F. Piron *et al.*, Astronomy and Astrophysics **374**, 895 (2001).

[59] H.E.S.S. collaboration webpage.

[60] W. Kraushaar *et al.*, The Astrophysical Journal **141**, 845 (1965).

[61] S. M. Derdeyn, C. H. Ehrmann, C. E. Fichtel, D. A. Kniffen, and R. W. Ross, Nucl.Instrum.Meth. **98**, 557 (1972).

[62] K. Bennett *et al.*, (1974).

[63] G. Kanbach *et al.*, Space Science Reviews **49**, 69 (1988).

[64] M. Tavani *et al.*, Astronomy and Astrophysics **502**, 995 (2009).

[65] W. B. Atwood *et al.*, The Astrophysical Journal **697**, 1071 (2009).

[66] Fermi observation strategy: Pointed vs survey, http://fermi.gsfc.nasa.gov/ssc/library/support/Pointed-vs-Survey.pdf.

[67] W. B. Atwood *et al.*, Note (2013), arXiv: 1303.3514.

[68] *Fermi*-LAT Collaboration, The Astrophysical Journal Supplement Series **203**, 4 (2012), arXiv: 1206.1896.

[69] J. Albert *et al.*, Physics Letters B **668**, 253 (2008), Phys.Lett.B668:253-257,2008.

[70] J. D. Scargle, J. P. Norris, and J. T. Bonnell, The Astrophysical Journal **673**, 972 (2008).

[71] V. Vasileiou *et al.*, Physical Review D **87**, 122001 (2013).

[72] M. Martinez and M. Errando, Astroparticle Physics **31**, 226 (2009).

[73] H.E.S.S. Collaboration, The Astrophysical Journal, to appear , arXiv: 1501.05087.

[74] M. Natrella, *NIST/SEMATECH e-Handbook of Statistical Methods* (NIST/SEMATECH, 2010).

[75] F. Aharonian *et al.*, Astronomy and Astrophysics **448**, L19 (2006).

[76] C. W. Danforth, B. A. Keeney, J. T. Stocke, J. M. Shull, and Y. Yao, ArXiv e-prints (2010), 1005.2191.

[77] MAGIC Collaboration and J. Cortina, ATel #4069: MAGIC detects an unprecedented high VHE gamma-ray emission from the blazar PG 1553+113, 2012.

[78] E. Komatsu *et al.*, The Astrophysical Journal Supplement Series **192**, 18 (2011).

[79] S. D. Biller *et al.*, Physical Review Letters **83**, 2108 (1999).

[80] *Fermi*-LAT Collaboration, (unpublished).

[81] A. A. Abdo *et al.*, Nature **462**, 331 (2009).

[82] Z. Chang, Y. Jiang, and H.-N. Lin, Astroparticle Physics **36**, 47 (2012).

[83] K. Cranmer, Computer Physics Communications **136**, 198 (2001).

[84] MAGIC Collaboration and E. Aliu, Science **322**, 1221 (2008), arXiv: 0809.2998.

[85] VERITAS Collaboration *et al.*, Science **334**, 69 (2011), arXiv: 1108.3797.

[86] CTA Consortium, Experimental Astronomy **32**, 193 (2011), arXiv: 1008.3703.

[87] H. Sol *et al.*, Astroparticle Physics **43**, 215 (2013), 1304.3024.

[88] HAWC collaboration *et al.*, Astroparticle Physics **35**, 641 (2012), arXiv: 1108.6034.

Résumé : Des modèles de Gravité Quantique (QG) prédisent une violation de l'invariance de Lorentz (LIV), se manifestant par une dispersion de la lumière dans le vide. Si un tel effet existe, des photons d'énergies différentes émis en même temps par une source distante sont détectés sur Terre à des moments différents. Les émissions transitoires à (très) hautes énergies provenant de sources astrophysiques lointaines, comme les sursauts gamma (GRBs) et les blazars sont utilisées pour contraindre cet effet LIV. Cet ouvrage présente les études menées avec deux télescopes gamma majeurs : H.E.S.S.– pour lequel une étude de la qualité des données étalonnées a été réalisée – et *Fermi*-LAT. Les énergies et les temps d'arrivée de photons individuels ont été utilisés pour contraindre le paramètre de dispersion dans le vide ainsi que l'échelle d'énergie E_{QG} à laquelle des effets LIV peuvent apparaitre. La méthode de maximum de vraisemblance est décrite, avec une étude détaillée des systématiques. Une modification dans le cas de fond non négligeable est appliquée aux données de l'éruption d'un blazar observé par H.E.S.S. : les limites obtenues sur E_{QG} sont moins contraignantes que les meilleures limites précédentes, mais elles se trouvent à un redshift non couvert à ce jour. Quatre GRBs observés par *Fermi*-LAT ont aussi été analysés, en déterminant la courbe de lumière de deux manières : ajustements gaussiens et estimation par densité de noyaux. Les meilleures limites sur E_{QG} pour le cas linéaire/subluminal sont obtenus avec GRB 090510 : $E_{QG,1} > 7{,}6\ E_{Planck}$. Des limites plus robustes, tenant compte des effets intrinsèques à la source, ont également été produites.

Mots-clés : astronomie γ : H.E.S.S., astronomie γ : *Fermi*-LAT, Invariance de Lorentz, sources transitoires : sursauts gamma, noyaux galactiques actifs : blazars, maximum de vraisemblance

Abstract: Some Quantum Gravity (QG) theories allow for a violation of Lorentz invariance (LIV), manifesting as a dependence on the velocity of light in vacuum on its energy. If such a dependence exists, then photons of different energies emitted together by a distant source will arrive at the Earth at different times. (Very) high energy transient emissions from distant astrophysical sources such as Gamma-ray Bursts (GRBs) and blazars can be used to search for and constrain LIV. This work presents the studies obtained with two leading Gamma-ray telescopes: H.E.S.S.– for which a study of the quality of the calibrated data was performed – and *Fermi*-LAT. The energies and arrival times of individual photons were used to constrain the vacuum dispersion parameter and the energy scale E_{QG} at which QG effects causing LIV may arise. The maximum likelihood method is described, with detailed studies of the systematics. A modification for a non-negligible background is provided and applied to the data of an AGN flare observed by H.E.S.S.: the obtained limits on the QG energy scale are less constraining than the previous best limits obtained with blazars; yet, the new limits lie a redshift range not covered this far. Four bright and quasi background-free GRBs observed by the *Fermi*-LAT were also analysed, with two different template light curve determinations – Gaussian fits and Kernel Density Estimates. The best limits on the E_{QG} scale for the linear/subluminal case are from the shortest burst, GRB 090510: $E_{QG,1} > 7.6\ E_{Planck}$. More robust limits, considering the intrinsic effects possibly occurring at the source, were also derived.

Key words: γ-ray astronomy: H.E.S.S., γ-ray astronomy: *Fermi*-LAT, Lorentz Invariance, Transient sources: Gamma-ray burst, Active galactic nuclei: blazars, maximum likelihood method